

# Exploring molecular encoding in the context of T cell-based immunotherapy

**Moss, Keith Henry**

*Publication date:*
2021

*Document Version*
Publisher's PDF, also known as Version of record

# Exploring molecular encoding in the context of T cell-based immunotherapy

Keith H. Moss

PhD Thesis

Kongens Lyngby

May 2021

# PREFACE

This PhD thesis has been submitted to the Technical University of Denmark, Department of Health Technology, to fulfill one of the requirements for obtaining a PhD degree. All of the research presented in this thesis was conducted under the principle supervision of Professor Sine Reker Hadrup, initially at the National Veterinary Institute, then at the Department of Micro- and Nanotechnology and finally at the Department of Health Technology. The research was conducted from September 2017 to May 2021. Approximately halfway through the PhD, a change of projects resulted in the scope of the PhD changing considerably.

The thesis consists of an introductory section, where relevant literature and scientific background is covered. Followed by one Manuscript, which represents the primary focus of the thesis. The main research findings for this are reflected upon in the discussion section. Two additional results sections are then introduced and the research findings are presented with reflection in each of the sections. An epilogue is given after the additional results, where the overall perspectives for the three research topics are provided. Finally, a review article, published as first author, has been included in the end. This article is not entirely relevant for the scope of the thesis, but provides further background for one of the additional results sections.

# ACKNOWLEDGEMENTS

Firstly, I would like to thank Sine for the four years of guidance, leadership and inspiration, since I began my Master's thesis project with her and continued in her group to pursue my PhD. Sine's general kindness as well as her ability to approach all tasks, big and small, calmly, really promoted a comfortable and stress-free research environment.

I would like to thank my co-supervisors involved throughout the PhD, Søren in the beginning, and Amalie towards the end. Søren's laidback, but motivating nature, as well as our good personal relationship, really made it a pleasant work environment. After my change in projects, Amalie was able to efficiently train me in the new techniques and was incredibly good at providing feedback and discussion for any sort of question that I had.

I would like to thank the Technicians, Bente, Anni and Julian, for their essential work in keeping the labs running behind the scenes, but also for providing support whenever it was needed. On a similar note, I would like to acknowledge Tripti, for taking care of all the MHC production, without such, our research would not have been as feasible. I would like to give a word of thanks to Mo and Jeppe, for assisting with my big final experiment. To my office mates, Sunil, Annie, Kamilla, Mo, Amalie, as well as the rest of the lovely people in building 202, for all the interesting discussions, both work- and non-work related.

I would like to give a big thanks to my family, despite being separated by vast oceans, they have always provided moral support and motivation throughout my PhD studies. I would like to give a shout-out to my friends, both near and far, for keeping me motivated to achieve my title as Dr. Moss. Last but certainly not least, I would like to thank Isabel for being by my side during these last few months of stress and isolation.

# ABSTRACT

The immune system plays a pivotal role in maintaining general health and providing protection against the abundance of invading pathogens that an individual may come across in their lifetime. Regulation and clearance of cells undergoing malignant transformation is another critical function of the immune system. However, the heterogeneous nature of cancer has proven to be a major obstacle for obtaining effective therapeutic outcome in the majority of patients. The concept of immunotherapy, where the aim is to boost the patient's natural immunity towards cancer, has revolutionized the way cancer treatment is approached. Nonetheless, despite massive advancements in the field, the multifactorial nature of the interactions between the immune system and cancer has resulted in mixed therapeutic outcomes. The factors which contribute to clinical response are not universal, which partly explains why the majority of patients still do not respond favorably to strategies such as immune checkpoint blockade therapy. As such, there has been a great effort in recent years to identify the key parameters, or immune predictors, which dictate the patient's outcome to immune-based therapies. A comprehensive understanding of these immune predictors would enable a more effective design of treatment strategies, based on the profile of the given cancer type or individual patient.

The overall objective of this thesis is to evaluate tumor antigen recognition and novel tools for the detection of antigen-specificity, as well as to highlight nanoparticle-based strategies for delivery of therapeutic cargo, in the context of T cells and cancer therapy. These concepts are connected by one common element, the use of DNA barcodes as a form of molecular encoding.

In manuscript I, DNA barcode-labeled MHC multimers are utilized in combination with a multicolor T cell phenotype panel in a novel approach that allows the parallel analysis of T cell recognition with corresponding phenotypic characteristics. This was performed to assess the characteristics of neoantigen-reactive $CD8^+$ T cells (NARTs), one of the primary drivers of immunotherapy-based tumor elimination, in the hopes of understanding whether T cell-intrinsic factors are involved in the response to therapy. This study was performed in a diverse cohort of cancer patients from a Phase I basket trial, in an effort to identify a profile of NARTs that could distinguish responding from non-responding patients. Although, due to the small sample size and heterogeneity of the cohort, no significant difference was observed between the patient groups, related to the breadth and magnitude of the detected NARTs. There also appeared to be no significant phenotypic profile associated with the responding patient NARTs. However, insights into a favorable antigen-reactive T cell profile were made evident. Tendencies for increased expression of markers such as Ki67, CD27 and TCF-1 were observed in some of the patients, post-therapy. Indicating that the presence of proliferating, early-activated NARTs with self-renewal properties could provide therapeutic benefit. Further studies in larger cohorts would be warranted to provide concise conclusions.

In the first additional results section, a novel strategy was applied to make use of DNA barcodes for encoding MHC tetramer reagents for the detection of viral-reactive $CD8^+$ T cells. The second additional results section implemented a DNA barcode in the nanoparticle design, as a proof of concept for developing a screening platform to identify formulations successful in the

in vivo delivery of messenger RNA cargo. These preliminary results indicate that the use of DNA barcodes could be widely applicable for encoding purposes, not only to identify relevant drug and T cell targets but also to facilitate the design of more effective nanoparticle delivery systems for enhancing current therapeutic strategies.

# DANSKE RESUMÉ

Immunsystemet spiller en central rolle for at opretholde den generelle sundhed, og yder beskyttelse mod den overflod af patogener, som hvert individ kan blive eksponeret for i deres levetid. En anden kritisk funktion af immunsystemet består i at regulere og eliminere de celler, der gennemgår malign transformation. Det har imidlertid vist sig at den heterogene karakter af cancer celler, er en væsentlig hindring for at opnå terapeutisk effekt for en stor del af patienter. Begrebet immunterapi, hvor målet er at øge patientens naturlige immunitet mod cancer, har revolutioneret vores tilgang til behandlingen af kræft. På trods af massive fremskridt inden for feltet, har den multifaktorielle karakter af interaktionerne mellem immunsystemet og kræft, resulteret i varierende terapeutiske resultater. De faktorer, der bidrager til klinisk respons, er ikke universelle, hvilket delvis forklarer, hvorfor en stor del af patienterne stadig ikke responderer på behandlinger såsom immuncheckpoint blokadeterapi. For at kortlægge disse faktorer, har der de seneste år været en stor indsats for at identificere de prædikative immunmarkører, som dikterer hvilke patienter der kan have gavn af en given immunterapeutisk behandling. En bred forståelse af disse immunmarkører vil således gøre det muligt at udforme mere effektive behandlingsstrategier baseret på profilen af den givne kræfttype eller den individuelle patient.

Det overordnede formål med denne afhandling er både at evaluere tumorantigengenkendelse, og nye værktøjer til detektion af antigenspecificitet, samt at beskrive hvordan nanopartikelbaserede strategier kan benytte til levering af terapeutisk aktive elementer, i forbindelse med T-celler og kræftbehandling. Disse emner er forbundet af et fælles element; molekylær kodning via DNA-stregkoder.

I manuskript I anvendes DNA-stregkodemærkede MHC-multimerer i kombination med et multifarvet T-cellefænotype-panel, som en ny tilgang, der muliggør parallel analyse af T-celle-genkendelse og fænotypisk karakteristika. Dette blev udført med det formål at vurdere egenskaberne ved neoantigen-reaktive $CD8^+$ T-celler (NARTs), en af de primære drivkræfter for immunterapi-baseret tumoreliminering, i håb om at forstå, hvilke iboende faktorer ved T-cellerne, der er afgørende for effekten af behandlingen. Denne undersøgelse blev udført baseret på et fase I forsøg, der inkluderede en gruppe patienter med forskelligartet kræft, med det formål at identificere en profil af NART'er, der gør det muligt at identificere de patienter der responderer på behandling. På grund af det begrænsede antal patienter inkluderet i studiet, og på grund af de forskelligartede typer kræft, blev der ikke observeret nogen signifikant forskel mellem patientgrupperne. Hverken relateret til antallet af forskellige responser eller frekvensen af de påviste NART populationer. Der blev heller ikke fundet nogen signifikant fænotypisk profil i forbindelse med de NARTér der blev identificeret i patienter der havde gavn af behandlingen. Resultaterne gav dog en indikation af hvad der kan være en gunstig profil af de antigenreaktiv T-celler. Således blev der observeret en tendens til øget ekspression af markører såsom Ki67, CD27 og TCF-1 hos nogle af patienterne efter behandling. Dette indikerer, at tilstedeværelsen af proliferende og tidligt aktiverede NART'er kunne give en terapeutisk fordel. Yderligere undersøgelser i større kohorter ville være nødvendinge for a drage yderligere konklusioner.

I det første supplerende resultatafsnit blev der anvendt en ny strategi som gør brug af DNA-stregkoder til kodning af MHC-tetramerer til at påvise virus-reaktive $CD8^+$ T-celler. Det andet supplerende afsnit beskriver hvordan DNA-stregkoder kan benyttes i design af nanopartikler, som *proof-of-concept* for udviklingen af en screeningsplatform der kan benyttes til at identificere de mest optimale materialesammensætninger til specifikt at levere messenger RNA in vivo. De foreløbige resultater giver en indikation af, at DNA-stregkoder kan benyttes til sporing i større udstrækning, ikke kun for at identificere relevante mål for lægemidler og T-celler, men også for at gøre det muligt at designe systemer til udvikling af effektiv terapeutisk levering via nanopartikler, som kan forbedre nuværende behandlingsstrategier.

# ABBREVIATIONS

| | |
|---|---|
| ACT | Adoptive cell therapy |
| APC | Antigen-presenting cell |
| β2M | $\beta_2$ microglobulin |
| CDR | Complementarity-determining region |
| CITE-Seq | Cellular indexing of transcriptomes and epitopes by sequencing |
| CMV | Cytomegalovirus |
| CTL | Cytotoxic T cells |
| CTLA-4 | Cytotoxic T lymphocyte antigen 4 |
| CyTOF | Cytometry by time-of-flight |
| DC | Dendritic cell |
| DMSO | Dimethyl sulfoxide |
| EBV | Epstein-Barr virus |
| ER | Endoplasmic reticulum |
| FasL | Fas ligand |
| FDA | Food and drug administration |
| FDR | False-discovery rates |
| FLU | Influenza virus |
| FCS | Fetal calf serum |
| GFP | Green fluorescent protein |
| GZMb | Granzyme B |
| HLA | Human leukocyte antigens |
| HNSCC | Head and neck squamous cells cancer |
| ICB | Immune checkpoint blockade |
| IDO1 | Indoleamine 2,3-dioxygenase |
| IFN | Interferon |
| Ig | Immunoglobulin |
| IL | Interleukin |
| IMGT | ImMunoGeneTics |
| LNP | Lipid nanoparticle |
| MCP | Microenvironment cell population |
| MDSC | Myeloid-derived suppressor cells |
| MFI | Median fluorescent intensity |
| MHC | Major-histocompatibility complex |
| mRNA | Messenger RNA |
| MSI | Microsatellite instability |
| MuPEXi | Mutant peptide extractor and informer |
| NART | Neoantigen-reactive T cells |
| NK | Natural killer |
| NP | Nanoparticle |
| NSCLC | Non-small cell lung cancer |
| Oligo | Oligonucleotide |

| | |
|---|---|
| PD1 | Programmed cell death protein 1 |
| PD-L1 | Programmed death-ligand 1 |
| PMBC | Peripheral blood mononuclear cell |
| PRR | Pattern-recognition receptor |
| qPCR | Quantitative PCR |
| RCC | Renal cell carcinoma |
| REAP-seq | RNA expression and protein sequencing |
| RECIST | Response evaluation criteria in solid tumors |
| REP | Rapid expansion protocol |
| SA | Streptavidin |
| scRNA-seq | Single-cell RNA sequencing |
| SEF | Sum of estimated frequencies |
| Seq | Sequencing |
| SNV | Single nucleotide variants |
| ssDNA | Single-stranded DNA |
| STAT | Signal transducer and activator of transcription |
| TAA | Tumor-associated antigens |
| TAP | Transporter associated with antigen processing |
| TCF-1 | T cell factor 1 |
| TCO | Trans-cyclooctene |
| TCR | T cell receptor |
| TDO | Tryptophan 2,3-dioxygenase |
| $Te_{ff}$ | Effector T cell |
| $T_{ex}$ | Exhausted T cell |
| $T_{FH}$ | T follicular helper cell |
| $T_{H}$ | T helper cell |
| TIL | Tumor-infiltrating lymphocyte |
| TMB | Tumor mutational burden |
| TME | Tumor microenvironment |
| TNF | Tumor necrosis factor |
| TPM | Transcripts per million |
| $T_{reg}$ | Regulatory T cell |
| $T_{rm}$ | Tissue-resident memory T cell |
| TSA | Tumor-specific antigen |
| $T_{scm}$ | Stem-cell memory T cell |
| TZ | Tetrazine |
| VART | Viral antigen-reactive T cell |
| VEP | Variant effect predictor |
| WES | Whole-exome sequencing |

# CONTENTS

# 1 SCOPE OF THESIS

This Ph.D. thesis covers aspects of general T cell immunology, with a focus on immuno-oncology and the role of antigen-specific CD8 T cells in directing clinical response to checkpoint inhibition therapy. The overall objective of this thesis is to evaluate tumor antigen recognition and novel tools for the detection of antigen-specificity, as well as to highlight nanoparticle-based strategies for delivery of therapeutic cargo, in the context of T cells and cancer therapy.

# 2 INTRODUCTION

## 2.1 From Innate to Adaptive immunity

The host's protection against imminent threats such as invading pathogens or cells undergoing malignant transformation relies on several layers of defense and a multitude of immune cells, which provide the host with the ability to recognize non-self and conduct appropriate immune responses. Anatomic and chemical barriers form the first line of this defense. Surfaces in contact with pathogens, namely the skin, oral mucosa, intestine and respiratory epithelium etc. form a physical barrier and possess various chemical and enzymatic systems including anti-microbial compounds and complement, which provide immediate protection for these epithelial barriers. If these epithelial barriers are breached by invading pathogens, various innate lymphoid cells in the vicinity, such as macrophages, natural killer cells, granulocytes and dendritic cells (DCs) sense the threat and coordinate to provide a rapid cell-mediated immune response. This sensing is provided by innate recognition receptors such as pattern-recognition receptors (PRRs), which recognize pathogen-associated and damage-associated molecular patterns. These sensors are strategically located at different cellular locations, e.g. toll-like receptors in the transmembrane regions, and NOD-like receptors and RIG-1-like receptors in the cytoplasm, allowing for thorough and robust detection of foreign antigens. Upon PRR triggering, these innate cells act either directly by phagocytosis to engulf and destroy the pathogen or indirectly by the production of various cytokine and chemokine mediators, which induce inflammation to recruit other immune cells to propagate the response.

The second arm of the immune response, at least in vertebrates, is provided by the adaptive immune system. A key cellular component of adaptive immunity are the lymphocytes, namely B lymphocytes (B cells) and T lymphocytes (T cells), which allow specific responses against an astronomical amount of antigens from the numerous pathogens that the host is exposed to throughout its lifetime and, critically, confers the phenomenon of immunological memory. Lymphocytes can respond to such an array of antigens due to the presence of highly variable antigen receptors on the cell surface, which allow recognition and binding of antigens. Each lymphocyte matures to possess a single variant of this antigen receptor so that the lymphocyte population as a whole expresses an enormous repertoire of antigen-binding specificities, capable of binding any given foreign antigen.

### 2.1.1 The complexity of the TCR-pMHC interaction

In the case of conventional T cells, the T cell receptor (TCR) recognizes antigenic peptides in the context of major-histocompatibility complex (MHC) molecules. More precisely, the specificity of this recognition is determined by the αβ TCR, which is comprised of separate chains assembled from variable (V), diversity (D), joining (J) and constant (C) gene fragments, a process known as somatic gene rearrangement[1]. The stochastic arrangement and assembly of V(D)J segments and the heterodimeric nature of the α and β TCR chains results in an astounding theoretical repertoire of $10^{15}$ unique αβ TCRs in the mouse[2,3]. In humans, this is thought to be orders of magnitude larger, due to the increased number of TCRβ variable genes[4]. The TCR diversity is provided by

six complementarity-determining regions (CDRs), which interact with both the peptide and the MHC molecule[5]. There is a dependency for amino acid sequence on both sides of the peptide-MHC-TCR interaction, i.e. a "double-sided key" and these specific residues govern the binding preference and affinity for the given MHC or TCR. MHC class I (MHC-I) molecules possess a closed peptide-binding groove and as such the length of the antigenic peptide is typically restricted to 8-11 amino acids[5]. Whereas, an open binding groove in MHC class II (MHC-II) molecules permits the binding of longer peptides[6]. There are critical residues in the peptide that permit and specify docking into the MHC binding groove (anchor residues) as well as T cell contact residues that engage on the TCR side of the interaction. For most MHCs, the anchor residues are located in the peptide at positions two and nine (or C-terminus of longer peptides), whereas the residues in contact with the TCR surface are typically internal amino acids[7].

The notion of "one-clonotype-one-specificity" in the proposed clonal selection theory suggested that individual lymphocytes have specificity for a single antigen[8]. Considering the 20 proteinogenic amino acids, the potential array of peptides that can be synthesized and bind to self-MHC is theoretically astronomical ($>10^{15}$), and this does not include peptides containing post-translational modifications e.g., phosphorylation and glycosylation. This indicates that despite the immense theoretical repertoire of TCRs, the number of potential foreign peptide-MHC (pMHC) complexes to which T cells might be exposed still vastly outweighs the TCR availability[1]. This all implies that individual T cells have to be cross-reactive i.e. can respond to a range of different pMHCs, and this has clinical implications in autoimmunity and adoptive cell therapy (ACT). The combination of a specific peptide bound to a particular MHC molecule is the basis of specificity for any given TCR. This is otherwise known as MHC restriction[9]. MHC molecules are highly polymorphic transmembrane glycoproteins, and in humans, are encoded within human leukocyte antigens (HLA) locus. Throughout a population, there are numerous versions of the HLA molecule, which derive from similar but distinct alleles. This polymorphism provides robust population protection as it allows the capacity to display a larger variety of antigenic peptides. An individual will express six different classical peptide-presenting HLA class I molecules (two of each HLA-A, HLA-B and HLA-C) and well as six HLA class II molecules[1]. Non-classical HLA molecules further contribute to this immune complexity and provide additional levels of redundancy and protection; however, for the scope of this thesis, I will leave it at that.

The adaptive immune response, however, would not be possible without the pivotal function of DCs as antigen-presenting cells (APCs), in bridging the innate and adaptive immune system. The routine surveillance of the periphery allows DCs to engulf pathogens or infected/abnormal cells at the site of infection or neoplasm, respectively. Activation of PRRs on DCs stimulates expression of co-stimulatory molecules CD80/86 and lymphoid-homing chemokine receptor, CCR7, on the surface of DCs, which directs the DCs to the nearest lymph node whereby antigen presentation occurs. Naïve T cells, also expressing CCR7, recirculate constantly through peripheral lymphoid tissue, i.e. a draining lymph node, where they encounter DCs bearing and presenting their cognate antigen.

### 2.1.2 Antigen presentation and T cell activation

The thesis presented herein will focus on T cells, due to their inherent ability to recognize peptide antigens, presented on the cell surface by MHC molecules[3]. T cells derive from bone marrow progenitors and migrate to the thymus for maturation, positive and negative selection, and are subsequently exported to the periphery. Central tolerance in the thymus ensures that T cells interacting with self-pMHC ligands are positively selected, and subsequently, those that react to self with a high affinity are deselected and directed for apoptosis[10]. If self-reactive T cells bypass clonal deletion during central tolerance or if cognate self-antigens are first encountered outside the thymus, peripheral tolerance mechanisms are in place to compensate this evasion. There will be more emphasis on this shortly. These processes of immunological self-tolerance prevent undesired auto- and microbiome-reaction, which has implications in cancer and autoimmune disease, as well as in maintaining general immune health.

During antigen processing and presentation, antigens deriving from cytosolic proteins, or exogenous proteins phagocytosed by DCs, are proteolytically processed to peptides through the proteasome and translocated into the endoplasmic reticulum (ER) by transporter associated with antigen processing (TAP). In the ER, peptides are enzymatically trimmed to 9-11 or 11-19 amino acid sequences and loaded onto nascent MHC-I/II molecules, respectively, with the aid of chaperones. Assembled pMHC complexes are then trafficked to the cell surface for presentation to CD8 or CD4 T cells, respectively. A critical phenomenon known as cross-presentation allows DCs to uptake exogenous antigens (e.g. viral particles, or circulating tumor antigens) by endo- or phagocytosis and re-translocate back to the cytosol for proteasomal degradation and presentation on MHC-I[11]. This permits a cytotoxic T lymphocyte (CTL) response even though extracellular antigens would classically involve MHC-II binding and a T helper ($T_H$) response.

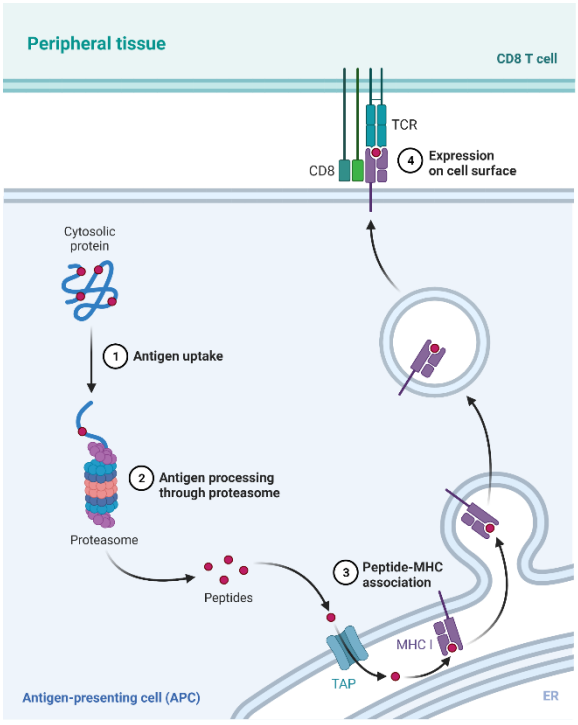


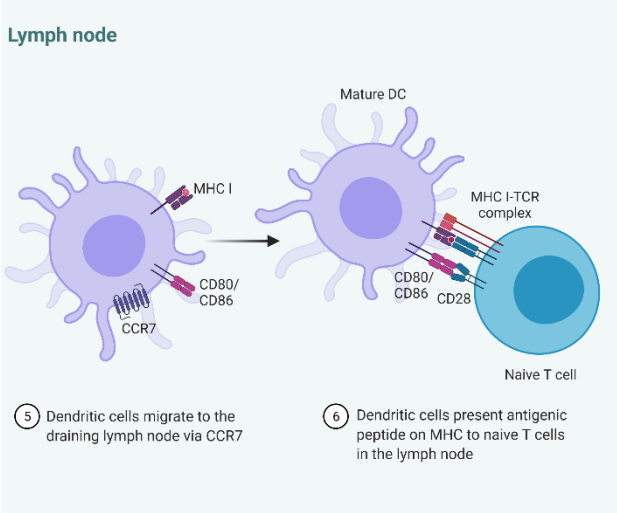

**Figure 1**. MHC class I antigen processing and presentation pathway (left) and antigen presentation to T cells (right). In the peripheral tissues, APCs such as DCs uptake antigen that is then proteolytically processed in the proteasome, whereby short peptide fragments are generated and translocated via TAP to the ER, whereby peptide loading onto nascent MHC-I molecules occurs. The assembled pMHC complexes are then transported to the cell surface for presentation. DCs are directed to the nearest lymph node by a chemokine gradient and the expression of CCR7. In the lymph node, antigen presentation occurs when DCs encounter naïve CD8+ T cells bearing a cognate TCR. TAP, transporter associated with antigen processing; ER, endoplasmic reticulum; TCR, T cell receptor. Adapted from a template on BioRender.com

T cell immunity as a whole must provide immune coverage for all possible foreign peptides that are bound to and displayed by self-MHC molecules. T cell recognition can be partitioned into three major processes or the "three signals": 1) antigen recognition i.e. TCR recognition of cognate pMHC, 2) binding of co-stimulatory molecules CD28 and CD80/86, and 3) cytokine-mediated differentiation and expansion, e.g. IL-2 stimulation.

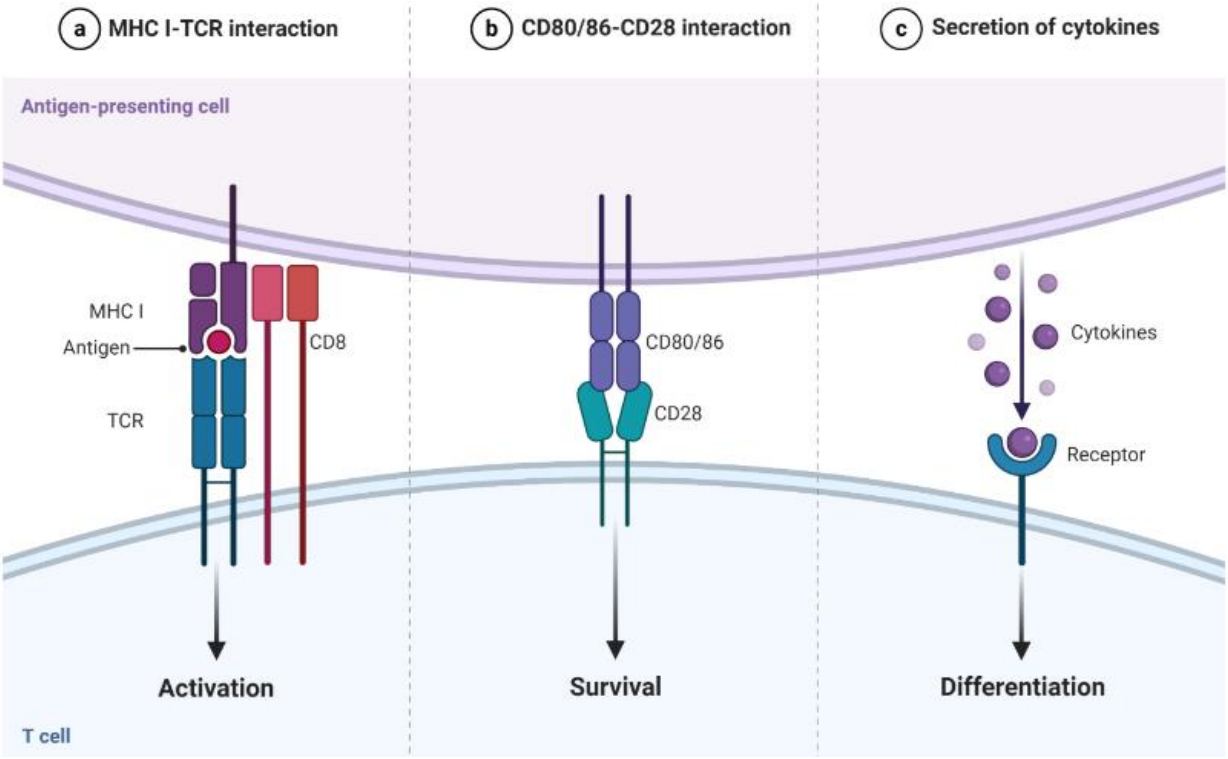


**Figure 2.** The three signals for T cell activation. The first signal (a) occurs when an APC presents pMHC to a T cell bearing a cognate TCR. The CD8 co-receptor binding to MHC-I recruits other factors involved in the assembly of the immunological synapse, resulting in T cell activation. The second signal (b) is provided by the interaction between CD28 on the T cell and co-stimulatory molecules, CD80/86, on the APC, which promotes T cell survival. The third signal (c) is provided by cytokines, e.g. IL-2, which then stimulates the T cell differentiation and expansion. Modified from a template on BioRender.com

## 2.2 T cell development and fate

There are two broad classes of T cells with distinct effector functions, delineated by the expression of either the CD4 or CD8 co-receptor. These co-receptors support antigen recognition and TCR signaling upon antigen engagement, by binding to either MHC-II or MHC-I molecules, respectively. Co-receptor binding results in the recruitment of other factors involved in the assembly of the TCR-pMHC-CD4 or TCR-pMHC-CD8 immune synapses and hence support T cell activation and survival[12].

$CD4^+$ T cells detect their cognate antigen in the context of MHC-II and coordinate with the adaptive immune system by the production of cytokines that are involved in chemotaxis and inflammation[13]. There are multiple subsets that CD4 T cells differentiate into, including $T_H$ -1, -2, -17, which mediate specific types of immune responses depending on the antigen encountered. These subsets primarily act in peripheral tissues at sites of infection or injury. T follicular helper ($T_{FH}$), a subset of CD4 T cells located in the lymphoid tissues, are responsible for B cell interaction and regulation of antibody production in the humoral immune response. Regulatory T cells ($T_{regs}$) are responsible for dampening immune responses in the contraction phase following pathogen clearance, as well as being implicated as a key player in tumor-associated immunosuppression[14] and autoimmunity[15].

$T_H1$ cells mediate type I immunity to intracellular pathogens and tumors via the release of interferon-γ (IFN- γ) and IL-12, which activate macrophages and granulocytes, as well as lymphocytes such as CTLs. $CD8^+$ T cells detect their cognate antigen in the context of MHC-I and are thereby able to survey intracellularly-derived antigens that are displayed on the cell surface, i.e. from a virus-infected or neoplastic cell, and subsequently deploy cytotoxic components to directly destroy the infected or abnormal cell[16]. CTL's secrete enzymes such as perforins and granzymes, which directly induce transmembrane pore formation and apoptosis in the target cell. The interaction of Fas molecules on the surface of target cells with Fas ligand (FasL) on the CTL is another method by which apoptotic signaling may occur[17].

T cell differentiation in the periphery occurs in three phases. Clonal expansion, where activated antigen-experienced T cells expand and differentiate into effector T ($Te_{ff}$) cells that mediate clearance. Contraction, where $T_{eff}$ cells are directed for apoptosis following infection (i.e. peripheral deletional tolerance). Followed by a memory phase, in which a small fraction of primed T cells persists to maintain a memory response[16]. Following antigen encounter and priming, the fate of T cells is dictated by several peripheral tolerance checkpoints that modulate their activity, in terms of both the quality and magnitude of the T cell-mediated response. At the naïve T cell stage, where T cells are capable of responding to new antigens, quiescence and ignorance mechanisms act to prevent steady-state expansion in response to tonic signals i.e. to self-antigens[18]. This state of ignorance has been linked to the self-antigen abundance (as well as TCR affinity) but interestingly, also the anatomical location[19]. In the transition from T cell priming to the onset of the effector stage, mechanisms of anergy prevent potential immunopathology in the context of co-stimulation-deficient or tolerogenic TCR activation[18]. In the absence of appropriate co-stimulation, a hyporesponsive T cell state is induced that is hallmarked by reduced levels of IL-2, IFN-γ and

TNF in response to TCR stimulation. This anergic state is maintained by prolonged antigen exposure, e.g. in chronic viral infections, but may be reversed in absence of antigen[20].

During the effector phase of an acute immune response, $T_{eff}$ cells contract to memory T cells, which maintain long-term immunity to the pathogen. Whilst the majority of $T_{eff}$ cells rapidly contract and do not occur at significant proportions during steady-state, a population of terminal effectors re-expressing CD45RA ($T_{EMRA}$), but not CCR7, can persist in circulation. $T_{EMRA}$ cells are predominantly in the CD8+ T cell lineage and exhibit a low proliferative capacity, characterized by e.g. low levels of transcription factor Ki67, but high levels of effector cytokines IFN-γ and granzyme B (GZMb)[21]. This subset is associated with prolonged infections, as the frequency in the blood correlates with persistent cytomegalovirus (CMV) infection, but also tends to increase with age[22,23]. Memory T cells represent a heterogeneous subset that is sub-divided phenotypically into central memory ($T_{CM,}$ CD45RA- CCR7+), effector memory ($T_{EM,}$ CD45RA- CCR7-) and stem-cell memory ($T_{scm}$, CD45RA+ CCR7+) T cells[16]. Importantly, memory T cells are endowed with the ability for rapid and functional recall responses to a re-encountered antigen and have a lower threshold for antigen responsiveness[18]. $T_{CM}$ maintain a lymphoid-homing profile with high proliferative capacity and tend to migrate to the tissues, whereas $T_{EM}$ remain in circulation and have a higher capacity to produce effector cytokines.

It has recently been established that a transcriptionally distinct subset of memory T cells exists in the tissues, tissue-resident memory T ($T_{rm}$), which have features of resting memory T cells, but express the additional markers CD69 and CD103, which are characteristic markers for an early-activated or tissue-resident state, respectively[24]. These are thought to mediate a more rapid *in situ* protection against various infections, as compared to circulating memory T cells[16]. The relatively rare subset of $T_{scm}$ are able to maintain a high proliferative and self-renewal capacity but exhibit no effector function[25]. This "stemness" can be partially attributed to the expression of T cell factor 1 (TCF-1), a transcription factor generally restricted to naïve T cells, but has been recently observed to be expressed in pre-exhausted or pre-dysfunctional T cells. Critically, TCF-1 seems to be downregulated in terminally exhausted T cells, in the context of chronic viral infections and cancer[26–29].

Upon persistent antigen stimulation, e.g. during chronic infection and in certain cancers, functional memory T cells fail to develop and instead, an exhausted T cell subset ($T_{ex}$) predominates the antigen-specific repertoire. This diverse subset has characteristics including reduced cytokine production capabilities, high levels of inhibitory receptor expression, altered metabolic and transcriptional states, as well as an inability to maintain a state of quiescence or "readiness" observed in memory T cells[18]. The term "exhaustion" can however be quite vague. It was initially thought that $T_{ex}$ cells were defined by the expression of inhibitory receptors e.g., programmed cell death-1 (PD-1), LAG3, TIM3, TIGIT but subsequent studies highlighted that these are not exclusive markers of $T_{ex}$ cells but are also expressed by functional $T_{eff}$ cells, where a dynamic expression exists depending on the localization and differentiation state[30,31]. Furthermore, recent accounts suggest significant differences in $T_{ex}$ cell state in chronic viral infections versus cancer[32]. Although there are phenotypic similarities shared between $T_{ex}$ in either of the scenarios, $T_{ex}$ cells in tumor models exhibit defective effector functions and poor control of tumor growth and

metastasis, whereas Tex in chronic viral infections show functional responses. Additionally, tumor-specific $T_{ex}$ cells seem to arise early after tumorigenesis[33] and this has been attributed to suboptimal priming of T cells. Contrasting with viral infection models, where an initial T cell stimulation does occur appropriately[34]. Rather than there just being exhausted T cells in the tumor microenvironment (TME), there seems to be evidence for a broader collection of dysfunctional T cells comprising both exhausted and anergic[18]. Due to the lack of key immunogenic features in most cancer types, i.e. HLA downregulation as well as the suppression of co-stimulatory molecules and proinflammatory cytokines, there is sub-optimal priming of T cells in the TME, which results in anergic tumor-specific T cells[18]. Additionally, since anergy occurs very early after T cell activation, there may be a considerable amount of T cells in the anergic state as opposed to the exhausted state[34].

When T cells reach the stage of terminal differentiation, they can adopt a state of senescence. This is represented by proliferative arrest that is induced when cells come to the end of their replicative potential or are subject to stressors such as hypoxia, reactive oxygen species and low pH[35]. Senescent T cells have been shown to display surface markers such as CD45RA and CD57, but do not express costimulatory receptors CD27 and CD28. CD57 is generally characteristic of late-differentiated or potentially senescent T cells[22], whereas, CD27 is induced upon T cell activation

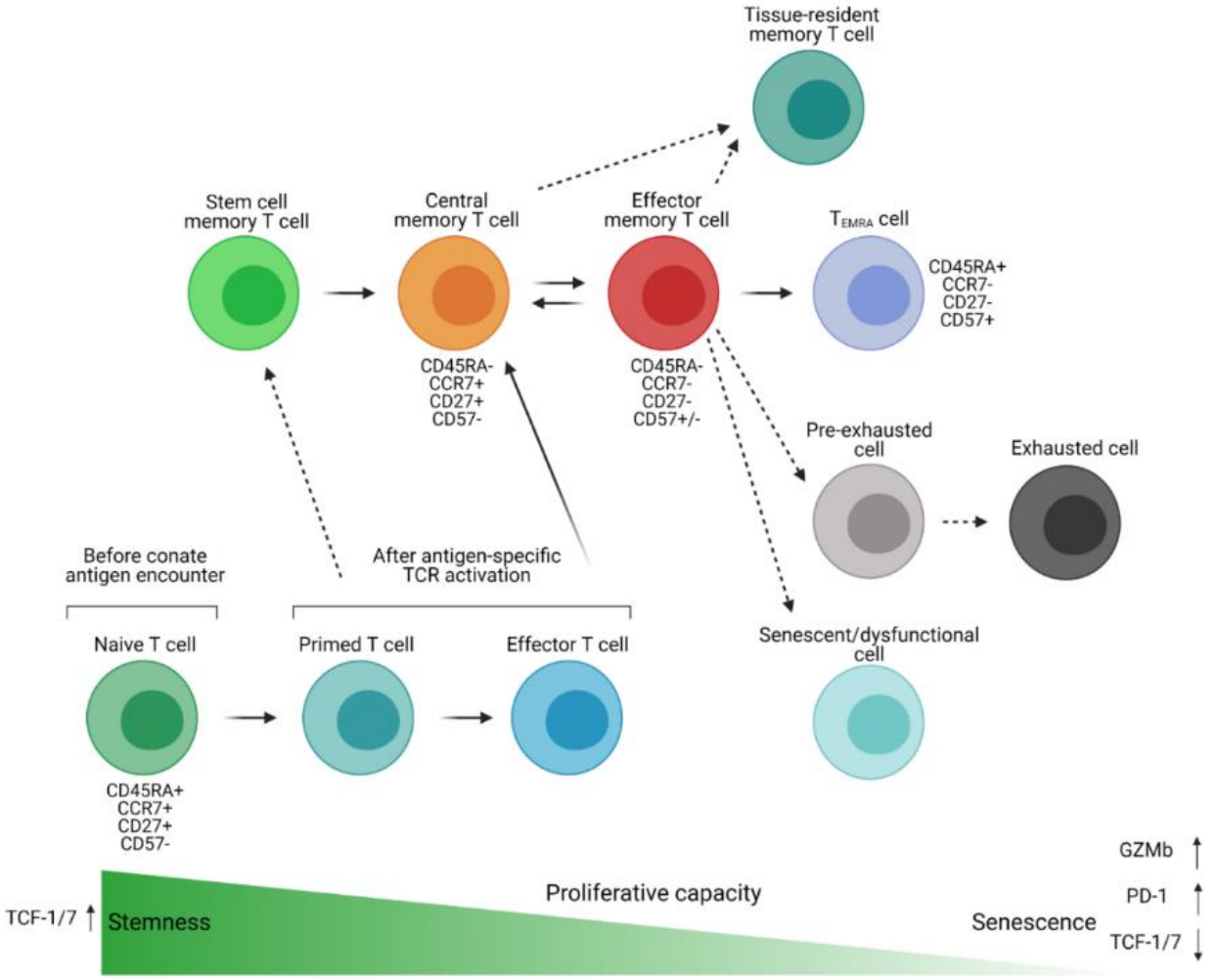

**Figure 3**. Schematic of T cell differentiation and a simplified representation of the phenotypic state of relevant T cell subsets. Upon naïve T cell priming, a small pool of antigen-reactive T cells persist as various subsets of memory cells, which provide long-term immunity. As T cells progress towards a terminally differentiated state, various dysfunctional or senescent subsets arise before eventually transitioning to terminally exhausted state, characterized by low proliferative capacity and reduced self-renewal capabilities. Created with BioRender.com

and is viewed as an early differentiation marker[36]. The replicative potential relates to the gene telomere length, as telomere shortening has been described as an aging-induced effect[37]. In contrast to $CD27^{+}CD28^{+}$ T cells, senescent T cells have short telomeres so they lose CD27 and CD28, whilst re-expressing CD45RA[38]. Contrasting to $T_{ex}$ cells, senescent cells do not exhibit compromised effector function but transition to a secretory state characterized by increased pro-inflammatory and suppressive cytokine production, regardless of their lack of proliferation[38,39]. Overall, it is becoming increasingly evident that the development, differentiation and maintenance of T cells are dynamic processes that change throughout an individual's lifespan.

## 2.3 Immuno-oncology

Since the hallmarks of cancer have been described back in the early 2000s, novel mechanisms governing malignant transformation and metastasis have been uncovered. Other than the classical mechanisms such as genome instability, the resistance of cell death, and induction of angiogenesis; there are other mechanisms whereby tumor cells avoid immune detection and destruction[40]. The latter has a huge significance regarding immune system modulation and the ability for detection and clearance of malignant cells. Tumor cells can persist in the body due to mechanisms that evade and suppress immune responses towards these cells.

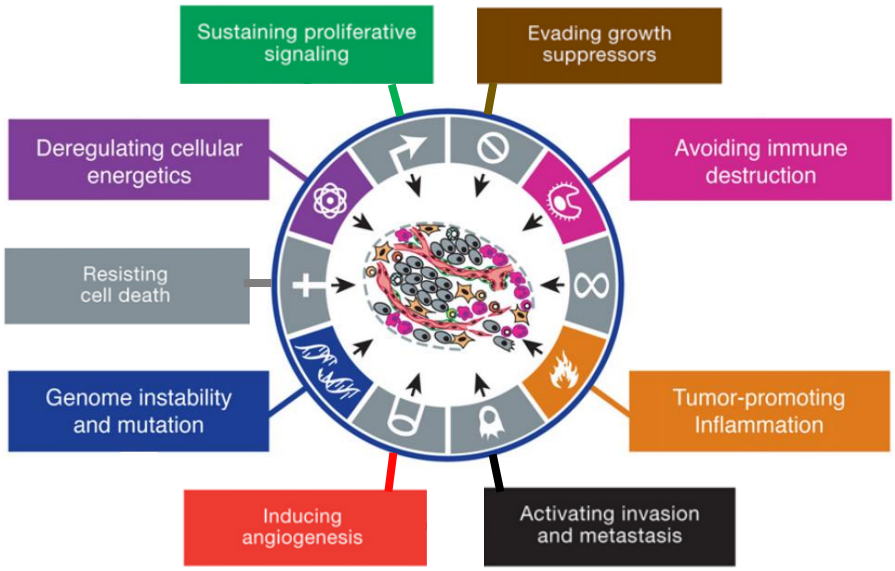


Figure 4. Emerging hallmarks and enabling characteristics of cancer. Although all of the highlighted parameters contribute to tumorigenesis, for the scope of this thesis, the characteristics of avoiding immune destruction and tumor-promoting inflammation are of most relevance in relation to immune system's regulation of tumor outgrowth. Modified from[40].

Solid cancers develop within a heterogeneous TME composed of various cellular and non-cellular components, including innate and adaptive immune cells, stromal cells and vascular networks. The TME of solid malignant tissues has been a major obstacle in cancer therapy and understanding this intricate, dynamic ecosystem has been of great interest[41]. The immune cell component of the TME comprises effector cells, e.g. CTLs, CD4 $T_H1$ cells, natural killer (NK) cells; as well as tumor-suppressor cells such as Tregs, tumor-associated macrophages (TAMs) and myeloid-derived suppressor cells (MDSCs)[42]. As well as being immunosuppressive, the TME is under metabolic stress due to oxygen and glucose deprivation[42].

The density and heterogeneity of the TME is closely associated with treatment prognosis and efficacy, and as such, modulating this environment may serve as an immunotherapeutic strategy. The TME can be generally characterized as hot (T cell inflamed with features of immune activation) or cold (non T cell inflamed with features of T cell absence or exclusion), which is primarily due to levels of inflammatory cytokine production and T cell infiltration[43]. Hot tumors generally respond favorably to immunotherapeutic strategies such as immune checkpoint inhibition (ICB), and thus, there is much focus on converting cold non-inflamed tumors to hot ones to achieve a better treatment outcome[43].

### 2.3.1 Cancer immunoediting

As highlighted in the section above, there is a complex interaction between the developing tumor and the immune system component within the TME. A process known as cancer immunoediting describes the delicate balance whereby immunity can either provide protection against tumor development or on the other hand, allow immune escape and promote tumor outgrowth[44]. The three classical E's of cancer immunoediting, elimination, equilibrium and escape, are depicted in Figure 5. The elimination phase involves immunosurveillance, whereby innate and adaptive immunity allows detection and destruction of the tumor. Specifically, this involves DCs, macrophages, NK, NKT, γδ T cells, CD4 and CD8 T cells, as well as a host of cytokines and effector molecules, e.g., IFN α/β, IFNγ, tumor necrosis factor (TNF), interleukin (IL)-12, perforin and TRAIL[44]. In the case of immunogenic tumors, the recognition of tumor-associated antigens (TAA) or tumor-specific antigens (TSA) is the main driver for the elimination phase, which relies on T cells. This will be elaborated further in the following section.

The equilibrium phase occurs when the residual tumor cells remain in a state of dormancy after the immune system is unable to eliminate them. The progression of a tumor from equilibrium into escape depends on alterations of the TME, and consequently, editing of the tumor's immunogenicity. This state of equilibrium can last the lifetime of an individual. This may seem favorable for cancer therapeutics; however, the longer the duration of equilibrium promotes further immunoediting and allows tumors to become more resistant to immune-mediated cytotoxicity[45]. The TME of tumors in immune equilibrium contains increased numbers of NK cells, CD8 T cells and γδ T cells, as well as reduced numbers of Tregs, MDSCs and NKT cells, as opposed to the TME of escape tumors[46]. Additionally, the presence of tertiary lymphoid structures, containing B cells, within the TME, has been shown to provide a favorable prognosis for melanoma patients undergoing immunotherapy[47]. However, the balance of immune effector and suppressor cells

ultimately determines the progression from immunological maintenance of tumors to immunological evasion.

The escape phase of cancer immunoediting involves uninhibited and progressive tumor outgrowth. There are numerous tumor-intrinsic and -extrinsic mechanisms of immune escape and the list is ever-expanding, however, the focus here will be on those that are a direct result of immune pressure on the tumor and the consequent inability for immune recognition and/or increase in immune suppression[44,48]. Reduced immune recognition is a key mechanism of tumor-mediated immune escape, and is driven largely by the downregulation of MHC-I expression and the consequent loss of antigen processing and presentation function on tumor cells. A recent study relating to metabolic stress in the TME reported that simultaneous exposure to low glucose and oxygen levels resulted in decreased MHC-I surface expression on tumor cells, driven by compromised activation of signal transducer and activator of transcription (STAT)-1[49].

Another fundamental mechanism of tumor-mediated immune evasion is the escape via suppression of T cell responses. The skewing of $T_H1$ responses is a primary contributor to ineffective anti-tumor responses and progression from immune equilibrium, as escape tumors typically display altered $T_H1$ signatures[44]. In the elimination phase, the TME is predominated by $T_H1$-like cytokines, e.g. IL-12, IFNγ and TNF-α, but when the balance shifts to favor suppressor cells, TAMs and MDSCs promote a $T_H2$-like signature by the release of IL-10, IL-6 and IL-4 in the TME[50,51]. The $T_H2$ bias results in further escape-promoting mechanisms such as angiogenesis and immune-suppressive factors e.g. TGF-β and VEGF[52]. Increased TGF-β secretion in the TME induces CD8 T cell exhaustion through upregulation of the transcription factor, MAF[53], as well as promoting the accumulation of other suppressor cells e.g. $T_{regs}$. There is also metabolic inhibition of T cells in the TME by upregulation of enzymes responsible for tryptophan catabolism, e.g. indoleamine 2,3-dioxygenase 1 (IDO1) and tryptophan 2,3-dioxygenase (TDO), and synthetic inhibitors of such enzymes have been effective in restoring anti-tumor immunity in mouse tumor models[54].

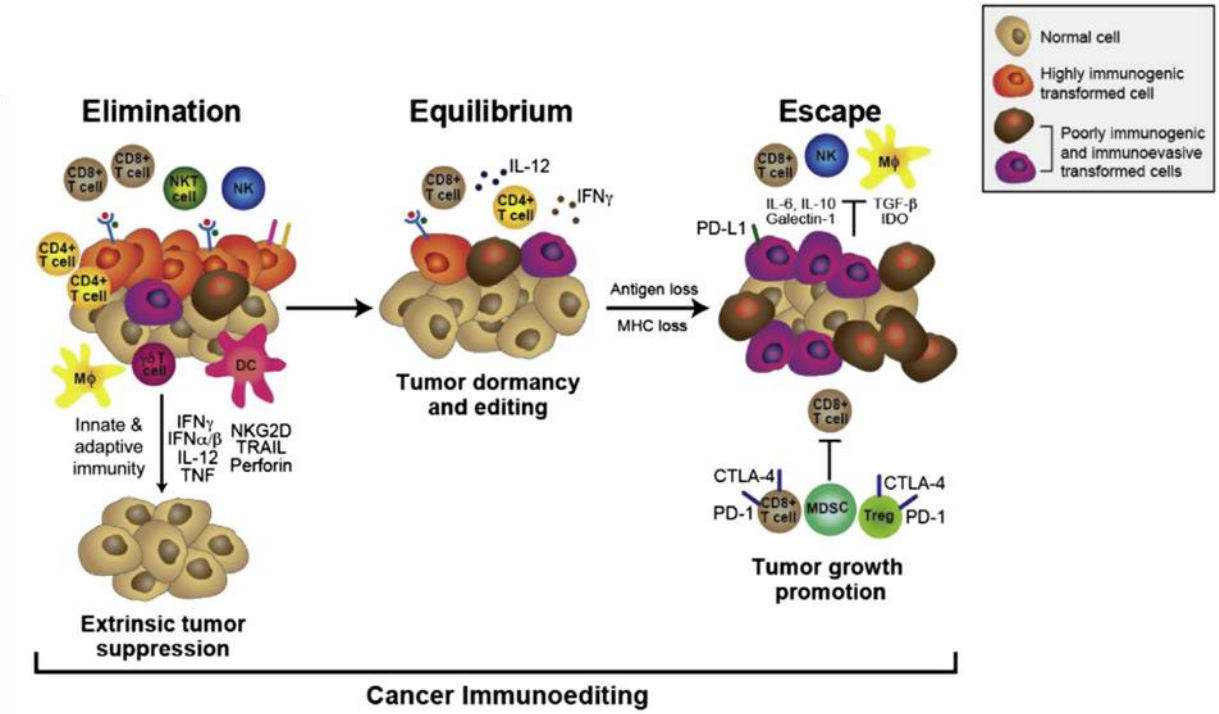


Figure 5. The three classical E's of cancer immunoediting, represented by an elimination, equilibrium and escape phase. The balance between the three phases ultimately dictates whether a tumor is eliminated by the immune system, or progresses to immune escape and results in uncontrollable tumor outgrowth. Amended from[44]

For this thesis, perhaps the most relevant mechanism of tumor-mediated immune suppression is the expression of inhibitory ligands that engage with inhibitory receptors on immune cells within the TME. Upon respective ligand-receptor interaction on the tumor cells, a state of T cell exhaustion or dysfunction is induced within the TME, which hinders tumor-specific T cell responses. Aspects of T cell exhaustion have already been discussed, and inhibitory receptors will be elaborated further in the cancer immunotherapy section. For now, the T cell targets in cancer will be introduced and the aspects of their detection and use in the clinics will be outlined.

### 2.3.2 Tumor antigens and their detection

The different classes of tumor antigens are generally segregated based on their tumor specificity i.e. how restricted they are to cancer tissues versus normal healthy tissue. Those of low tumor specificity are generally tumor-associated and are represented by differentiation antigens or antigens that are overexpressed in tumors. In the case of melanoma, where there is CTL recognition of tumor cells as well as normal melanocytes, differentiation antigens deriving from Melan-A, tyrosinase and GP100 are examples of where incomplete tolerance has occurred for these melanocytic antigens[55]. Other than melanoma, there are differentiation antigens that exist in prostate cancer, e.g. prostate-specific antigen, which is absent from other tissues. Using a strategy of reverse immunology, antigenic peptides derived from such proteins have been utilized for therapeutic immunization[55]. The overexpression of proteins by tumors also provides an opportunity for antigen-specific T cell responses, e.g. in the case of HER2-expressing cancers of

epithelial origin, such as ovarian and breast carcinomas[55], as well as MUC1-overexpressing adenocarcinomas[56]. However, signatures of tumor-specific overexpression can be difficult to characterize rigorously, as methods of quantitative PCR and immunohistochemistry that are generally applied do not provide complete resolution of the tumor heterogeneity.

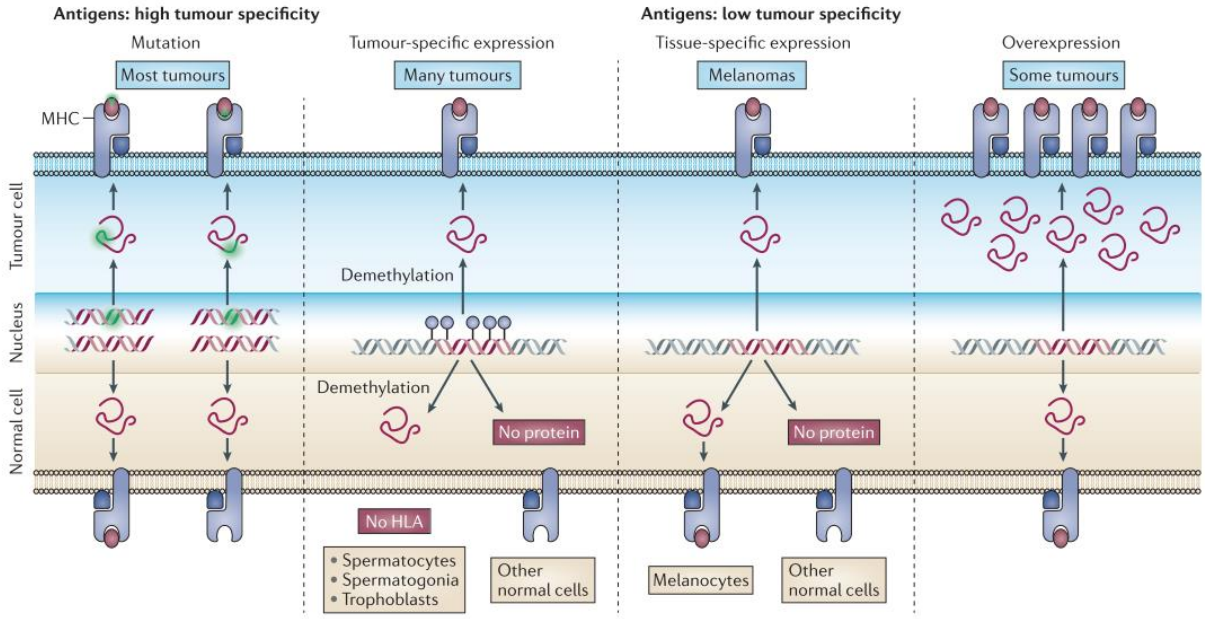


Figure 6. Classification of tumor antigens. Antigens of high tumor specificity to the left, represented by mutation-derived neoantigens as well as oncoviral and cancer-germline antigens. Antigens of low tumor specificity to the right, represented by differentiation and overexpression antigens. Amended from[55]

On the other hand, antigens of high tumor specificity represent more favorable immunotherapeutic targets based on the potential for a selective anti-tumor response. Tumor-specific antigens include oncoviral antigens, antigens encoded by the germline genes as well as mutation-derived neoantigens. Antigens of viral origin are prominent in subsets of cancers including Merkel cell carcinoma and cervical carcinoma, among others[57,58]. Antigens deriving from cancer-germline genes, otherwise known as cancer-testis antigens, possess tumor specificity due to the aberrant demethylation that seems to occur more frequently in advanced tumors[55]. These germline genes, e.g. from the MAGE gene family, are usually in a methylated state and dormant in normal tissues apart from the germline cells. Whereas, the increasing state of hypomethylation associated with tumor progression results in these germline genes being expressed in a substantial fraction of tumors. Furthermore, since trophoblasts and male germ cells are immune-privileged sites, tolerance is not established towards these antigens and hence they are seen as non-self when expressed by tumors[59]. Based on this principle, hypomethylating agents such as azacitidine have been utilized in the clinic in an attempt to boost cancer-germline antigen T cell responses in tumors[60].

### 2.3.3 Mutation-derived neoantigens and their prediction

Somatic mutations that give rise to nonsynonymous amino acid alterations may generate novel antigens that are normally absent from the human genome. Neoantigens, or non-self-antigens deriving from somatic mutations, are formed by tumor-specific DNA mutations that result in novel protein sequences. Neoantigens are highly tumor-specific, as they are not expressed in healthy tissue; they are foreign and have not been involved in central immune tolerance, so they serve as ideal immunotherapeutic targets[61].

They are, however, also highly patient-specific i.e. personalized, due to a lack of conservation in tumors across individuals, and therefore such therapies have to be tailored to the individual patient. There is also the additional complexity of intra- and inter-tumoral heterogeneity, where the mutational landscape is not homogenous both within a tumor mass and between different metastases[62]. This further complicates the design of neoantigen-based therapies for the clinic. According to the evolutionary phylogenetic tree proposed for primary tumors, within the tumor mass, there are different subclones that arise during tumor development[62]. These subclones possess both shared and private somatic mutations. The trunk of the phylogenetic tree contains shared or public mutations which are directly associated with tumorigenesis (driver mutations), and hence occur early in tumor development. As the tumor mass develops various subclones branch off the tree and are associated with private mutations that are only present in a particular region of the tumor. These are typically characterized as passenger mutations, as they occur later in tumorigenesis and are not responsible for driving the initial neoplastic transformation. The concept of clonal and subclonal neoantigen burden, and their relationship to overall survival was evaluated in primary lung adenocarcinomas and melanoma[63]. This study highlighted that tumors enriched in clonal neoantigens, as opposed to subclonal, were more sensitive to treatment with immune checkpoint blockade.

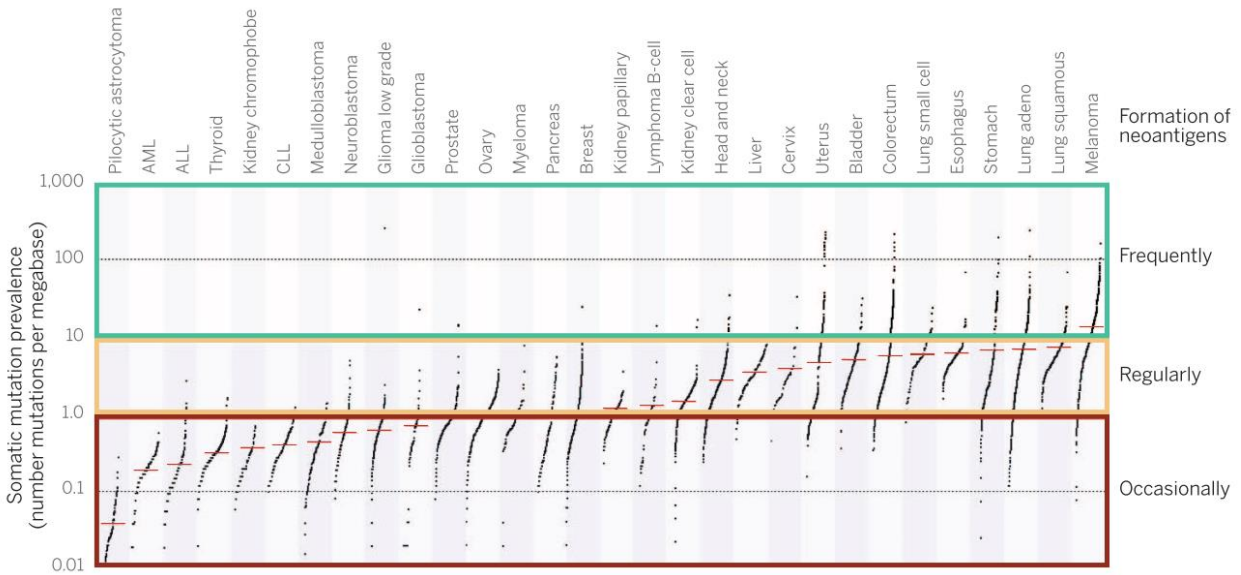


Figure 7. Mutational landscape and estimate of neoantigen repertoire in human cancers. Each data point represents an individual tumor. Tumor types to the left depict categories of low somatic mutational prevalence and therefore infrequently result in the formation of neoantigens. Whereas, those to the right depict categories that have a high mutational prevalence and hence have a greater neoantigen repertoire. This plot depicts both tumor heterogeneity between different tumor types (left/right), but also inter-patient heterogeneity among the same tumor types (up/down). Amended from[61].

All these layers of tumor heterogeneity necessitate the use of genome-based approaches to identify the neoantigen landscape for each given patient. Deep-sequencing technologies have facilitated this and enabled the use of the exome, i.e. the protein-encoding region of the genome, to predict neoantigens and their corresponding neoepitopes[64]. The technological pipeline for predicting neoantigens starts from obtaining tumor material and normal tissue for whole-exome or RNA sequencing to identify tumor-specific mutations within the expressed genes. This is proceeded by the generation of peptides *in silico* and the filtration through prediction algorithms such as the mutant peptide extractor and informer (MuPeXi) tool, whereby mutant peptide lists of single-nucleotide variants and insertions and deletions (indels) are generated and prioritized based on HLA-binding affinity, similarity to self-peptides, expression level and mutant allele frequency[65]. Since a predicted neoepitope does not necessarily imply induction of T cell reactivity, the resulting neoepitope sets are then evaluated for T cell recognition with MHC multimer-based screening approaches or functional assays[61]. This will be elaborated on in the upcoming section.

Out of the many potential neoepitopes identified across the different cancer types, only a small fraction, on average 1-2%, of these neoepitopes are immunogenic i.e. recognized by T cells[61,66]. Indeed, it has been demonstrated that tumor-infiltrating lymphocytes (TILs) from melanoma patients were only able to recognize 1 out of 11 neoantigens that were recognized by healthy donor CD8 T cells[67]. Moreover, it has been shown through cancer exome-based screens that the majority of CD8+ T cell neoantigen responses (92%) are directed at passenger mutations, and not driver

mutations or oncogenes[61]. In an ideal world, the majority of predicted neoantigens would originate from essential oncogenes and they would be shared among larger patient groups. This would decrease the potential of immune escape and more readily facilitate the development of off-the-shelf therapeutic strategies. This is unfortunately not the case. Due to the limited availability of patient material and low frequencies of neoantigen-specific T cells, isolation of reactive T cells and validation of putative neoepitopes at a large scale remains a challenge. In a novel approach, neoantigen-reactive T cells may be induced from healthy donor T cell repertoires, utilizing messenger RNA (mRNA) transfection of DCs to prime autologous naïve $CD8^+$ T cells. This involves endogenous antigen processing and presentation, so it has more biological meaning than the use of MHC multimers presenting minimal epitopes[68].

### 2.3.4 Detection & monitoring of antigen-specific T cells

Techniques utilizing the interaction between a pMHC complex and its given TCR have been applied for the detection and interrogation of antigen-specific T cells over the recent decades (Figure 8). Early methodologies applied for the characterization of T cell recognition utilized functional assays based on cytokine secretion, e.g. ELISPOT, which are generally of low sensitivity and rely on the secretory capacity of T cells[69]. Methods such as this are low-throughput, but at least provide a functional readout of T cell recognition. The use of fluorescently labeled streptavidin molecules to assemble pMHC tetramers enabled the parallel analysis of T cell recognition by flow cytometry[70]. Additionally, the development of production methods for the generation, folding and purification of stable pMHC-I complexes, facilitated by the incorporation of conditional UV ligands and peptide exchange technology, greatly reduced the constraints associated with the utilization of large pMHC libraries[71–73]. On the other hand, development in the field of MHC-II multimers has not been quite as successful, due to various production and peptide prediction challenges[74].

In an attempt to increase the complexity of MHC-based screening approaches, protein-based pMHC microarrays have been explored but were however still limited by detection sensitivity and reproducibility compared to flow cytometry-based techniques[74]. Since then, several MHC multimer-based technologies have focused on improving assay complexity and sensitivity, to allow for a larger range of peptides to be screened and to permit the detection of frequently rare antigen-specific T cell populations[75]. Hadrup *et al*. developed a two-dimensional combinatorial, color-based approach to the encoding of pMHC-I multimers[76]. This approach had the capacity for including up to around 40 unique pMHC-I specificities in a single assay, whilst permitting the recovery of viable cells post-screening for subsequent analysis. This color-based approach, however, has the limitation of overlap of fluorophore emission spectra and hence is not feasible for larger peptide libraries. Mass cytometry approaches incorporated with combinatorial tetramer staining, e.g. CyTOF, removed the caveat of spectral overlap by using heavy-metal isotope tags and allowed up to around 100 pMHC-I specificities[77]. However, due to the destruction of cells, subsequent post-sort analysis is not feasible.

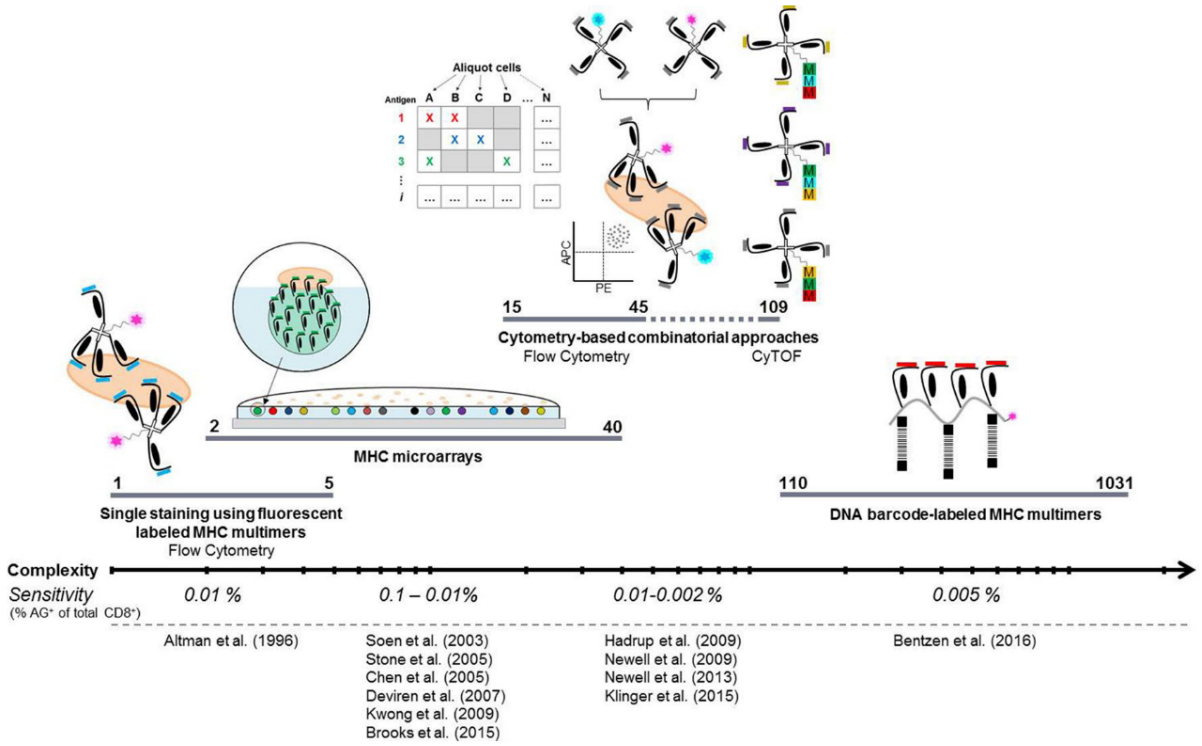


Figure 8. Evolution of MHC-based technologies. Such methodologies initially could screen for only a handful of antigen-reactive T cells in a single assay, with low sensitivity. Over the years, the capacity for detecting a larger range of antigen-reactive T cells (complexity) has increased exponentially, with a corresponding increase in the detection sensitivity. Allowing for the detection of low-frequency antigen-reactive T cells. $AG^+$, antigen-positive; CyTOF, cytometry by time-of-flight. Amended from[75]

Despite advancements in the complexity of antigen-specific T cell detection, the tetrameric form of pMHC multimers may suffer from insufficient sensitivity for the detection of T cells with low-affinity TCRs[78]. This is particularly problematic for T cells bearing low-affinity TCRs in the case of autoimmunity and anti-tumor immunity, where thymic selection eliminates T cells with a high affinity for self-antigens[79]. As well as in the case of antigen-specific CD4+ T cells[80], where frequencies of specific CD4 T cells are lower[81] and supposedly a weaker TCR-pMHC interaction exists[82].

To address this shortfall, higher-order pMHC multimers such as dextramers and dodecamers have enabled a 2- to 5-fold higher sensitivity in the detection of specific CD8+ T cells compared to the corresponding tetramers[83,84]. At the forefront of this technology, DNA barcode-labeled MHC multimers represent the essence of a sensitive high-throughput assay for screening for antigen-specific T cells in peripheral blood[75,85]. This molecular encoding technology, developed by Bentzen *et al*., utilizes a DNA oligonucleotide (oligo) barcode to tag and identify a given pMHC complex, allowing for pooling of >1000 T cell specificities in a single tube assay. The pMHC molecules with corresponding DNA barcodes are multimerized on a dextran backbone for increased avidity to T cells. Following T cell staining, fluorescence-activated cell sorting (FACS) allows the specific isolation of multimer-binding T cells, and the corresponding DNA barcodes

can be sequenced to inform the identity of T cell-reactive pMHCs. An important advantage of this technique is that cells can be analyzed post-sort, e.g. by *in vitro* functional assays. Moreover, not only does the barcode tag remove the capacity limitation of using either fluorescent or metal labels, but also ensures that the measurement of T cell recognition is based on sequencing reads and not just signal intensity from the flow cytometer.

Although these MHC multimer-based technologies have provided a quantum leap for the interrogation of antigen specificity, they still lack the aspects of endogenous processing and presentation, as well as the functional recognition by T cells. Since the binding of MHC multimers to T cells does not necessarily imply an associated functional T cell response, it can be difficult to infer the immunogenicity of the peptide antigen. An alternative strategy, e.g. the T-Scan approach, utilizes lentiviral delivery of antigen libraries and a reporter for GZMb activity, to identify antigens productively recognized by T cells[86]. This, however, is mentioned more as a perspective and will not be elaborated further. For now, the concept of cancer immunotherapy will be introduced, and insights into novel strategies to boost T cell-mediated elimination of cancer will be outlined.

## 2.4 Cancer immunotherapy

The concept of utilizing the immune system as a tool to treat cancer has been around since the nineteenth century[87] and recently, immunotherapy has revolutionized the therapeutic approach to treat metastatic disease. As the number of patients eligible for immunotherapy increases, and the molecular and biochemical basis of the tumor-specific immune responses are resolved, novel druggable targets and new treatment combinations continue to expand the realm of immune-based therapies in the clinic. Strategies of ACT, such as tumor antigen-specific T cell transfer, TCR engineering and chimeric antigen receptor therapy, as well as therapeutic cancer vaccination, despite being very prominent in the clinic, are out of the scope of this thesis. As such, the following section will focus on the unequivocal role of T cells in mediating response to one of the primary cancer immunotherapeutic strategies, ICB.

### 2.4.1 Principles of ICB

There are several evolutionarily conserved negative regulators of T cell activation, i.e. checkpoint molecules, which modulate immune responses and prevent hyperactivation. Out of the many checkpoint molecules expressed by T cells, CTLA-4 and PD-1 are the most noteworthy and dominate the clinic. There is a low basal expression of CTLA-4 in conventional T cells, but a strong upregulation occurs following activation with antigen. CTLA-4 functions to restrain T cell activation by directly antagonizing the interaction between CD28 and CD80/86 at the immunological synapse[88], thereby providing one of the mechanisms of peripheral tolerance. However, $CD4^{+}FoxP3^{+}$ $T_{regs}$ express CTLA-4 constitutively, and hence elicit an immunosuppressive function[89]. In general, blockade of CTLA-4 has been shown to have its primary effect in the T cell priming phase in lymphoid organs by boosting $T_{eff}$ responses, but also by depleting intratumoral $T_{regs}$. Ultimately resulting in an enhanced breadth of tumor antigen-specific T cells[90].

Analogous to CTLA-4, the expression of PD-1 is induced on T cells following TCR stimulation as a function of suppressing T cell-mediated immunity. The ligands for PD-1, homologs of CD80/86, i.e. programmed death-ligand 1 (PD-L1) and PD-L2, are constitutively expressed on

DCs but are also present on tumor cells[91]. Since the Food and Drug Administration (FDA) approval of the PD-1 antibodies, pembrolizumab and nivolumab, for the treatment of refractory melanoma and non-small-cell lung carcinoma, there have been numerous successful clinical trials in various cancer settings, reviewed in[90]. Further expanding the application of these blocking antibodies to various other cancer types such as Hodgkin lymphoma, renal cell carcinoma and colorectal cancer with a high degree of microsatellite instability (MSI) or DNA mismatch repair[92]. This demonstrates the versatility of PD-1 blockade. In contrast to CLTA-4 blockade, PD-1 blockade seems to have a broader clinical utility and this may be attributed to the fact that tumors involve the PD-1 axis via the ligands expressed, so there can be a preferential effect in the TME[93]. Whereas, the immunoregulatory circuitry of CTLA-4 is broader and hence the effect is somewhat more complex[94].

As expected, however, there are clinical complications associated with blocking such natural immunoregulatory mechanisms, as the normal tolerogenic boundaries for self-tissues may not be upheld. A glimpse into the potential spectrum of autoimmune responses induced by checkpoint blockade therapy has been provided by the use of *Ctla4*- and *Pdcd1*- knockout mice[95,96]. A common immune-related toxicity is a loss of naïve T cells and the accumulation of hyperactive memory T cells, which cause inflammatory damage in peripheral organs such as the gastrointestinal tract and lungs[97]. Whereas, more severe autoimmune complications are reported in 30% and 15% of patients treated with CTLA-4 and PD-1 blocking antibodies, respectively[98].

The next section will focus primarily on PD-1 axis blockade and aspects of why many treated patients do not show a favorable response.

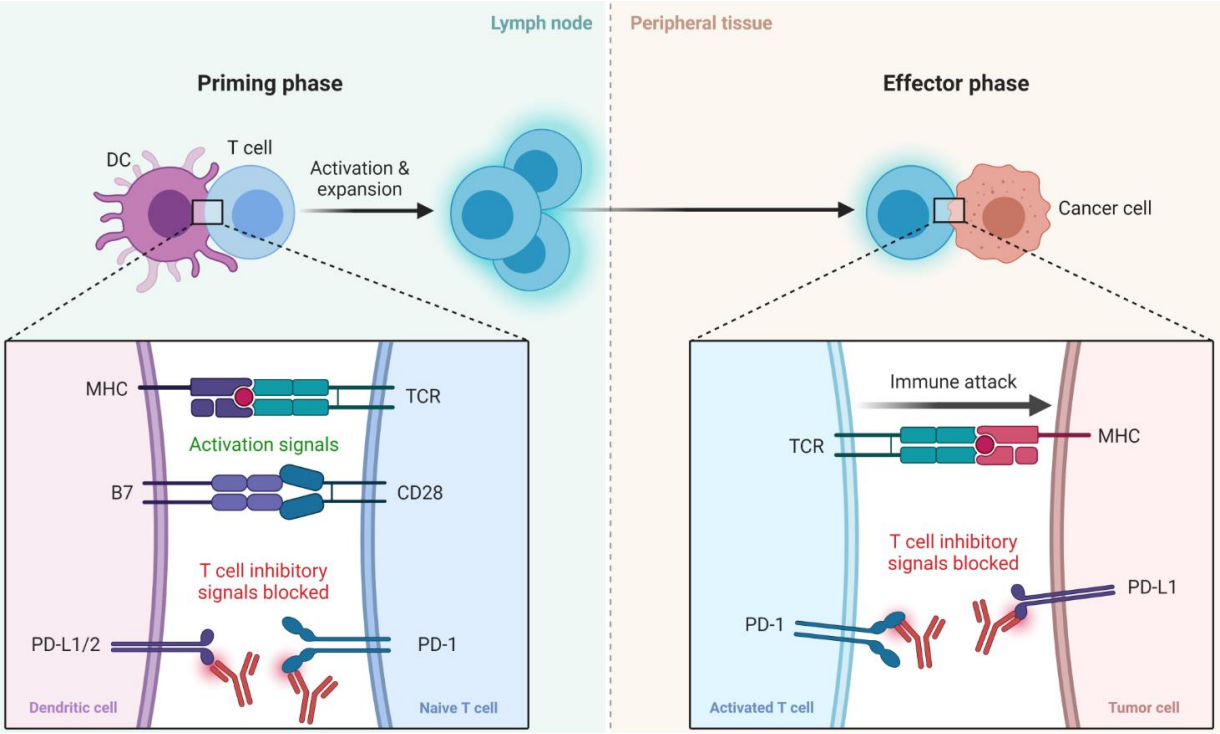


Figure 9. Mechanisms of PD-1 axis blockade. Blocking of the PD-1 axis by the administration of α-PD-1 or α-PD-L1/2 prevents the inhibitory interaction that occurs in both the priming phase in the lymph node, but also the effector phase in the TME. Ultimately promoting T cell activation and proliferation to unleash the anti-tumoral T cell response. Adapted from a template on BioRender.com

### 2.4.2 Dynamics of PD-1 axis blockade

Blockade of the PD-1 axis, i.e. with α-PD-1/PD-L1, is thought to mediate its therapeutic effect in both the priming sites and TME, since interactions occur between both the T cells and DCs, but also T cells and tumor cells[90]. Despite substantial clinical response rates of PD-1/PD-L1 blockade, still, only a relatively small fraction of cancer patients respond favorably. This is partly due to the lack of TILs, e.g. the influx of $CD8^+$ and $T_H1$ cells in the TME has generally been associated with improved prognosis[99], but it is becoming evident that other resistance mechanisms are at play. A recent study on single-cell TCR sequencing of tumor-infiltrating cells showed that PD-1 blockade does not significantly alter the tumor-infiltrating $T_{ex}$ cell population, but rather prevents *de novo* generated tumor-specific $T_{eff}$ from becoming exhausted, implying more of an effect on the magnitude of the T cell response rather than the breadth[100]. In a recent study on the analysis of ACT products, it was observed that most $CD8^+$ TILs reactive towards tumor antigens express CD39 and are in a terminally differentiated state, which was associated with poor TIL persistence. However, a CD39-negative, stem-like memory-progenitor state has been associated with TIL persistence and complete tumor regression[101]. In general, CD39 is upregulated following recent antigen exposure and allows discrimination of tumor-reactive versus bystander CD8+ T cells, but has been linked to a dysfunctional, terminally differentiated phenotype[102–104].

As previously mentioned, anergy is a tolerogenic mechanism that seems to be co-opted by and characteristic of the TME. Anergy in the TME is related to insufficient or sub-optimal priming of tumor-specific T cells, and this has recently been reported to undermine the favorable impact of

PD-1 blockade as preexisting T cell dysfunction may be exacerbated. It was reported that when PD-1 blockade occurs under suboptimal T cell priming conditions, a dysfunctional population of PD-1$^{+}$CD38$^{hi}$CD8$^{+}$ cells was generated and resulted in α-PD-1 resistance and poorer therapeutic outcome[34]. A noteworthy finding was that this suboptimal priming-induced resistance could be reversed by appropriate antigen stimulation, further supporting the notion that these anergic cells seem to dominate the tumor antigen-specific CD8 T cell pool. The same study elucidated that the particular dysfunctional CD8$^{+}$ T cell subset can be used for prognostic purposes in both the tumor and blood, and it may be a "biomarker" of α-PD-1 resistance. It was sown that progressive disease patients exhibited increased numbers of dysfunctional PD-1$^{+}$CD38$^{hi}$CD8$^{+}$ T cells in the TME and blood, compared to the disease control patients.

### 2.4.3 Immune predictors for ICB

There is also the potential for proteins involved in the PD-1 axis to serve as an immune predictor for clinical outcome[105], as in general tumors presenting increased PD-L1 expression respond favorably to PD-1 axis blockade[106]. Other than PD-L1 expression on tumor cells, additional factors have been reported to contribute to the success of PD-1/PD-L1 therapy. Preferentially superior responses have been observed in patients presenting a higher TMB, where there is an increased prevalence of mutation-derived neoantigens and thus an increased probability of tumor-reactive T cells[107]. This implies that patients with tumors harboring more mutations have a larger T cell repertoire and that when checkpoint inhibition therapy "removes the brakes of the immune system" there is a stronger antigen-specific T cell response against the tumor.

As previously mentioned, tumors with high T cell infiltrates i.e. hot tumors, such as desmoplastic melanoma[108], Merkel cell carcinoma[109] and MSI$^{high}$ tumors[110] respond more favorably to ICB. This was similarly demonstrated with α-PD1 therapy (Pembrolizumab) in non-small cell lung cancer (NSCLC)[107]. The notion of TMB as a predictor of clinical response to ICB has now been validated multiple times across multiple tumor types. However, this observed correlation between TMB and the improved response has yet to be fully substantiated, especially in a pan-cancer setting.

It is becoming increasingly evident that TMB alone is not a sufficient immune predictor of clinical response to immunotherapies such as ICB. There is a dynamic interaction between tumor cells, across the various stages of tumorigenesis, and the immune system. As such, the cancer-immune interaction is multifactorial and hence different combinations of "biomarkers" will be required. The *cancer immunogram* and *Immunoscore* are two recent concepts that have comprehensively summarized the main immune parameters that contribute positively or negatively to cancer development. The *immunogram* highlights parameters including tumor foreignness (i.e. TMB), T cell infiltration and the presence of inhibitory receptors, and importantly, stresses that the weight of each parameter may differ substantially between patients[111]. The *Immunoscore*, a recently defined immune-based assay, focuses on immune contexture, i.e. the density, composition, organization and functional state of the immune infiltrate in the TME[112]. Notably, this study demonstrates that a pre-existing adaptive immune response within the tumor is required for effective immunotherapies and that the pre-existing contexture of the TME ultimately dictates the therapeutic outcome.

In summary, the topics introduced have covered aspects of general T cell immunology with a primary focus on immuno-oncology and the role of antigen-specific $CD8^+$ T cells in checkpoint blockade therapy. The complex, multifactorial nature of the interactions between the immune system and cancer, and remarkably the dynamic state of T cells, provide some insight into why only a fraction of patients respond favorably to therapy. This also highlights that there is still a long road to fully understanding this complex interplay and that additional studies are required to characterize one of the primary therapeutic mediators of ICB, the tumor-reactive $CD8^+$ T cells.

# 3 RESEARCH OBJECTIVES

The overall objective of this thesis is to evaluate the properties of tumor-reactive T cells and novel tools for the detection of antigen-specificity, as well as to highlight nanoparticle-based strategies for delivery of therapeutic cargo, in the context of T cells and cancer therapy.

**Manuscript I**

*Characteristics of neoantigen-reactive CD8 T cells as an immune predictor for clinical outcome to checkpoint blockade therapy in a pan-cancer setting.*

The objective of this study is to assess whether the presence of neoantigen-reactive CD8 T cells (NARTs), their properties of antigen recognition as well as their phenotypic profile correspond with clinical outcome, to further the understanding of the role of NARTs in the response to ICB therapy.

**Additional results I**

*A method for generating off-the-shelf barcode-labeled MHC tetramer reagents for the interrogation of antigen-reactive T cells.*

This preliminary data highlights a method for generating barcode-labeled fluorescent streptavidin molecules as building blocks for the off-the-shelf generation of MHC tetramers for T cell staining. Proof of concept experiments are performed with known viral-derived epitopes to demonstrate that the co-attached DNA barcode can be used to identify the specificity of antigen-reactive T cells.

**Additional results II**

*Molecular encoding of mRNA nanocarriers for optimizing the delivery of therapeutic cargo.*

This includes preliminary data on the assessment of *in vitro* lipid nanoparticle (LNP)-based mRNA delivery in a tumor cell line and PBMCs. In an attempt to develop a proof of concept for a LNP screening platform, DNA barcodes are incorporated into the LNP assembly to provide an encoding system, to elucidate formulations that are successful in the delivery of mRNA to cells.

**Review article**

*Lipid nanoparticles for delivery of therapeutic RNA oligonucleotides.*

*DOI: 10.1021/acs.molpharmaceut.8b01290*

This review article published in ACS *Molecular Pharmaceutics* provides an updated summary of delivery methods for RNA gene therapeutics based on LNPs. In addition to surveying the recent preclinical and clinical data, this review provides an extensive overview of the appeal of RNA-LNPs and discusses the challenges associated with manufacture and screening for effective translation into drugs for human metabolic disease and cancer.

# 4 MANUSCRIPT I

## Characteristics of neoantigen-reactive CD8$^+$ T cells as an immune predictor for clinical outcome to checkpoint blockade therapy in a pan-cancer setting

Keith Henry Moss[1,4], Ulla Kring Hansen[1,4], Vinicius Araújo Barbosa de Lima[1,4], Esteban Sanchez Marquez[1], Annie Borch[1], Anne-Mette Bjerregaard[1], Olga Oestrup[3], Amalie Kai Bentzen[1], Andrea Marion Marquard[1], Inge Marie Svane[3], Ulrik Lassen[2], Sine Reker Hadrup[1,*]

[1] Department of Health Technology, Technical University of Denmark, Lyngby, Denmark.
[2] Department of Oncology, Phase 1 Unit, Rigshospitalet, Copenhagen, Denmark
[3] Center for Cancer Immune Therapy, Copenhagen University Hospital, Herlev, Denmark
[4] These authors contributed equally to this work

*** Correspondence:**
Corresponding Author
sirha@dtu.dk

## Abstract

Recent preclinical and clinical studies have highlighted the role of immune checkpoint inhibitor molecules in tumor-driven immune suppression. Immune checkpoint blockade (ICB) has been approved as first-line or second-line therapies for an ever-expanding list of malignancies. However, these forms of therapies are not effective for the majority of patients. There is an evident need to identify additional immune predictors for the clinical outcome to ICB, to enable broader and more efficient clinical utility of such immune-based therapies. Recent studies have shed light on how T cell-intrinsic factors, such as the functional state of tumor-reactive T cells, may dictate the outcome to ICB. In particular, T cells recognizing mutation-derived neoantigens are hypothesized to play a major role in tumor elimination. However, the dynamics and characteristics of such neoantigen-reactive T cells (NARTs) in the context of ICB are still limitedly understood. To explore this, tumor biopsies and peripheral blood were obtained pre- and post-treatment from 20 patients with solid metastatic tumors, in a Phase I basket trial. From whole-exome sequencing and RNA-seq data, patient-specific libraries of neopeptides were predicted and screened with DNA barcode-labeled MHC multimers for $CD8^+$ T cell reactivity, in conjunction with a T cell phenotype panel. We were able to detect NARTs in the peripheral blood and tumor biopsies for the majority of the patients; however, we did not observe any significant difference between the disease control and progressive disease patient groups, in terms of the breadth and magnitude of the detected NARTs. We applied dimensionality reduction and clustering techniques to provide an unbiased phenotypic analysis of bulk $CD8^+$ T cells and NARTs from the peripheral blood mononuclear cells (PBMCs) and tumor-infiltrating lymphocytes (TILs). There was no significant signature distinction between the disease control and progressive disease patients, related to the bulk $CD8^+$ T cell and NART phenotype pre- versus post-treatment. Although, there appeared to be a treatment-induced signature specifically in the NARTs post-treatment. This corresponded with the appearance of $Ki67^+$ $CD27^+$ $PD\text{-}1^+$ subsets in the PBMCs and $CD39^+$ $Ki67^+$ $TCF\text{-}1^+$ subsets in the TILs. Finally, differential gene expression analysis from the tumor microenvironment revealed that there is no signature related to the presence of NARTs, but there may be intrinsic properties of the tumor microenvironment that ultimately dictate the outcome to ICB. Our preliminary data indicate the possibility of monitoring the characteristics of NARTs from tumor biopsies and peripheral blood, and that such characteristics could potentially be incorporated with other immune predictors to understand further the complexity governing clinical success for ICB therapy.

## Introduction

Early preclinical studies have suggested evidence for the PD-1/PD-L1 axis in tumor-driven immune suppression and the activation of this signaling pathway has resulted in the evasion of antigen-specific T cell responses[1,2]. Phase I studies initially investigated monoclonal antibodies targeting PD-1 and PD-L1 in advanced solid tumors, which led to the development of the first checkpoint inhibitors, Nivolumab and Pembrolizumab, and approval by the FDA[1,2]. The initial approval of Pembrolizumab (α-PD-1) for advanced or unresectable melanoma set the scene for immunotherapy and moved it to center stage[3]. Accordingly, antibodies targeting the PD-1/PD-L1 pathway have been approved as first-line or second-line therapies for an ever-expanding list of malignancies, including lung cancers, renal cell carcinoma (RCC), lymphoma, head and neck squamous cells cancer (HNSCC), bladder cancer and gastro-esophageal cancer. However, these forms of therapies are not effective for the majority of patients receiving immune checkpoint blockade (ICB), despite major advancements in the field. As a result, there is an ever-growing interest to understand the key parameters that dictate the outcome of therapy, in the setting of ICB.

Among these parameters is the tumor mutational burden (TMB). TMB has been shown to predict clinical response to α-CTLA-4 therapy in patients with advanced melanoma[4], and additionally, for α-PD1 therapy in non-small cell lung cancer (NSCLC)[5]. Recently, it has been observed that, generally, patients with a higher TMB show better clinical responses to ICB[6]. Implying that patients with tumors harboring more mutations have a larger T cell repertoire for recognizing such mutations and that when checkpoint blockade therapy "removes the brakes of the immune system" there is a stronger antigen-specific T cell response against the tumor, in these cases. However, the recently proposed cancer *immunogram*[7] and *Immunoscore*[8] provide an extensive evaluation of the parameters that influence response to ICB. These comprehensive studies highlighted that certain immune predictors, such as TMB or the presence of inhibitory receptors, may provide prognostic value for some patients, but there is currently no universal predictor for all patients across different cancer types.

In this study, we use DNA barcode-labeled MHC multimers to detect neoantigen-reactive $CD8^+$ T cells (NARTs) in clinical samples from a Phase I basket trial. We monitor the dynamics of NARTs and their phenotypic properties along the course of ICB therapy in multiple cell compartments to investigate the hypothesis that the presence of NARTs, and their characteristics, can be used as an immune predictor for clinical outcome to ICB therapy in a pan-cancer setting.

## Results

### Neoantigen-reactive CD8$^+$ T cells are detectable in a diverse cohort of cancer patients

The present study consists of a cohort of 20 cancer patients diagnosed with nine different cancer types and treated with seven different ICB therapies, either as a mono or combination therapy. All patients were treated with ICB targeting the PD-1/PD-L1 axis. Clinical response to treatment was assessed according to the response evaluation criteria in solid tumors (RECIST) version 1.1, where the best-obtained response, lasting for at least 2 months, was reported. Based on this criteria, the patients were grouped into non-progressive disease (CR, PR, SD. n = 7), i.e. disease control, and progressive disease (PD. n = 13). Clinical information is presented in Supplementary Table S1.

The experimental workflow for the detection and phenotypic analysis of NARTs is schematically depicted in Figure 1A. Tumor biopsies and blood samples were collected before and after the first treatment with ICB. The mutational landscape was assessed by whole-exome sequencing (WES) to identify the tumor-specific mutations, and RNA-seq was performed to determine the relative expression levels of the mutated genes. This was proceeded by the *in silico* generation and filtration of neopeptides through the prediction tool, mutant peptide extractor and informer (MuPeXi)[9]. Patient-specific neopeptide libraries were then synthesized and assembled with DNA barcode-labeled pMHC multimers into patient-specific multimer panels. Included in each library were HLA-matching epitopes derived from common viruses; cytomegalovirus (CMV), Epstein-Barr virus (EBV) and influenza virus (FLU). Patient PBMCs and TILs (young and rapid expansion protocol (REP)) were obtained from the 20 patients pre- and post-therapy, and were then stained with the multimer panels in conjunction with a 12-parameter T cell phenotype panel. PBMCs from two healthy donors were additionally stained with each of the patient-specific multimer libraries, as controls. Patient samples and healthy donor controls were then acquired and sorted by FACS, multimer-binding CD8$^+$ T cells were isolated based on their positive PE signal, and the corresponding DNA barcodes were amplified with PCR and sent for next-generation sequencing to inform the identity of the T cell-reactive neoepitopes. DNA barcodes enriched in the sorted T cell fraction, with a false discovery rate (FDR) < 0.001, compared to baseline level defined significant T cell reactivity towards the corresponding neopeptide in the given sample.

Depicted in Figure 1B is a summary plot of the detected T cell reactivity for a representative patient (RH35). This plot is segregated vertically by the different PBMC and TIL samples, and horizontally by the HLA types included in the patient-specific panel. The $Log_2$ fold change (fc) depicts DNA barcodes that have been positively enriched in the given sample, and a threshold $Log_2$ (fc) value of > 2 depicts where significant T cell reactivity ($p < 0.001$) has been detected towards the neopeptide (red) or viral control peptide (blue). Several NARTs were detected in multiple of the patient's samples with four unique neoepitopes detected in at least one sample (Figure 1B).

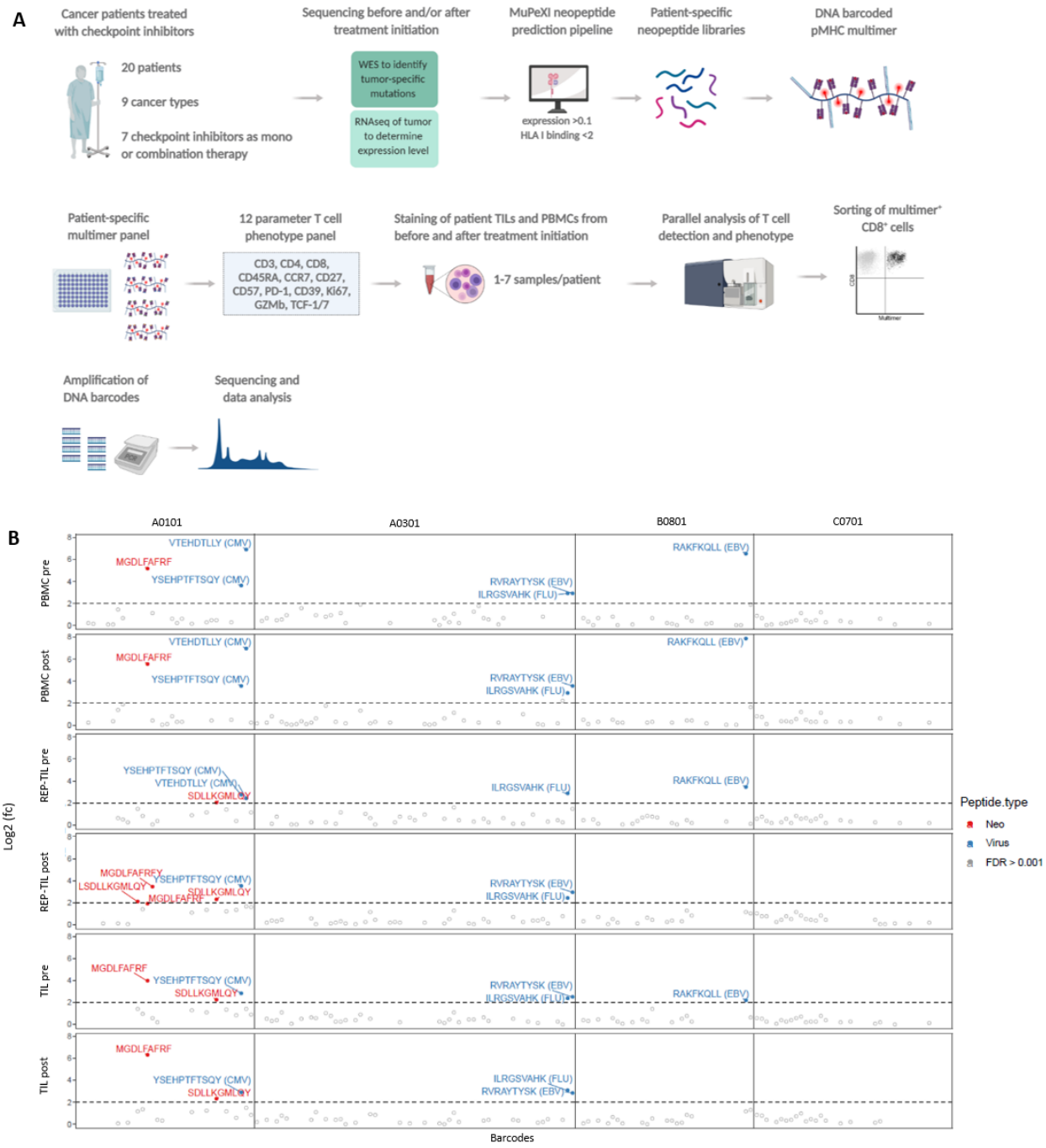


**Figure 1. Neoantigen-reactive CD8⁺ T cells are detectable in a diverse cohort of cancer patients**

**A,** Experimental workflow for the detection and phenotypic analysis of neoantigen-reactive T cells (NARTs).

**B,** Summary plot of the detected T cell reactivity for a representative patient (RH35). This plot is segregated vertically by the different PBMC and TIL samples, and horizontally by the HLA types included in the patient-specific panel. The Log2 fold change (fc) depicts DNA barcodes that have been positively enriched in the given sample, and a threshold Log2 (fc) value of > 2 depicts where significant T cell reactivity ($p < 0.001$) has been detected towards the neopeptide (red) or viral control peptide (blue).

The A0101-restricted neopeptide, MGDLFAFRF, appeared with significant T cell reactivity in both the PBMC and TIL samples, and an additional A0101-restricted neopeptide, SDLLKGMLQY, appeared in only the TIL and REP-TIL samples, albeit at a lower $Log_2$ (fc). Moreover, viral antigen-reactive T cells (VARTs) corresponding to CMV-, EBV- and FLU-derived epitopes were detected in several of the patient samples. Representative flow plots show the gating strategy applied for sorting NART and VART $CD8^+$ T cells from bulk PBMCs (Supplementary Figure S1A). It is important to note that neopeptide multimers are assembled on a PE-labeled dextran backbone, whereas virus multimers are assembled on an APC-labeled dextran. This allows separate analysis of these two classes of antigen-reactive T cells. Two additional patient representative summary plots for detected T cell reactivity are depicted in Supplementary Figure S1B and S1C. Again, several NARTs and VARTs were detected in multiple of the patient samples. For patient 25 (RH25), the B2705- restricted neopeptide, KRVFILLLS, appeared with significant T cell reactivity in the PBMC samples pre- and post-therapy. Note that this particular patient has an additional PBMC sample taken from day 86 post-treatment start, and the KRVFILLLS response was also detected there (S1B). For patient 27 (RH27), the A0201-restricted neopeptide, LLVFLVIYL, appeared with significant T cell reactivity in both PBMCs and TILs, pre- and post-therapy (S1C). Various healthy donor controls were screened multiple times across the patient screenings. A summary of all the detected VARTs across the healthy donor controls in multiple screenings is depicted as a correlation plot, both regarding $Log_2$ (fc) and estimated frequency (Supplementary Figure 1E and 1F).

**Characterization of the breadth and magnitude of NARTs between the two cell compartments**

To assess whether the detection of NARTs could potentially be used as an immune predictor for clinical outcome to ICB, the disease control and progressive disease patient groups were compared to evaluate for any tendencies that may be used to distinguish the groups. The total number of immunogenic neoepitopes across all of the patient screenings, for both PBMCs and TILs, is depicted in Figure 2A. This shows the absolute number of neoepitopes recognized by T cells, detected in each patient, split according to disease control and progressive disease patients. There is a slight tendency for an increased number of immunogenic neoepitopes detected in the patients responding to therapy.

To characterize the T cell reactivity pre- versus post-treatment in the two patient groups, the number of unique neoepitopes recognized, i.e. the breadth of the NARTs was assessed in either the PBMCs (Figure 2B) or the TILs (Figure 2C). In the PBMCs, there is no significant difference in the breadth of NARTs in the two patients groups, at each different time point. Interestingly, the breadth of NARTs seems to drop at day 34, especially in the treatment benefit group.

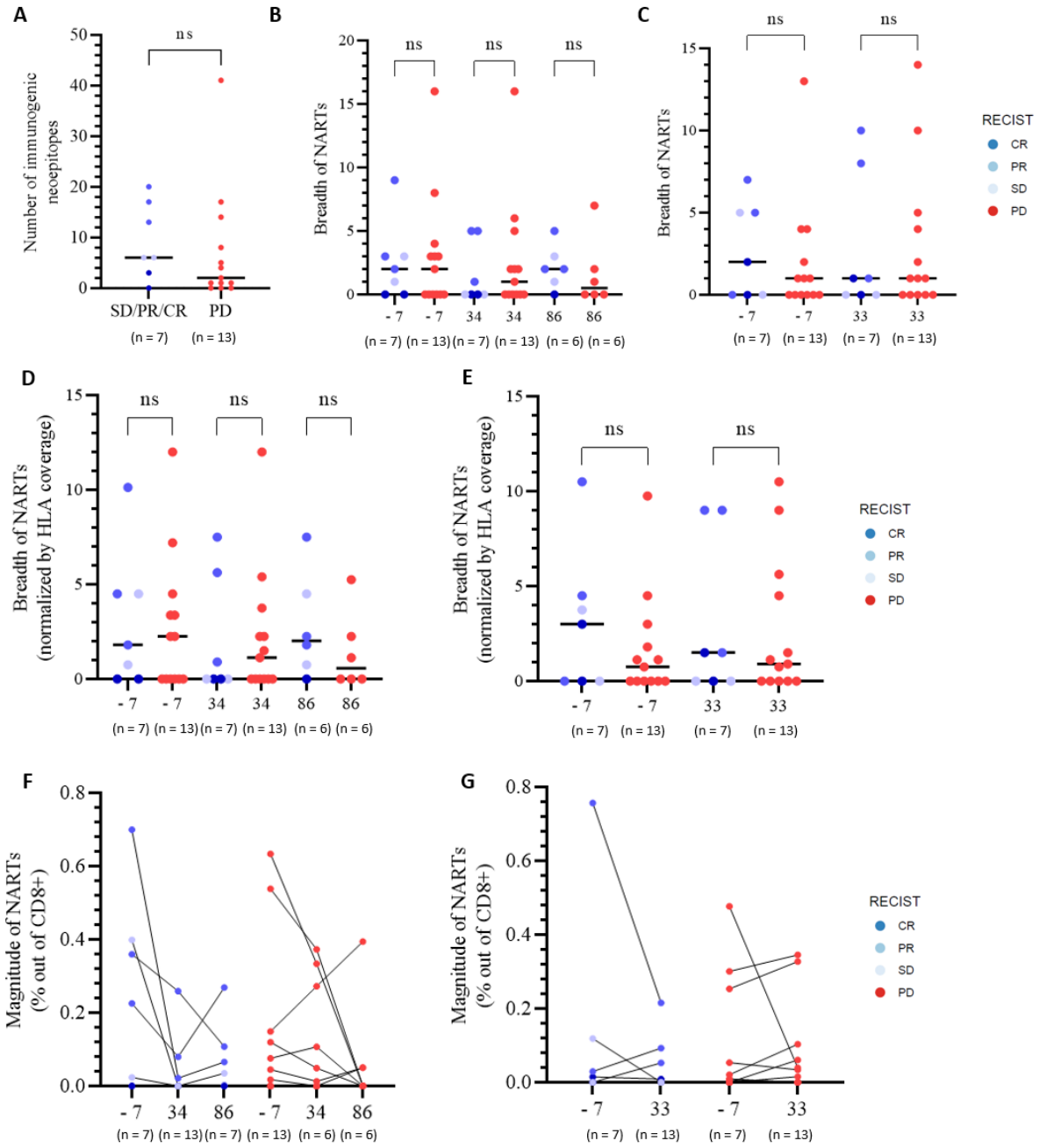


**Figure 2. Characterization of the breadth and magnitude of NARTs between the two cell compartments**

**A,** The total number of immunogenic neoepitopes across all of the patient screenings, for PBMCs and TILs combined. The patients are grouped and color-coded according to RECIST criteria, non-progressive (SD/PR/CR) and progressive disease (PD). Significance is denoted based on a Mann Whitney test. **B-C,** The breadth of NARTs, i.e. the number of unique neoepitope T cell recognition events, along the course of therapy, for PBMCs (B) and TILs (C). Pre-treatment (-7) and post-treatment (34 and 86, for PBMCs; 33 for TILs) **D-E,** The breadth of NARTs, normalized by average HLA coverage, along the course of therapy, for PBMCs (D) and TILs (E). **F-G**, The magnitude of NARTs along the course of therapy, represented by the sum of estimated frequency out of $CD8^+$ T cells for PBMCs (F) and TILs (G). Significance for B-E is denoted based on Kruskal-Wallis test with Dunn's correction. CR; Complete responder, PR; Partial responder, SD; Stable disease, PD; Progressive disease.

In the TILs, the breadth of NARTs tends to decrease post-treatment in the disease control group, albeit there is a substantial spread in the data points. In the progressive disease group, the breadth of NARTs tends to be stable pre- versus post-treatment.

Due to differences in the HLA coverage between the patients (Supplementary Figure S1D), the breadth of NARTs for each patient was normalized by the average HLA coverage. This difference in HLA coverage was due to constraints in the availability of HLA molecules in-house, and hence this normalization was performed to ensure a standardized representation of the patient-specific multimer panels. A similar trend was observed for the normalized breadth of NARTs, for both PBMCs (Figure 2D) and TILs (Figure 2E). The breadth of NARTs detected in the individual patients is summarized in Supplementary Table S2. Low-frequency NARTs were present in the healthy donor controls, but at lower detected levels than in the patient samples.

To assess the kinetics of the detected NARTs between the treatment time points, the sum of estimated frequencies (SEF) for the NARTs, out of $CD8^+$ T cells, i.e. magnitude of NARTs, was assessed for both the PBMCs (Figure 2F) and the TILs (Figure 2G). The estimated frequency is an approximation based on the fraction of read counts for a given neoepitope, obtained from sequencing, and the frequency of $multimer^+$ CD8 T cells in the sort gate. Hence, the SEF approximates the magnitude of the detected NARTs. Data points represent the SEF for the individual patients. In the PBMCs, for both patient groups, there is a tendency that the magnitude of the detected NARTs decreases at time point 34, followed by an increase at time point 86. In the TILs, mixed tendencies are observed, where the magnitude of NARTs for some patients increases post-therapy, and for others, decreases post-therapy.

Additional to monitoring the magnitude of the sum of detected NARTs, the magnitude of individual NARTs was surveyed between the PBMC and TIL compartment, pre- and post-treatment (Figure 2H). This analysis was performed to assess whether the most frequently detected NARTs in the PBMCs were also the most frequent in the TILs, and vice versa. This appears not to be the case; rather there is a somewhat random distribution of the magnitude of NARTs between the compartments. The compartmental overlap of the detected NARTs is given as a Venn diagram (Figure 2I). As depicted, there is an approximately equal breadth of NARTs in either the PBMCs or TILs. An overlap of 18% of the total unique NARTs was shared between the two compartments. To validate the detected NARTs, multiple neopeptides were selected for confirmatory tetramer stains (Figure 2J – 2L). The RH25-related neopeptide, KRVFILLLS, depicted in S1B, was confirmed in all three PBMC time points (Figure 2J). The RH27-related neopeptide, LLVFLVIYL, depicted in S1C, was confirmed in the REP-TIL and in both PBMC time points (Figure 2K). The RH35-related neopeptide, MGDLFAFRF, depicted in Figure 1B, was confirmed in both TIL and REP-TIL as well as both PBMC time points (Figure 2L).

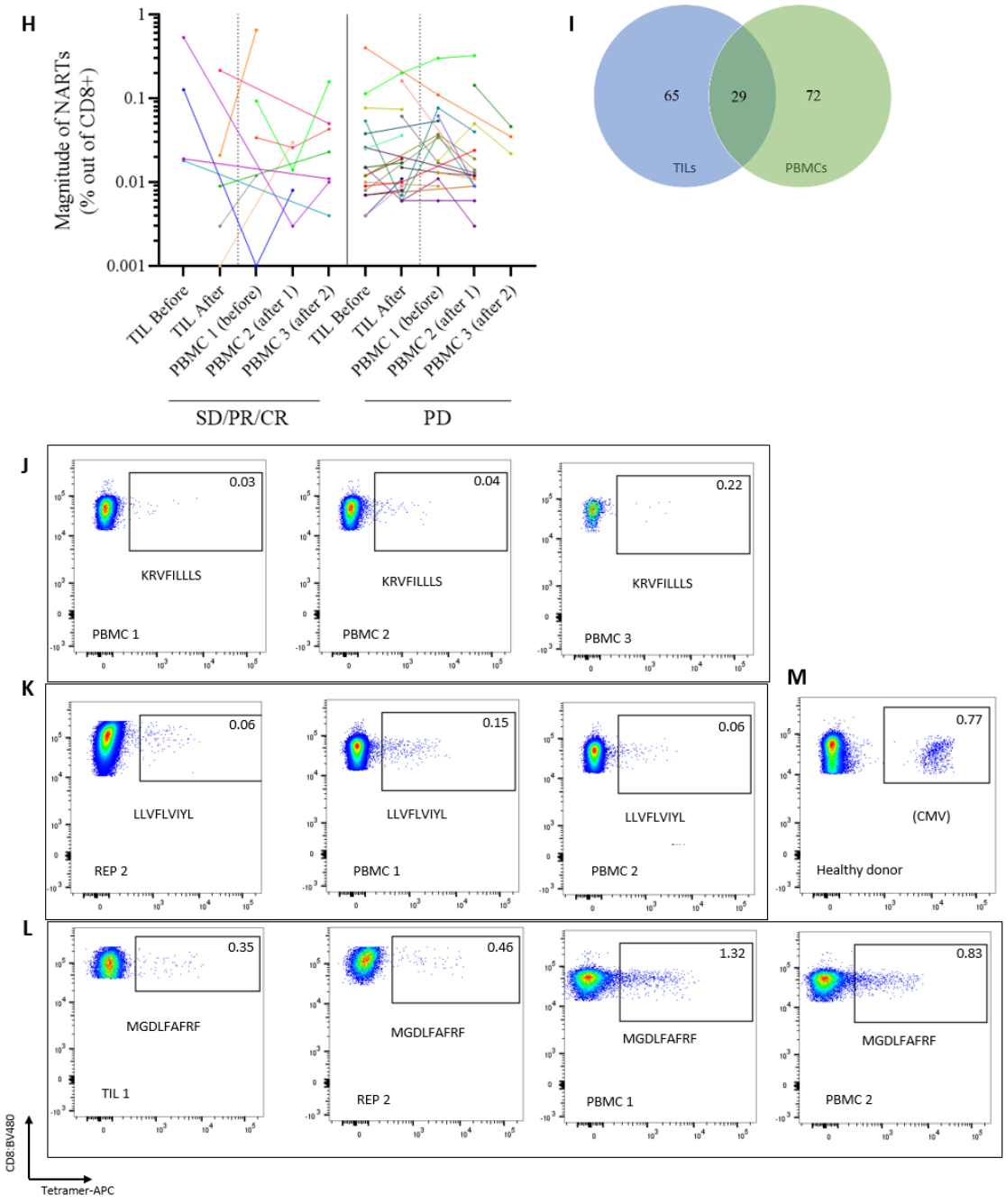


**Figure 2. Characterization of the breadth and magnitude of between the two cell compartments**

**H,** The magnitude of individual NARTs, represented by the estimated frequency out of CD8⁺ T cells, between the PBMC and TIL compartment, pre- and post-treatment. The detected NARTs have been given a random color-code and have been grouped based on RECIST criteria. The vertical dotted line visually segregates the TILs from PBMCs.
**I**, Venn diagram representing the compartmental overlap of the detected NARTs, where the number represents the breadth of unique NARTs in each compartment, as well as the NARTs that are shared between the compartments.
**J-L**, Confirmatory tetramer stains for representative patients RH25 (J), RH27 (K) and RH35 (L). The neopeptide, corresponding frequency of CD8⁺ T cells, and specific sample is denoted in the plots. **M**, Healthy donor control, with a known CMV CD8⁺ T cell response, was included in the same experiment. Pre-gated on lymphocytes, singlets, live, CD8⁺ and DUMP⁻. CR; Complete responder, PR; Partial responder, SD; Stable disease, PD; Progressive disease.

As a control for the tetramer assembly process, a healthy donor PBMC sample, with a known CMV response, was included in the experimental setup (Figure 2M).

When analyzing the bulk RNA-seq data from the TME, an estimate of T cell abundance was determined using the microenvironment cell populations (MCP) counter. (Supplementary Figure S2A). Here the patients are grouped according to RECIST criteria, and the T cell abundancy is compared pre- and post-treatment, where RNA-seq data was available. There was no apparent difference between the patient groups pre-treatment, but there is a tendency for an increased T cell abundance in the disease control group post-treatment. Moreover, the T cell receptor (TCR) CDR3 sequences were extracted from available bulk RNA-seq data from the TME, either pre- or post-treatment, and the T cell diversity was calculated. The T cell diversity was then correlated with the breadth of NARTs, for all of the patients (Supplementary Figure S2B). A slight positive correlation ($r = 0.23$) was observed between the two parameters, in particular, with those patients presenting an increased breadth of detected NARTs.

**Phenotypic characterization of bulk CD8$^+$ T cells and NARTs from patient-derived PBMCs**

Since the distinction between the disease control and progressive disease patient groups has not been evident based on the characteristics of breadth and magnitude of the detected NARTs, additional characteristics were assessed. Concordant with recent literature and clinical observations, it is becoming evident that the functional state of tumor-reactive T cells, e.g. NARTs, ultimately dictates the therapeutic outcome to ICB. For this, a 12-parameter T cell phenotype antibody panel was incorporated into the MHC multimer screening pipeline to allow the parallel analysis of T cell detection with corresponding phenotypic profiling.

As an initial attempt at the phenotypic profiling related to T cell functional state, e.g. activation, proliferation or exhaustion etc., bulk CD8$^+$ T cells and NARTs from the patients were compared to assess for any phenotypic signatures that could be associated with NARTs, without any patient grouping. It is important to note that, due to sample limitation, the phenotypic analysis was only performed on the second half of the patient cohort (10 patients, RH22 – RH35). Initially, the samples were evaluated for single-parameter phenotypic differences, which additionally served to assess the quality of the data (Supplementary Figure S3). Apart from a significant increase ($p < 0.05$) in TCF-1 expression post-treatment in the bulk CD8$^+$ T cells from PBMCs (Figure S3B), there appeared to be no significant treatment-induced changes for the rest of the selected markers (Figure S3B and S3C). To comprehensively evaluate T cell characteristics, a multiparametric analysis is required. To this end, the dimensionality reduction technique, UMAP, in combination with unsupervised clustering by FlowSOM, was applied to the dataset. This was performed based on exploring T cell subpopulations that may have been missed due to conventional plotting and manual gating.

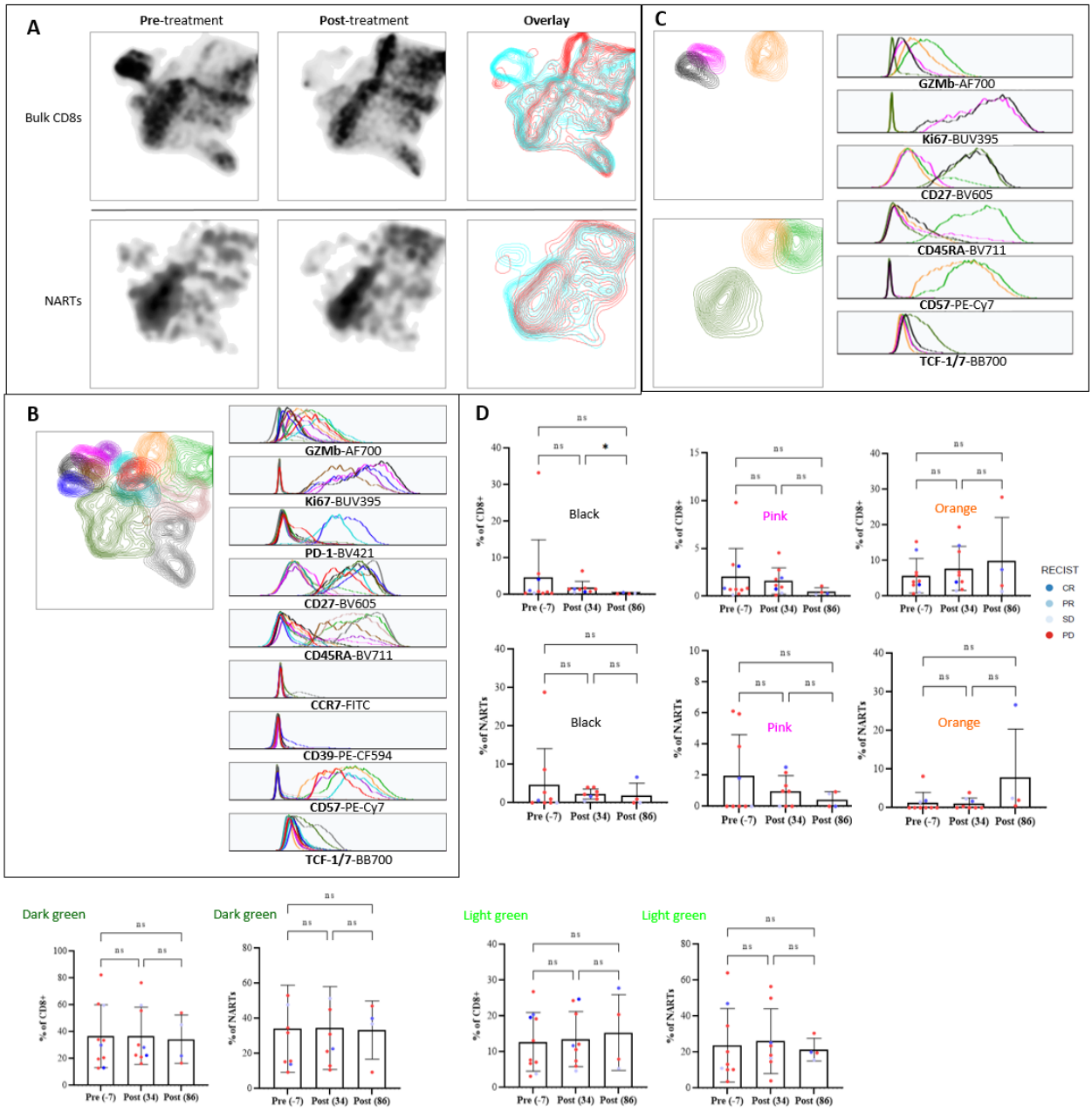


**Figure 3. Phenotypic characterization of bulk CD8⁺ T cells and NARTs from patient-derived PBMCs**

**A,** UMAP representation of the global structure of bulk CD8⁺ T cells (top) and NARTs (bottom) from all patients, pre- and post-treatment depicted as density and overlay plots (light blue: pre-treatment, red: post-treatment).

**B,** Overlay of FlowSOM clustering on UMAP, with conjunct histograms to visualize and identify the sub-populations within the global structure.

**C,** Selected sub-populations from the FlowSOM clustering and histograms for the corresponding phenotypic profiles.

**D,** Quantitative assessment of the FlowSOM clustering for the selected sub-populations, depicting the frequency of CD8+ T cells or NARTs that the particular sub-populations represent. For all the plots related to frequency of bulk CD8+ T cells: (-7, n = 10; 34, n = 9; 86, n = 4) and for all plots related to frequency of NARTs: (-7, n = 9; 34, n = 8; 86, n = 4). Significance for D is denoted based on Kruskal-Wallis test with Dunn's correction

The global structure of the bulk $CD8^+$ T cells and NARTs, from all patient PBMCs, without grouping, is depicted as density plots in Figure 3A. Here it is possible to visualize and compare the regions (subpopulations) of the global structure between bulk $CD8^+$ T cells and NARTs, both pre- and post-treatment. Overlays of pre-treatment (light blue) versus post-treatment (red) are given alongside the density plots, for both bulk $CD8^+$ T cells and NARTs. Visual distinctions may be appreciated from the density plots and overlay plots (Figure 3A). However, since the UMAP technique only provides a visualization of the subpopulations within the global structure, it is not possible to inform on the corresponding identity or phenotypic profile of the subpopulations. To this end, FlowSOM clustering was subsequently overlaid on the UMAP to generate a profile for the various subpopulations. A representative FlowSOM overlay and conjunct histograms for the phenotypic markers, for bulk $CD8^+$ T cells, are depicted in Figure 3B. Keeping this in mind, a selected few subpopulations were focused on to assess if there was any phenotypic signature induced with treatment, and secondly, whether a distinct signature was associated with NARTs versus bulk $CD8^+$ T cells (Figure 3C). When looking at the density plots and overlay for bulk $CD8^+$ T cells, with reference to the selected subpopulations (Figure 3C), it was apparent that the black and pink subpopulations seemed to reduce post-treatment, whereas the orange one seemed to increase. This corresponded with the following phenotypic profiles: black ($Ki67^{hi}$, $CD27^{hi}$, $GZMb^{int}$), pink ($Ki67^{hi}$, $CD27^{low}$, $GZMb^{int}$) and orange ($CD57^{hi}$, $GZMb^{int}$). Similarly, when looking at the NARTs specifically, it is apparent that the orange, light green and dark green subpopulations seemed to increase post-therapy. This corresponded with light green ($CD57^{hi}$, $CD45RA^{hi}$, $GZMb^{hi}$) and dark green ($CD27^{hi}$, $TCF\text{-}1^{int}$).

These histograms, however, provide only a qualitative assessment of the selected subpopulations. To allow for quantitation and statistical analysis, the FlowSOM clustering was run on an individual patient basis and the data was plotted in Figure 3D. Here, the patients are not grouped according to clinical outcome, but a color code is given to provide some further description. Keeping the same format, these plots depict the frequency of the particular subpopulation out of $CD8^+$ T cells or NARTs, respectively. The color label for the respective subpopulation has been indicated on the plots, for ease of understanding. The plotting of the selected subpopulations does not seem to reveal any significant treatment-induced phenotypic signature or any profile difference related to either the bulk $CD8^+$ T cells or NARTs (Figure 3D). However, the observations from the density and overlay plots are confirmed. It is also quite apparent that a few outlying patients seem to have a predominant contribution to the signal observed in the density and overlay plots in Figure 3A.

Since there appeared to be no obvious treatment-induced phenotypic distinction between the bulk $CD8^+$ T cells and NARTs from the PBMCs, without the use of patient grouping, a similar analytical workflow was performed on the dataset, this time with a grouping of the patients into disease control and progressive disease. The global structure of the bulk $CD8^+$ T cells and NARTs, pre- and post-treatment, from all patient PBMCs, is depicted as UMAP density plots (Figure 3E). This is the same UMAP as Figure 3A, however, now the patient groups have been segregated visually in the UMAP to allow for more subtle distinctions.

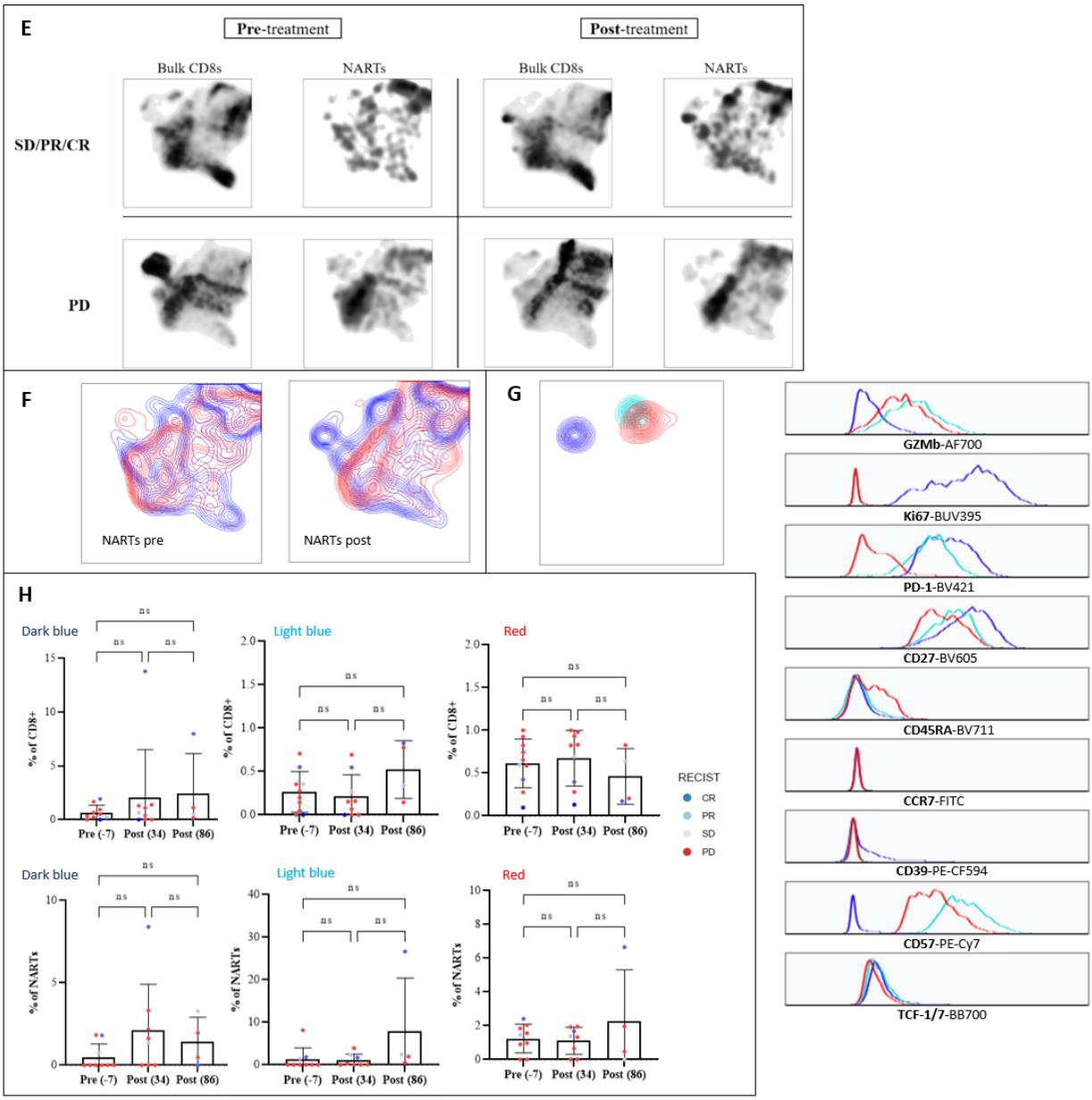


**Figure 3. Phenotypic characterization of bulk CD8⁺ T cells and NARTs from patient-derived PBMCs**

**E,** UMAP representation of the global structure of bulk CD8⁺ T cells and NARTs for responding (top) and non-responding (bottom) patients, pre- and post-treatment, depicted as density plots.

**F,** UMAP overlay of responding patient NARTs (blue) and non-responding patient NARTs (red), pre-treatment (left) and post-treatment (right).

**G,** Selected NART sub-populations from the FlowSOM clustering and histograms for the corresponding phenotypic profiles.

**H,** Quantitative assessment of the FlowSOM clustering for the selected sub-populations, depicting the frequency of CD8⁺ T cells or NARTs that the particular sub-populations represent. For all the plots related to frequency of bulk CD8⁺ T cells: (-7, n = 10; 34, n = 9; 86, n = 4) and for all plots related to frequency of NARTs: (-7, n = 9; 34, n = 8; 86, n = 4). CR; Complete responder, PR; Partial responder, SD; Stable disease, PD; Progressive disease. Significance for H is denoted based on Kruskal-Wallis test with Dunn's correction.

When focusing specifically on the density plots of the NARTs, there are apparent changes in the global structure post-treatment, particularly in the case of the disease control patients (Figure 3E). The progressive disease patients do not seem to have as distinctive changes in global structure post-treatment. Another way of easing the visualization of the changes between the groups, pre- to post-treatment, is with the use of overlay plots (Figure 3F). In this case, however, the NARTs pre-treatment, for the disease control (blue) and progressive disease group (red) have been overlaid in the plot to the left. Similarly, in the plot to the right, the NARTs post-treatment have been overlaid for the disease control (blue) and progressive disease group (red). The visual distinction from pre- to post-treatment can now be more easily appreciated, with reference to the subpopulations that become more prominent post-treatment in the disease control group. In a similar manner to Figure 3B and 3C, FlowSOM clustering was overlaid on the UMAP and relevant subpopulations were focused on for phenotypic profiling (Figure 3G). The three subpopulations of interest, that were prominent post-treatment in the NARTs from the disease control group, corresponded with the following profiles: dark blue (Ki67$^{hi}$, PD-1$^{hi}$, CD27$^{hi}$), light blue (PD-1$^{hi}$, CD27$^{hi}$, CD57$^{hi}$, GZMb$^{hi}$) and red (PD-1$^{low}$, CD27$^{int}$, CD45RA$^{int}$, CD57$^{int}$, GZMb$^{hi}$).

The three FlowSOM subpopulations focused on in Figure 3G were then similarly quantified on an individual patient basis (Figure 3H). Although the UMAP was segregated by patient group for visualization purposes, the plotting was still performed without patient grouping due to the low number of patients in the disease control group (for bulk CD8$^+$ T cells, n = 3; for NARTs, n = 2). There were only two patients in the disease control group for the NART phenotype analysis since one of the patients did not show any NART detection in the screening. However, the patients are still given a color code based on RECIST criteria, for descriptive purposes. The plotting of the three subpopulations in Figure 3H reveals a similar tendency for bulk CD8$^+$ T cells and NARTs. The dark blue subpopulation referred to in Figure 3G as the Ki67$^{hi}$ subset, seems to be increasing post-therapy in both the bulk CD8$^+$ T cells and NARTs. An outlying partial responder patient (RH25) is very apparent among this dark blue subset and has likely been the primary contributor to the signal observed in the density and overlay plots. The light blue and red subpopulations referred to in Figure 3G as the CD57$^{hi}$/GZMb$^{hi}$ subsets, also tend to increase post-treatment (Figure 3H). Again, the partial responder (RH25) appears to be an outlier.

This entire workflow, from UMAP visualization to FlowSOM clustering and quantitation, was performed in a separate analysis for the patient TILs (Supplementary Figure S3 E-H). Due to the separate UMAP run, the global structure appears visually different and the colors of the FlowSOM subpopulations are not the same, with respect to Figure 3A – 3H, however, the principles are the same. In brief, there appear to be two subpopulations (red and beige) that increase specifically in the NARTs, post-treatment. These subpopulations corresponded with the following phenotypic profiles: red (Ki67$^{hi}$, CD27$^{int}$, CD39$^{hi}$, TCF-1$^{int}$) and beige (Ki67$^{int}$, CD27$^{int}$, CD39$^{hi}$, TCF-1$^{int}$) (Supplementary Figure S3 G-H). It should be noted that all TIL samples were derived from expanded TILs and hence the phenotypic characteristics are likely to be altered during the *in vitro* culturing, compared to the *in vivo* scenario.

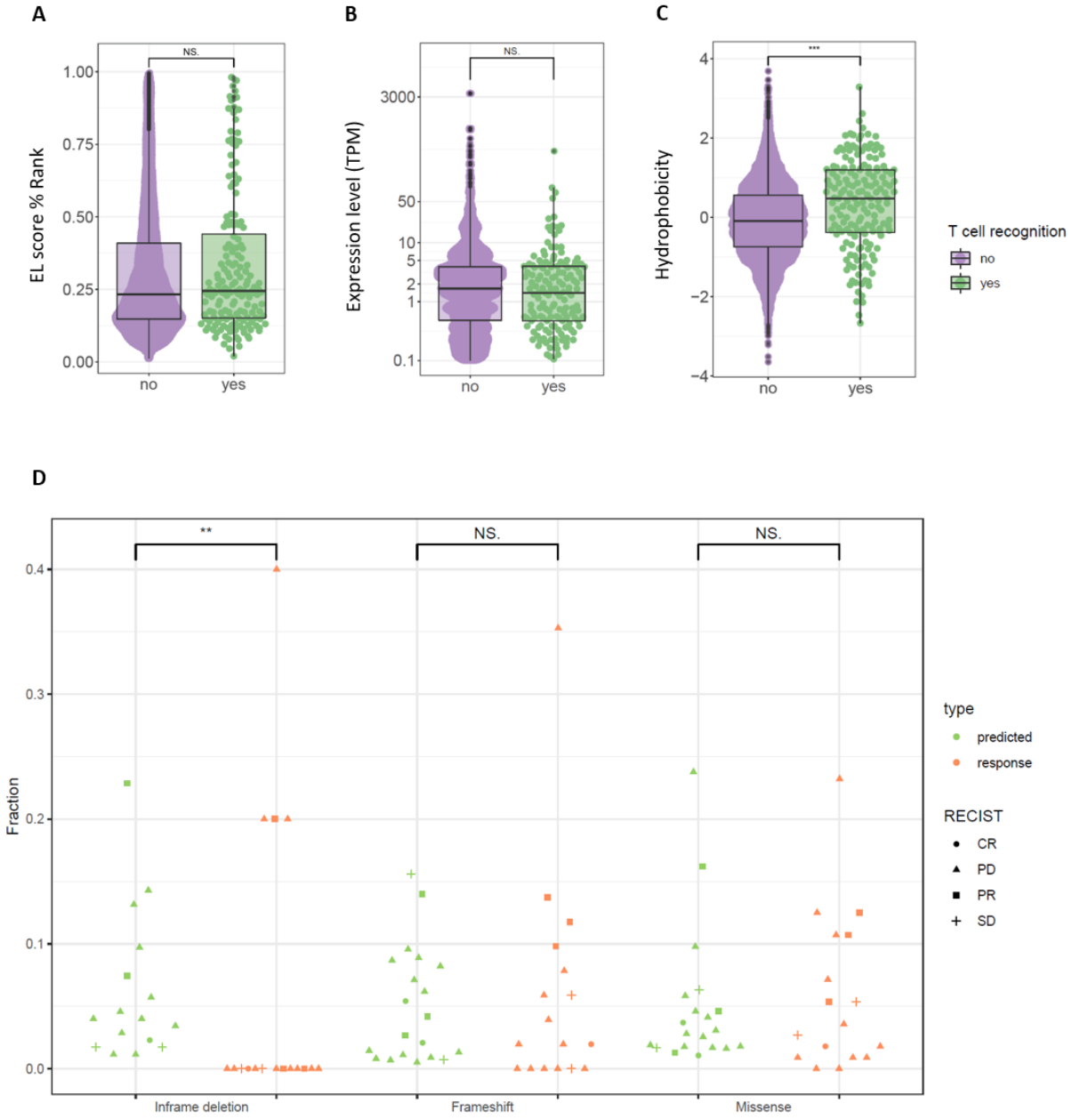


**Figure 4. Characteristics of neoepitope immunogenicity**

**A,** Comparison of immunogenic and non-immunogenic neopeptides in terms of predicted MHC binding affinity, represented as eluted ligand rank score (EL score % Rank) using netMHCpan 4.0. **B**, Comparison of immunogenic and non-immunogenic neopeptides in terms of expression level in transcripts per million (TPM) of the genes encoding for the neopeptides. **C**, Comparison of immunogenic and non-immunogenic neopeptides in terms of neopeptide hydrophobicity. **D,** The mutation types of the predicted neopeptides (green) and immunogenic neoepitopes (orange) calculated as a fraction out of total predicted or immunogenic peptides in a given patient. Significance denoted based on a Mann-Whitney test. CR; Complete responder, PR; Partial responder, SD; Stable disease, PD; Progressive disease.

**Characteristics of neoepitope immunogenicity**

To characterize additional aspects related to $CD8^+$ T cell recognition of neoepitopes, in particular, the properties of neoepitopes that give rise to T cell reactivity, three parameters, that were included in the neoepitope prediction, were assessed. The three parameters, eluted ligand (EL) rank score, expression level and hydrophobicity were assessed across all patients to explore these characteristics in relation to neoepitope immunogenicity. When comparing the EL rank score for neopeptides, a score of 0.25 – 0.5 was observed for most neopeptides, which is the range defining a weak MHC binder (Figure 4A). Additionally, it appears that those neopeptides associated with T cell recognition do not show a higher predicted binding affinity, within this narrow range evaluated. When comparing the expression levels of the genes encoding the neoepitopes, it appears that an increased gene expression level is not associated with T cell recognition (Figure 4B), though this has been indicated from previous studies (manuscript in revision). The third parameter, neopeptide hydrophobicity, does however show a significant difference ($p = 2x10^{-7}$) for those neopeptides where T cell recognition is associated (Figure 4C).

The association between the mutation types (in-frame deletion, frameshift and missense) of the recognized neoepitopes between the different patients (Figure 4D) was then investigated. The fraction of predicted neopeptides for each mutation type was also included in the analysis. In general, the fraction of mutations resulting in T cell recognition was highest for neoepitopes deriving from frameshift and missense mutations. There appears to be no enrichment of any particular mutation type in either the disease control or the progressive disease patients.

**Tumor mutational burden and predicted number of neopeptides**

The number of non-synonymous mutations and predicted neopeptides have been shown to indicate outcome of ICB in homogenous cancer cohorts. This was then investigated to see whether a similar trend is observed in a heterogeneous cohort such as this. For the majority of patients, both parameters were determined before and after the first treatment. No apparent difference in the numbers of non-synonymous mutations was observed between the patient groups, either pre- or post-treatment (Supplementary Figure S4A). The same comparison was performed with the number of predicted neopeptides. The non-progressive disease group showed a tendency for a higher number of predicted neopeptides at baseline and showed a similar tendency after the first treatment (Supplementary Figure S4B). When assessing the overlap between non-synonymous mutations and predicted neoepitopes at the two time points, it appeared that the non-progressive disease group had a more substantial overlap in both non-synonymous mutations and predicted neoepitopes between the two time points (Supplementary Figure S4C). Whereas, the PD group had less overlap between the time points for both parameters (Supplementary Figure S4D).

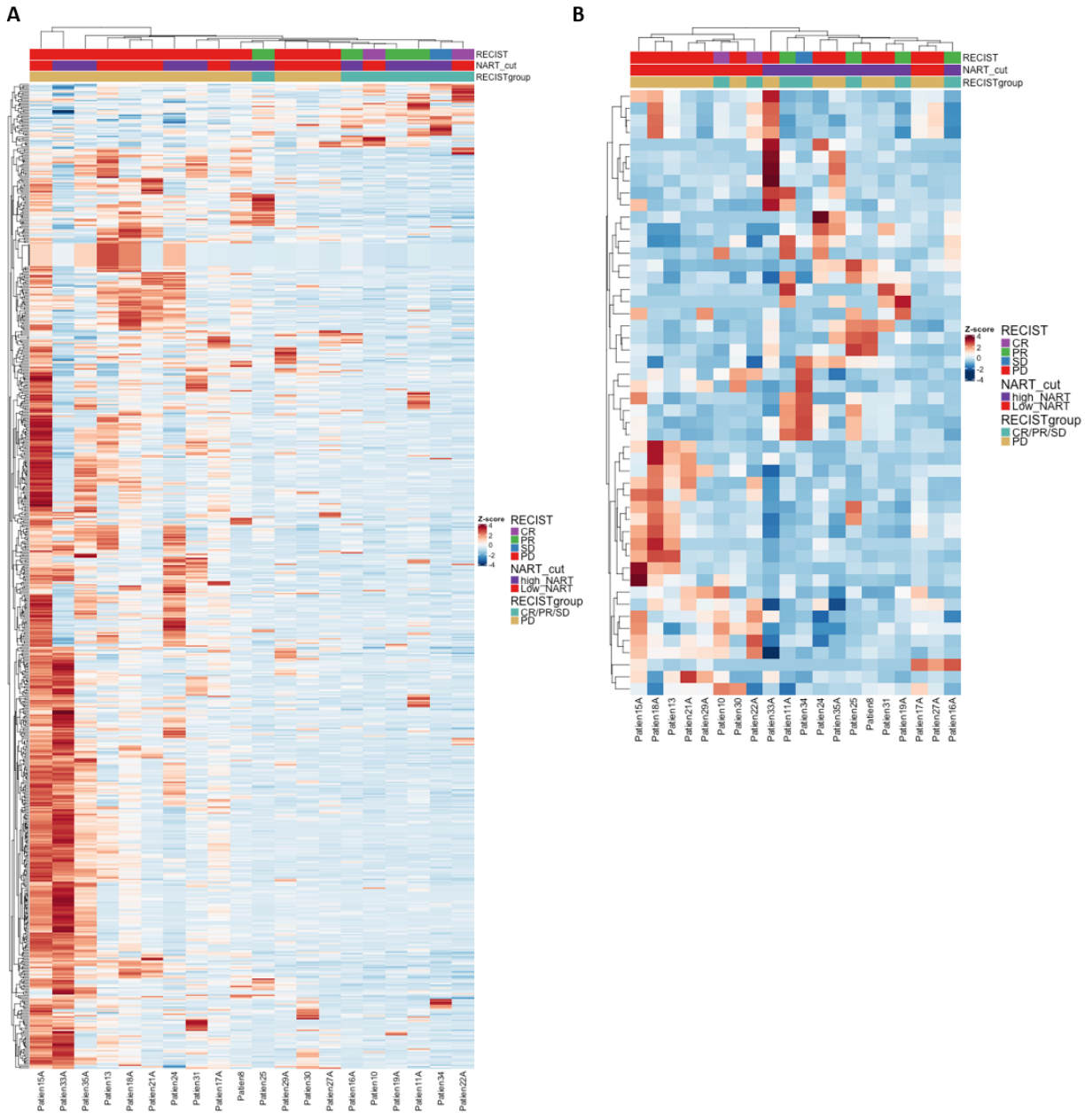


**Figure 5. Gene expression analysis from the tumor microenvironment reveals a signature related to treatment outcome**

**A,** Differential gene expression analysis based on RNA-seq data from the tumor microenvironment pre-treatment, segregated vertically by RECIST group i.e. treatment outcome. **B**, Differential gene expression analysis based on RNA-seq data from the tumor microenvironment pre-treatment, segregated vertically by the breadth of detected NARTs (i.e. NART high or NART low, threshold set by the median value). CR; Complete responder, PR; Partial responder, SD; Stable disease, PD; Progressive disease.

**Gene expression analysis from the tumor microenvironment reveals a signature related to treatment outcome**

Finally, a differential gene expression analysis was performed on the RNA-seq data from the TME, where all the differentially expressed genes were presented in a heat map and segregation was made either according to treatment outcome (Figure 5A) or according to the breadth of detected NARTs (Figure 5B). When looking at the differentially expressed genes split by treatment outcome, it is apparent that there is a polarization of certain gene clusters, i.e. a signature, related to either the disease control or the progressive disease groups, respectively (Figure 5A). When looking at the differentially expressed genes split by the presence of either a high or a low breadth of NARTs, no apparent signature is observed.

## Discussion

We report herein, a comprehensive evaluation of the characteristics of neoantigen-reactive $CD8^+$ T cells, to explore additional immune predictors of clinical outcome to ICB therapy. The concepts such as the cancer *immunogram*[7] and *Immunoscore*[8] have highlighted that although certain immune predictors, such as TMB or the presence of inhibitory receptors, provide prognostic value in some patients, there is currently no universal immune predictor for all patients of different cancer types. Hence, a pan-cancer study such as this is highly relevant. Furthermore, basket trial approaches, where patients are selected for treatment based on their molecular characteristics (e.g. TMB) rather than their diagnosis, are becoming more prominent in the clinic. Thus, understanding how immune characteristics may affect treatment outcomes in such a diverse cohort is of increasing importance.

The experimental workflow utilized in this study for the screening of antigen-reactive T cells makes use of dextran backbones with different fluorescent labels allowing the simultaneous detection and analysis of both NARTs and VARTs. This unique aspect could be used to characterize further T cell recognition in the context of chronic viral infection and cancer. The strong correlation for the detection of VARTs in healthy donor controls across all of the patient screenings highlights the robustness and reproducibility of the utilized screening approach.

We initially set out to evaluate whether the characteristics, such as breadth and magnitude of detected NARTs, were able to provide a distinction between the disease control and progressive disease patients. There was no significant difference in the absolute number of detected immunogenic neoepitopes between the patient groups, apart from a minor tendency for an increase in the disease control group. In the PBMCs, the breadth of the detected NARTs tended to decrease initially post-treatment, followed by an increase at the later time point, in the disease control group. This seems to confound previous reports showing an early increase in detected NARTs post ICB treatment, e.g. in the case of a bladder cancer study (manuscript in revision). In the progressive disease group, the breadth of detected NARTs tended to decrease and did not show a similar increase at the later time point. There appeared to be no clear tendencies for the breadth of the NARTs from the TILs. Although, recent studies have highlighted that PD-1 axis blockade does not necessarily increase the breadth of the NARTs in the TME[11]. Concerning the detection of

NARTs, the normalization by HLA coverage ensures a standardized representation of the patient-specific multimer panels. Those patients with greater HLA coverage would be more likely to result in the detection of NARTs, simply because more neopeptides could be accommodated in the screening. An alternative could be to normalize by the neopeptide library size, but this would potentially eliminate information on those particular patients that are present with high tumor mutational burden, e.g. $MSI^{hi}$ tumors[12], and are thus more likely to generate neoantigens and corresponding T cell reactivity.

We next evaluated the magnitude of the NARTs in the PBMCs and TILs, from pre- to post-treatment, to assess for treatment-induced kinetics. There was no significant difference between the groups; however, in a similar fashion to the breadth, there was a tendency that the magnitude of the detected NARTs decreased initially post-treatment followed by an increase at the later time point, at least in the disease control group. This would support a previous finding, where a higher frequency of neoantigen-specific T cells was detected in NSCLC patients responding to anti-PD-L1 therapy[13]. However, there have been potential implications reported about PD-1 blockade providing therapeutic benefit not by increasing T cell infiltration, but rather by reducing the generation of anergic tumor-reactive T cell populations within the TME[11]. In the TILs, again, no clear tendencies were observed. Strikingly, only 18% of the NARTs were detected in both TILs and PBMCs in our study. However, this is consistent with previous findings in an ovarian cancer cohort, whereby a discordance of neoepitope recognition was observed between TILs and PBMCs[14]. This could very likely be due to technicalities such as detection thresholds, as NARTs in circulation could be of lower frequency. This would suggest a dynamic relationship between the neoantigen landscape and repertoire of NARTs along the course of therapy, with the emergence and/or disappearance of clonal and subclonal neoantigens in the tumor and peripheral blood. The confirmation of the selected patient-related neopeptides with tetramer stains further verifies the presence of these NARTs in the given patients. Although, a more comprehensive validation by alternative techniques would ideally be performed in future studies related to this patient cohort. A larger selection of detected neopeptides could be included for combinatorial tetramer staining or *in vitro* stimulation assays. Additionally, *in vitro* culturing to provide specific expansion of NARTs, to numbers sufficient for further functional studies, such as T cell killing assays with patient-derived tumor cell lines, could be applied. Although immunogenic neoepitopes have been detected in this study, the aspects related to functional T cell recognition are still lacking.

According to the bulk RNA-seq data from the TME, the tendency for increased T cell abundancy in the disease control group post-treatment could indicate that increased T cell infiltration in the TME resulted in improved treatment prognosis. Patients with higher T cell influx in the TME generally respond more favorably to ICB[16]. Additionally, the minor positive correlation between T cell diversity and the breadth of NARTs, especially for those patients with a larger breadth of NARTs, indicates that the diversity of the TCR repertoire could be informative for the capacity to detect a larger range of neoantigens, which would also, in theory, be favorable for outcome. A positive correlation between T cell diversity and neoantigen burden has been recently reported in a pan-cancer immunogenomic analysis on data for 20 different solid cancers[17]. A low T cell

diversity would indicate a low level of T cell infiltration into the TME, and ultimately a decreased number of detected NARTs. However, a fraction of the progressive disease patients had a high T cell diversity, which did not reflect NARTs. These could be representative of bystander T cells in the TME.

The distinction between the disease control and progressive disease patient groups has yet to be evident based on the characteristics of breadth and magnitude of the detected NARTs. Considering the reports that the functional state of tumor-reactive T cells may ultimately dictate the therapeutic outcome to ICB[18], a 12-parameter T cell phenotype antibody panel was incorporated into the MHC multimer screening pipeline to provide a phenotypic profile of the detected NARTs. The dimensionality reduction technique, UMAP, and FlowSOM clustering were applied to the dataset to assess for any phenotypic signature induced with treatment, and secondly, to evaluate whether a distinct signature was associated with NARTs versus bulk $CD8^+$ T cells. This unbiased analysis was done to explore T cell subpopulations that may have been missed due to conventional plotting and manual gating. Additionally, the unsupervised nature of this approach removes any potential bias introduced from manual gating. In the PBMC compartment, a treatment-induced signature was observed for both bulk $CD8^+$ T cells and NARTs. Post-treatment, the bulk $CD8^+$ T cells seemed to lose two proliferating subsets, of which, one was in an early-differentiated state and the other a late-differentiated state i.e. black ($Ki67^{hi}$, $CD27^{hi}$) and pink ($Ki67^{hi}$, $CD27^{low}$). A late-differentiated effector subset, i.e. orange ($CD57^{hi}$, $GZMb^{int}$), became more prominent. Since these are frequencies, however, this may be due to the loss of other subsets. Two additional subsets were highlighted, which became more prominent in the NARTs. A late-differentiated $T_{EMRA}$ subset i.e. light green ($CD57^{hi}$, $CD45RA^{hi}$, $GZMb^{hi}$) and an early-differentiated subset i.e. dark green ($CD27^{hi}$, $TCF\text{-}1^{int}$) appeared to be more prominent post-treatment. Again, since these subsets appear not to be proliferating ($Ki67^{neg}$), this could be due to the disappearance of other subsets. However, $T_{EMRA}$s in the blood have been shown to increase in frequency in the context of prolonged viral infection, but also with age[19,20]. At least from an initial perspective, there appeared to be no specific signature that could distinguish the NARTs from bulk $CD8^+$ T cells.

Upon further UMAP visualization, this time with segregation based on patient grouping, three additional subsets became apparent post-treatment, specifically in the disease control patient NARTs. One proliferating, early-differentiated subset i.e. dark blue ($Ki67^{hi}$, $PD\text{-}1^{hi}$, $CD27^{hi}$) and two non-proliferating, early/late differentiated subsets i.e. light blue ($PD\text{-}1^{hi}$, $CD27^{hi}$, $CD57^{hi}$, $GZMb^{hi}$) and red ($PD\text{-}1^{low}$, $CD27^{int}$, $CD45RA^{int}$, $CD57^{int}$, $GZMb^{hi}$) became more apparent post-treatment. The light blue subset could potentially be terminally differentiated effectors that are becoming dysfunctional. The high expression of GZMb could be an indication of dysfunctionality as opposed to effector function, as insufficient degranulation may prevent the release of GZMb. Whereas, the red subset appears to have low PD-1 expression and has re-gained CD45RA expression, indicating a potential $T_{EMRA}$ subset. However, caution must be taken when basing conclusions on PD-1 expression, considering many of the patients in this analysis have been treated with PD-1 blockade antibodies. On the other hand, it has been reported that PD-1 expressing tumor-reactive T cells have contributed to favorable treatment outcome in ICB[21]. This may seem obvious since PD-1 blockade would prevent the suppression of such $PD\text{-}1^+$ T cells. An interesting

observation from the quantitation of FlowSOM subpopulations by individual patients was that an outlying partial responder patient (RH25, in light blue) was the primary contributor to these apparent increases post-treatment. Since this is a disease control patient, it does however hint at a favorable signature of NARTs for promoting therapeutic outcome. The signature, in this case, would be the presence of proliferating, early differentiated and PD-$1^{+}$ subsets.

In the TILs, two $CD39^{+}$ subpopulations became more apparent post-treatment, specifically in the NARTs. One proliferating subset, i.e. red ($Ki67^{hi}$, $CD27^{int}$, $CD39^{hi}$, TCF-$1^{int}$) and another low-proliferating subset, i.e. beige ($Ki67^{int}$, $CD27^{int}$, $CD39^{hi}$, TCF-$1^{int}$). Notably, these two subsets appeared to have increased TCF-1 expression. Both CD39 and TCF-1 have been recently implicated in relation to NARTs and ICB. The expression of CD39 has generally been associated with tumor-reactive T cells, allowing the distinction from bystander T cells in the TME, although, CD39 has generally been linked to a dysfunctional, terminally differentiated phenotype[22–24]. TCF-1, the stem cell-like marker, has been recently reported to provide T cells with self-renewal properties, although this tends to get downregulated in terminally exhausted T cells, i.e. in the context of chronic viral infection and cancer[25–28].

The characteristics of neoepitope immunogenicity revealed that neither the predicted MHC binding affinity nor the neoepitope expression level was able to predict T cell recognition, within the range tested, but the neopeptide hydrophobicity seemed to influence the neoepitope immunogenicity. Neopeptide hydrophobicity has been recently reported to play a role in TCR recognition[29]. However, to improve the accuracy of neopeptide prediction, these parameters, and others, may need to be incorporated into a combined model. This is particularly relevant, considering the low fraction of predicted neopeptides that result in T cell recognition[30]. In general, the fraction of mutations resulting in T cell recognition was highest for neoepitopes deriving from frameshift and missense mutations, indicating the potential use of these mutational signatures as an immune predictor. This notion has previously been supported in melanoma cohorts, where high levels of frameshift mutations were associated with improved response to ICB therapy[31].

As a final glance into potential treatment-related signatures, the differential gene expression analysis from the TME pre-treatment indicates that there are intrinsic properties of the TME that may dictate the therapeutic outcome. This signature does not seem to be related to the presence of NARTs and hence implies that the pre-existing immune contexture of the TME may be the primary driver of therapeutic outcome in this study. This would support a recent observation that the pre-existing anti-tumor immunity in the TME ultimately dictates the outcome of ICB therapy[8].

Taken together, this preliminary data should however be interpreted with caution. Due to the small cohort size, the heterogeneous nature of the patients enrolled and the lack of long-term follow-up samples, it is difficult at this time to elucidate explicit conclusions. Further research would include additional studies in a larger patient cohort, to allow a more comprehensive evaluation of the kinetics of NARTs as well as their phenotypic traits. An objective of further research in our study would be to investigate the clonality of the predicted neoantigens, as subclonal neoantigens may

be substantially contributing to the total mutational burden. The lack of immunogenic neoantigens (or presence of high subclonal neoantigens) could be a potential mechanism of acquired ICB resistance, as highlighted by multiple reports[17,32,33]. The clonal evolution of the tumor along the course of therapy promotes the emergence of novel mutations, which may contribute to the acquired resistance in ICB. This treatment-dependent immunoediting has been observed in NSCLC patients who have not benefited from ICB[34].

The use of sensitive, high-throughput T cell detection methods, such as DNA barcode-labeled MHC multimers, combined with T cell phenotyping, allows the ability to detect and characterize NARTs in tumor biopsies and peripheral blood. This preliminary data shows promise, as it would suggest the possibility of monitoring the characteristics of T cell immune responses during ICB and using this as an immune predictor for clinical outcome in multiple cancer types.

## Supplementary Tables and Figures

**Supplementary Table S1:** Clinical data

| Patient ID | Diagnosis | Checkpoint inhibitor treatment | Number of treatments | RECIST (best obtained) | Biopsy site | Number of prior treatments |
|---|---|---|---|---|---|---|
| RH08 | STAD | Nivolumab + LAG3 | 4 | PD | Liver[1] | 2 |
| RH10 | LIHC | Nivolumab + LAG3 | 13 | CR | Liver[1] | 2 |
| RH11 | BLCA | Pembrolizumab | 15 | PR | Lymph node | 1 |
| RH13 | CRC | Atezolizumab + CD3 | 6 | PD | Liver[1] | 3 |
| RH15 | OV | Atezolizumab + BET inhibitor | 4 | PD | Subcutaneous | 6 |
| RH16 | BRCA | Chemo + Pembrolizumab | 9 | PR | Lymph node | 3 |
| RH17 | BRCA | Chemo + Pembrolizumab | 6 | PD | Lymph node | 1 |
| RH18 | CRC | Atezolizumab + CD3 | 2 | PD | Liver[1] | 2 |
| RH19 | OV | Atezolizumab + BET inhibitor | 8 | SD | Lymph node | 3 |
| RH21 | CRC | Atezolizumab + CD40 | 4 | PD | Liver[1] | 4 |
| RH22 | HCC | Nivolumab + LAG3 | * | CR | Liver[1] | * |
| RH24 | GAC | Atezolizumab + CD40 | * | PD | Liver[1] | * |
| RH25 | UPT | Atezolizumab + CD3 | * | PR | Liver[1] | * |
| RH27 | BRCA | Atezolizumab + BET inhibitor | * | PD | Lymph node | * |
| RH29 | OV | Atezolizumab + BET inhibitor | * | PD | Subcutaneous | * |
| RH30 | MPM | Pembrolizumab | * | PD | Lymph node | * |
| RH31 | NSCLC | Nivolumab | * | PD | Liver[1] | * |
| RH33 | NSCLC | Pembrolizumab | * | PD | Lymph node | * |
| RH34 | MPM | Atezolizumab + CD40 | * | SD | Pleura | * |
| RH35 | NSCLC | Pembrolizumab | * | PD | Liver[1] | * |

STAD; Stomach adenocarcinoma, LIHC; Liver hepatocellular carcinoma, BLCA; Bladder Urothelial Carcinoma, CRC; Colorectal cancer, HCC; Hepatocellular carcinoma, GAC; Gastric carcinoma, UPT; Unknown primary tumor, BRCA; Breast invasive carcinoma, OV; Ovarian serous cystadenocarcinoma, MPM; Malignant pleural mesothelioma, NSCLC; Non-small-cell lung carcinoma. [1]Metastatic site. * Information not available

**Supplementary Table S2:** The number of neoepitopes recognized in the 20 patients' samples

| | TIL | | REP-TIL | | PBMC | | | Number of samples |
|---|---|---|---|---|---|---|---|---|
| | Before | After[1] | Before | After[1] | Before | After[2] | After[3] | |
| RH08 | - | 1 | - | - | 3 | 1 | 2 | 4 |
| RH10 | 1 | 1 | 1 | - | 0 | 0 | 0 | 7 |
| RH11 | - | - | - | 8 | 9 | 5 | 2 | 4 |
| RH13 | - | 0 | - | - | 0 | 0 | 1 | 4 |
| RH15 | 0 | 1 | 0 | 0 | 0 | 0 | 0 | 7 |
| RH16 | 0 | 4 | 5 | 6 | 2 | 1 | 2 | 7 |
| RH17 | - | 0 | - | 0 | 0 | 0 | 0 | 5 |
| RH18 | - | - | - | - | - | 0 | - | 1 |
| RH19 | 2 | 0 | 3 | 0 | 1 | 0 | 1 | 7 |
| RH21 | 1 | - | - | - | 2 | 0 | - | 3 |
| RH22 | 0 | - | 0 | - | 0 | 0 | - | 4 |
| RH24 | 3 | 0 | 1 | 3 | 3 | 5 | 7 | 7 |
| RH25 | 4 | 0 | 4 | 1 | 3 | 5 | 5 | 7 |
| RH27 | - | - | 1 | 4 | 3 | 2 | - | 4 |
| RH29 | 1 | - | - | 0 | 0 | 0 | 0 | 5 |
| RH30 | 0 | 0 | 0 | - | 0 | 0 | - | 5 |
| RH31 | 2 | 10 | - | - | 8 | 6 | - | 4 |
| RH33 | 6 | 12 | 7 | 2 | 16 | 16 | - | 6 |
| RH34 | - | 0 | 0 | 0 | 3 | 0 | 3 | 6 |
| RH35 | 2 | 2 | 1 | 4 | 4 | 2 | - | 6 |

[1] Average 33 days after treatment initiation. [2] Average 34 days after treatment initiation [3]Average 86 days after treatment initiation. [4]Average 26 weeks after treatment initiation. - samples not available or excluded due to <5000 live $CD8^+$ T cells. TIL; Tumor infiltrating lymphocytes; REP; Rapid expansion protocol, PBMC; Peripheral blood mononuclear cells.

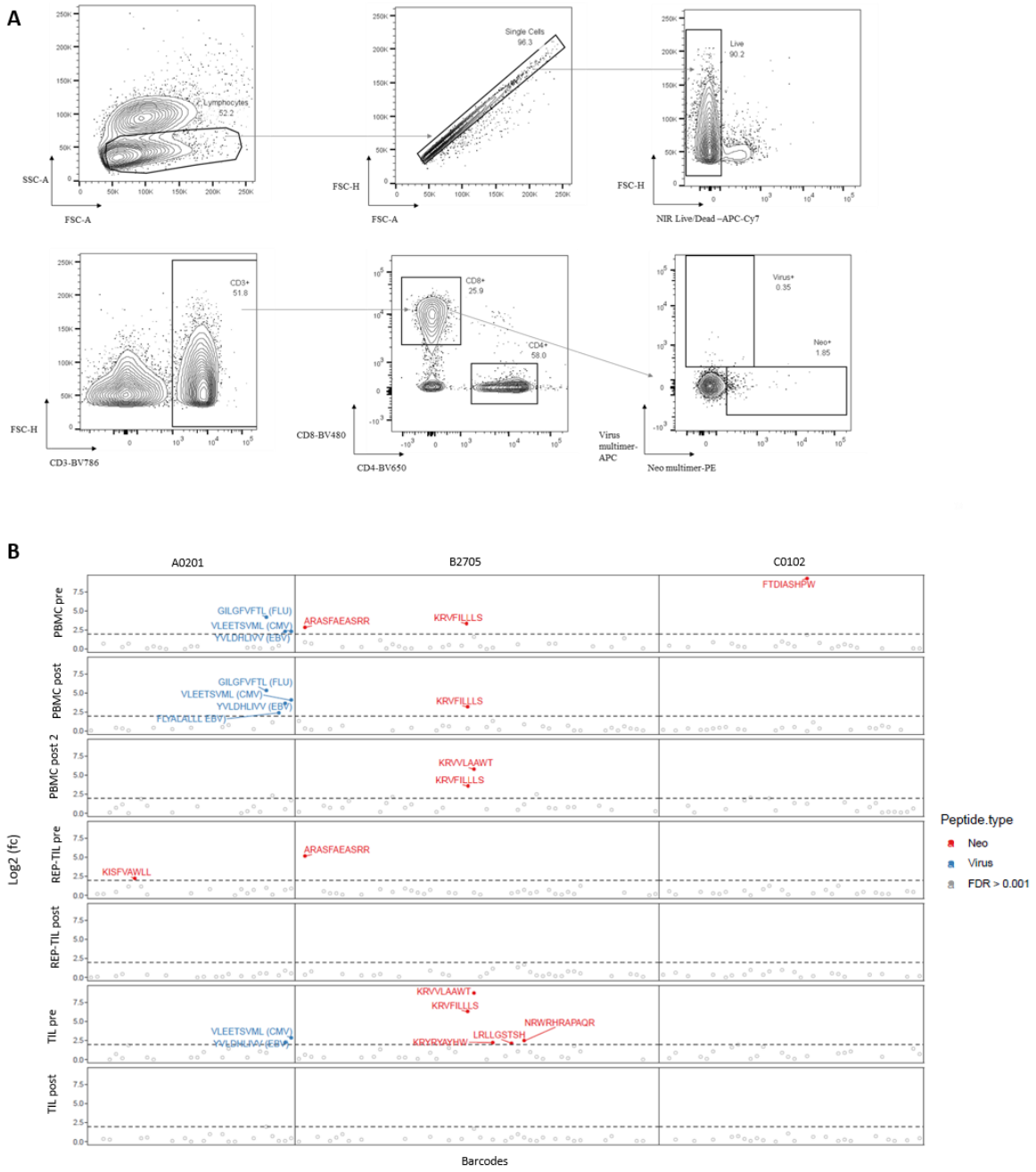


**Supplementary Figure S1.**

**A,** Representative gating strategy for sorting multimer+ CD8 T cells from bulk PBMCs.

**B,** Summary plot for detected T cell reactivity for patient 25 (RH25). This plot is segregated vertically by the different PBMC and TIL samples, and horizontally by the HLA types included in the patient-specific panel. The Log2 fold change (fc) depicts DNA barcodes that have been positively enriched in the given sample, and a threshold Log2 (fc) value of > 2 depicts where significant T cell reactivity ($p < 0.001$) has been detected towards the neopeptide (red) or viral control peptide (blue).

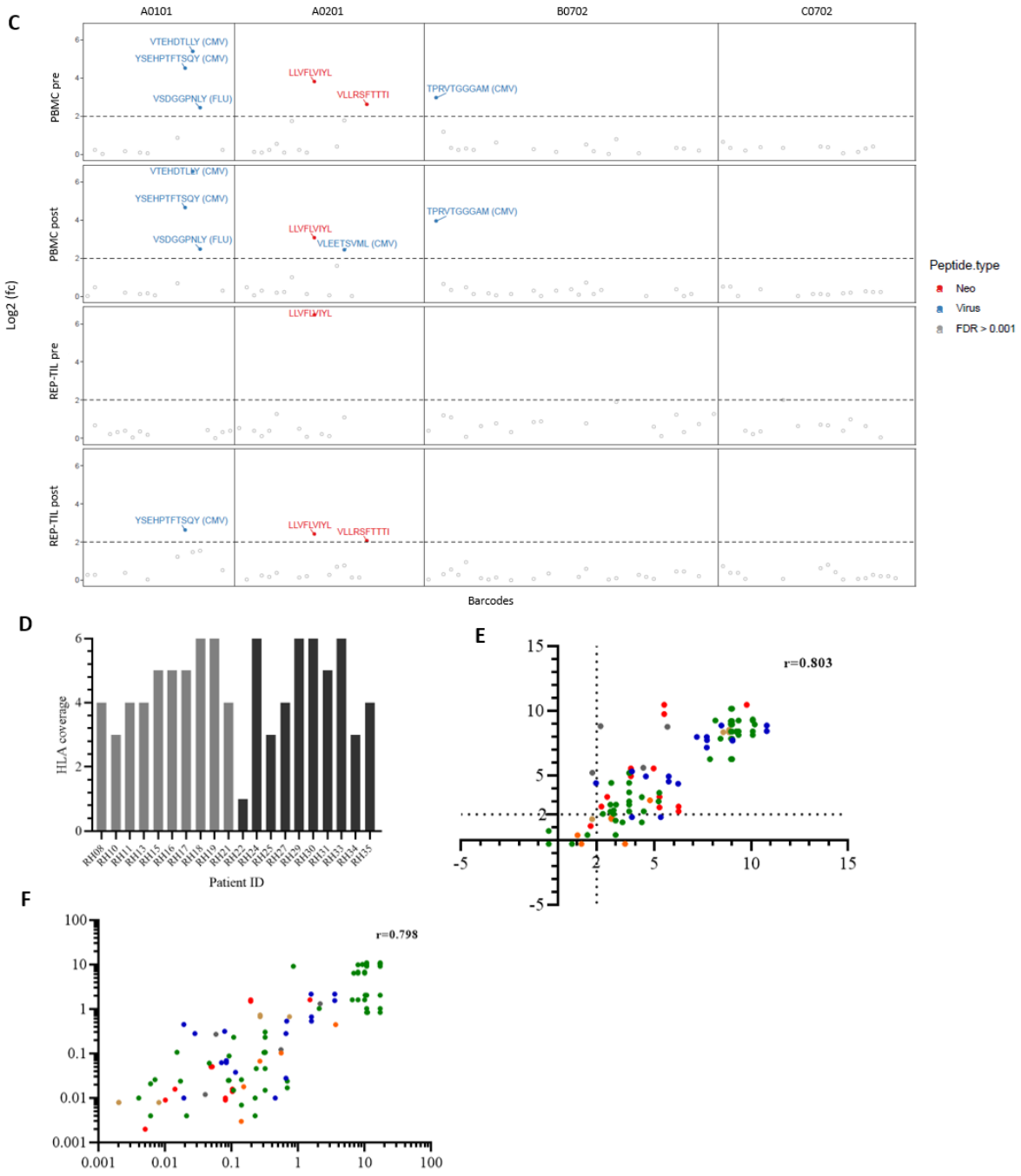


**Supplementary Figure S1.**

**C,** Summary plot for detected T cell reactivity for patient 27 (RH27). This plot is segregated vertically by the different PBMC and TIL samples, and horizontally by the HLA types included in the patient-specific panel. The Log2 fold change (fc) depicts DNA barcodes that have been positively enriched in the given sample, and a threshold Log2 (fc) value of > 2 depicts where significant T cell reactivity ($p < 0.001$) has been detected towards the neopeptide (red) or viral control peptide (blue). **D**, Number of HLA types, i.e. HLA coverage, that were available for generating each of the patient-specific multimer panels. **E-F**, Correlation plots for detected T cell reactivity against viral epitopes in the healthy donor controls that were screened multiple times, represented as Log2 (fc) values (E) or estimated frequency values (F). The color scheme depicts the various healthy donor controls.

**A**

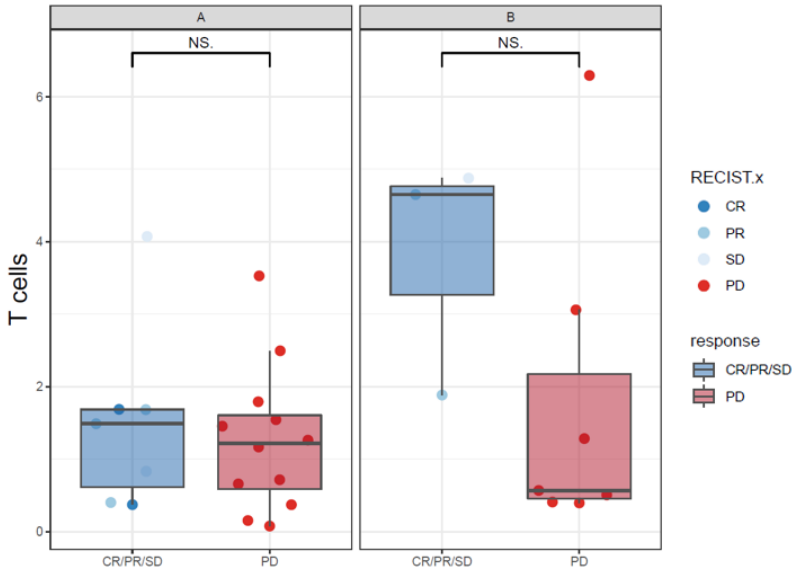


**B**

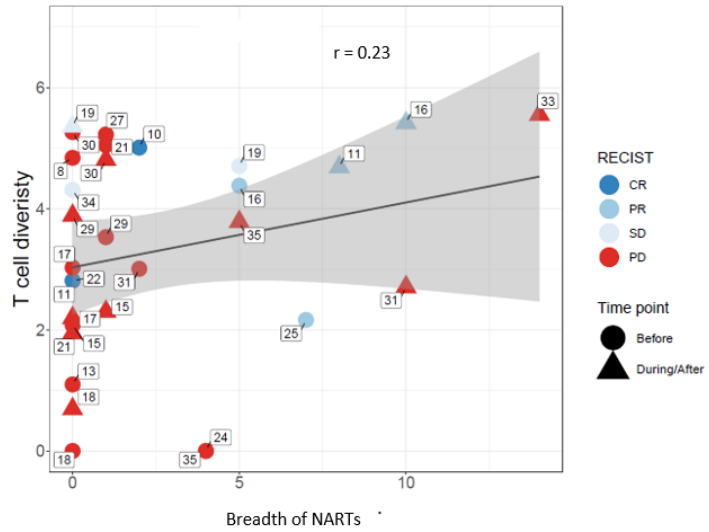


**Supplementary Figure S2.**

**A,** Estimate of T cell abundancy based on RNA-seq data from the tumor microenvironment, determined using microenvironment cell populations counter (MCP counter), pre-treatment (left) and post-treatment (right).

**B**, Correlation of T cell diversity, calculated based on RNA-seq data from the tumor microenvironment, and the breadth of the detected NARTs for all of the patients. CR; Complete responder, PR; Partial responder, SD; Stable disease, PD; Progressive disease.

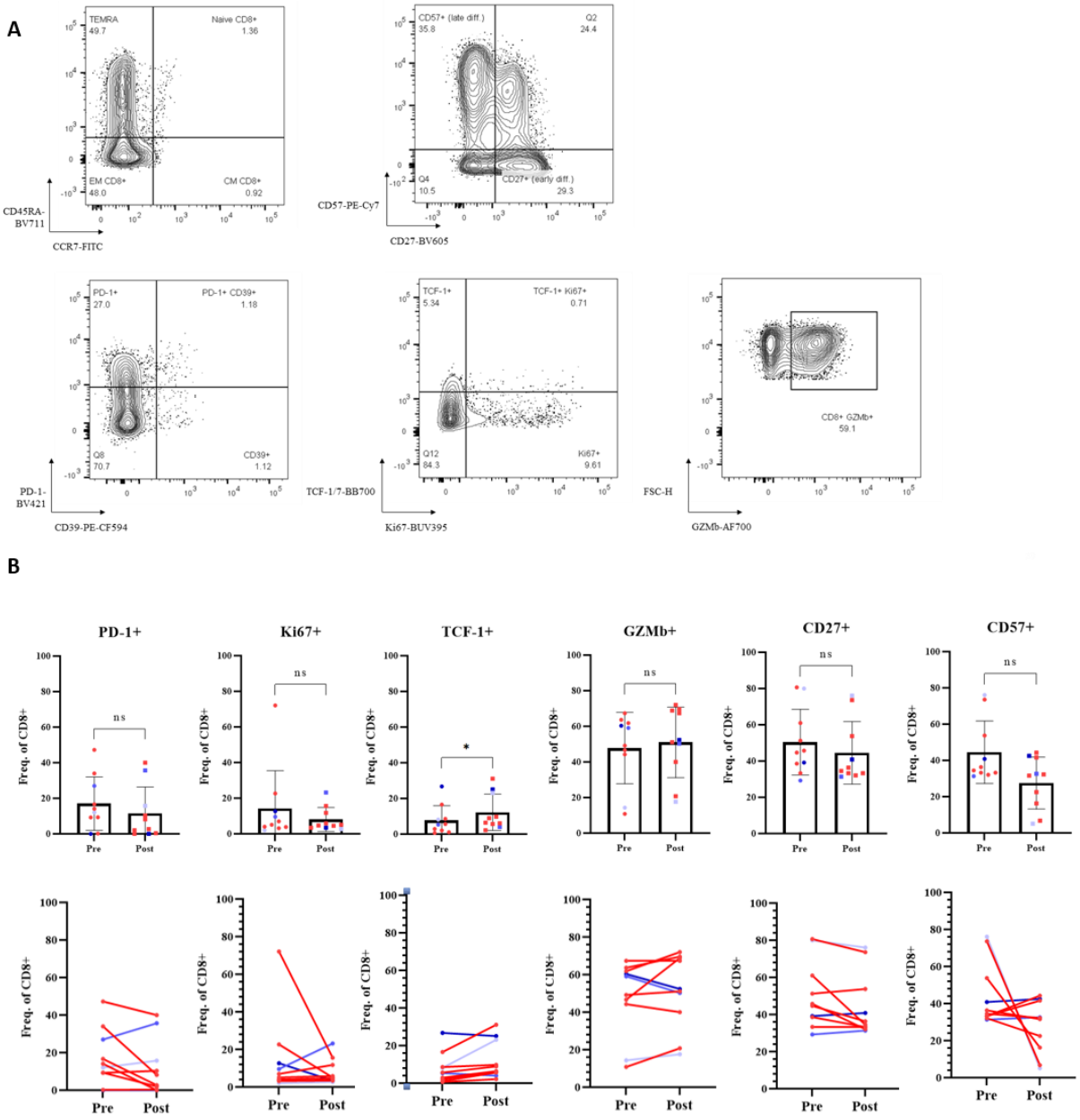


**Supplementary Figure S3.**

**A,** Representative gating strategy for the phenotypic analysis of bulk CD8⁺ T cells from bulk PBMCs. Pre-gated on lymphocytes, singlets, live, CD3⁺ and CD8⁺.

**B,** Plotting of selected markers based on manual gating from flow plots for bulk CD8⁺ T cells from PBMCs, pre- and post-treatment. The data is depicted either as unpaired values (top) or paired values (bottom) for pre- and post-treatment. Significance for B is denoted based on the Mann Whitney test.

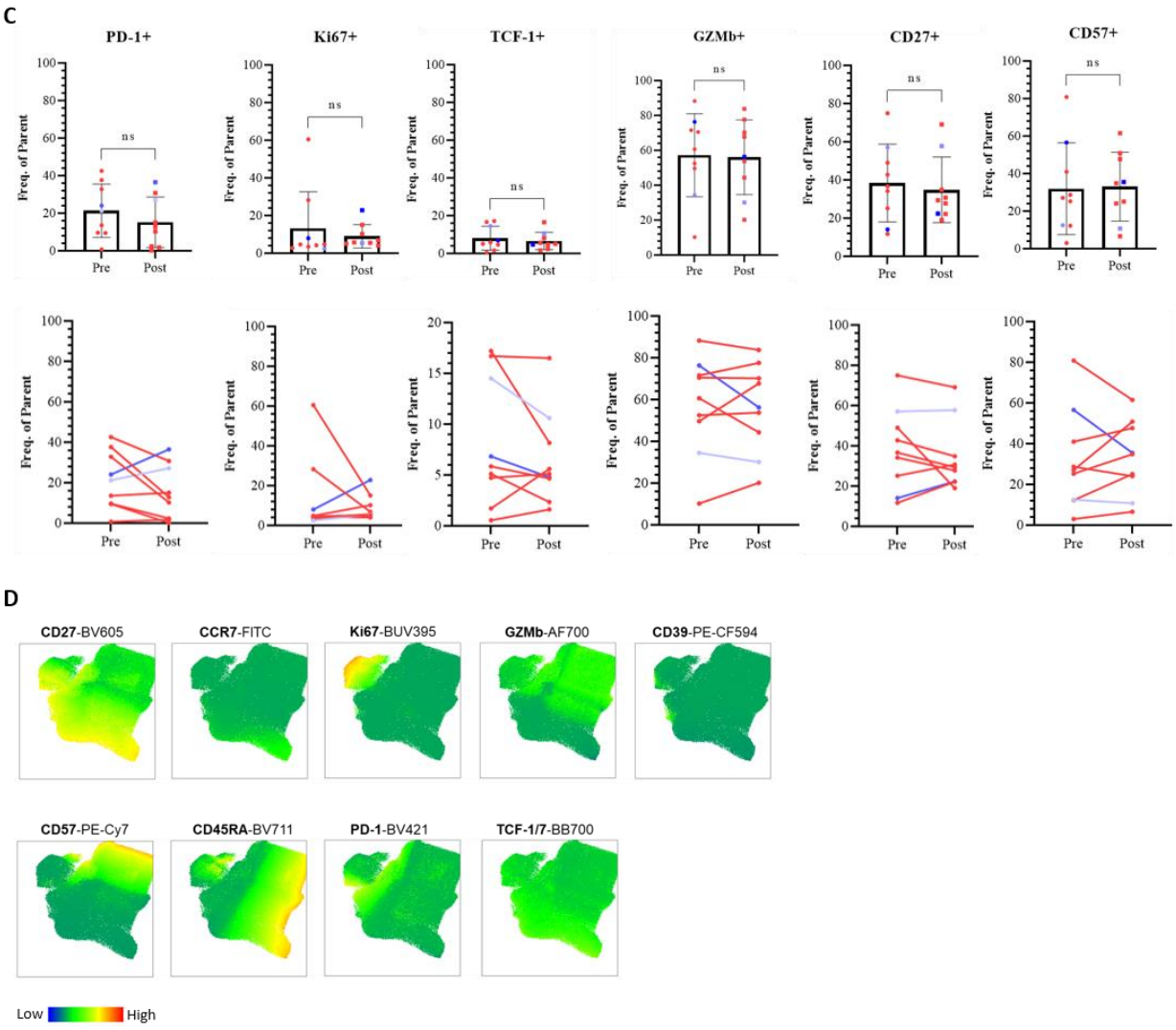


**Supplementary Figure S3.**

**C,** Plotting of selected markers based on manual gating from flow plots for NARTs from PBMCs, pre- and post-treatment. The data is depicted either as unpaired values (top) or paired values (bottom) for pre- and post-treatment.

Significance is denoted based on the Mann Whitney test.

**D**, UMAP representation, colored by protein expression, for bulk CD8⁺ T cells from PBMCs.

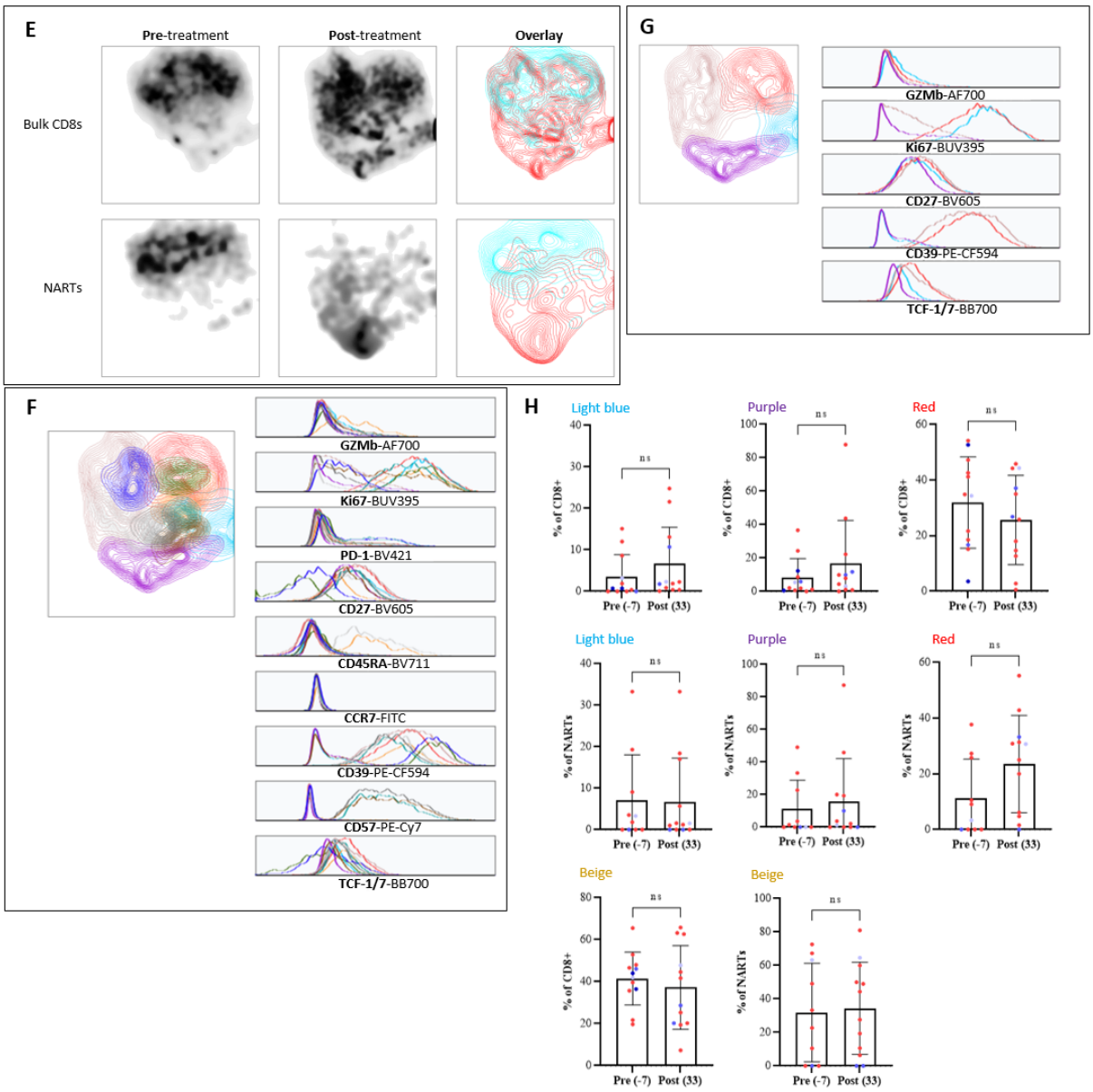


**Supplementary Figure S3. Phenotypic characterization of bulk CD8⁺ T cells and NARTs from patient-derived TILs**
**E,** UMAP representation of the global structure of bulk CD8⁺ T cells (top) and NARTs (bottom) from all patients, pre- and post-treatment depicted as density and overlay plots (light blue: pre-treatment, red: post-treatment).
**F,** Overlay of FlowSOM clustering on UMAP, with conjunct histograms to visualize and identify the sub-populations within the global structure.
**G,** Selected sub-populations from the FlowSOM clustering and histograms for the corresponding phenotypic profiles.
**H,** Quantitative assessment of the FlowSOM clustering for the selected sub-populations, depicting the frequency of CD8⁺ T cells or NARTs that the particular sub-populations represent. For all the plots related to frequency of bulk CD8⁺ T cells: (-7, n = 12; 33, n = 12) and for all plots related to frequency of NARTs: (-7, n = 10; 33, n = 12). Significance for D is denoted based on the Mann Whitney test.

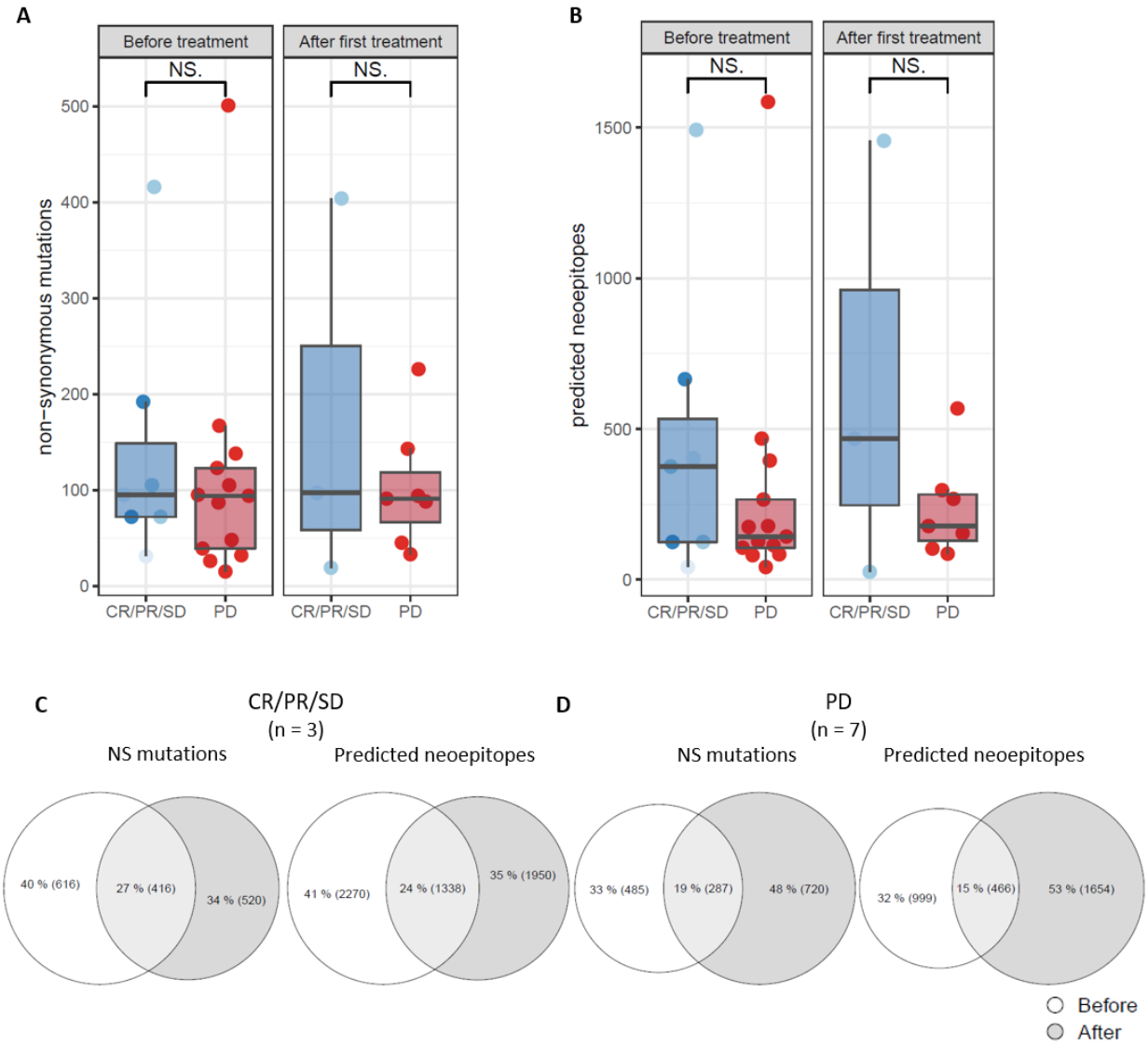


**Supplementary Figure S4. Tumor mutational burden and predicted neopeptides**

**A,** Comparison of the number of non-synonymous mutations detected either before (left) or after (right) treatment initiation between the non-progressive disease patients (CR/PR/SD) and the PD patients. Significance levels denoted based on the Mann-Whitney test. **B,** Comparison of the number of neopeptides predicted from the tumor sequencing data obtained either before (left) or after (right) treatment initiation between the non-progressive disease patients (CR/PR/SD) and the PD patients. Significance levels denoted based on the Mann-Whitney test. **C,** Venn Diagrams for the non-progressive disease patients with tumor sequencing data available before and after therapy initiation (n = 3). Average number of non-synonymous mutations (left) or predicted neopeptides (right) present in either sequencing data before (white), after (grey) or at both time points. **D,** Venn Diagrams for the PD patients with tumor sequencing data available before and after therapy initiation (n = 7). Average number of non-synonymous mutations (left) or predicted neopeptides (right) present in either sequencing data before (white), after (grey) or at both time points. CR; Complete responder, PR; Partial responder, SD; Stable disease, PD; Progressive disease, NS; non-synonymous.

## Materials and Methods

### Patient cohort

Twenty patients with solid metastatic tumors referred to treatment with checkpoint inhibitors at the Phase 1 Unit - Rigshospitalet, Copenhagen, Denmark, were included in this study. Inclusion criteria for immune therapy: performance status (ECOG scale) up to 1, age above 18 years, and at least one metastatic lesion accessible for radiologically-guided biopsy. Moreover, patients were required to have at least one measurable lesion according to response evaluation criteria in solid tumors version 1.1 (RECIST v.1.1), which was also used for assessing treatment response. The best-obtained RECIST response lasting for at least 2 months was registered. Clinical data are presented in Supplementary Table S1.

### Patient and healthy donor samples

Fresh tumor biopsies were obtained before initiation of therapy and approximately 40 days after treatment commencement from the same metastatic site. Immediately after collection, the tumor biopsies were stored in media containing RPMI1640 (Thermo Fischer Scientific), penicillin, streptomycin, and fungizone (Bristol-Meyers Squibb) for transport (elapsed time of one hour). Biopsies were minced manually under sterile conditions into smaller fragments and placed into 24-well plates (Nunc, Roskilde, Denmark) containing 2 mL of culture medium (90% RPMI1640, penicillin, streptomycin, fungizone, 10% heat-inactivated Human AB Serum) and 6000 UI/mL IL-2 (Proleukin, Novartis, Basel, Switzerland). Plates were kept in incubators (humidified atmosphere, temperature around 37˚C and 5% $CO_2$) for five days. Afterward, half of the medium in each well was removed and replenished with 1 mL of culture medium containing interleukin 2 (same concentration as described above). The same procedure was repeated afterwards every second day. Young TILs were pooled around five-six weeks after the biopsy date and cryopreserved similarly as for PBMCs. Further expansion of REP-TILs *in vitro* was done by irradiated allogeneic feeder cells (PBMCs from healthy donors), anti-CD3 antibody, and IL-2 for 14 days as described by Andersen and colleagues[35]. It is important to note that for all of the plotting and statistical analysis of this study, the young TILs and REP-TILs were grouped. This was due to inconsistent TIL/REP-TIL availability among the patients. Additionally, there were no follow-up biopsies taken at day 86, so the TILs represent just two time points. Blood samples were collected for isolation of PBMCs on the same day as biopsies carried out. The third collection of blood samples took place approximately 26 weeks after treatment start if patients were still in treatment. PBMCs were isolated from whole blood by density centrifugation on Lymphoprep (Axis-Shield PoC) in Leucosep tubes (Greiner Bio-One) and cryopreservation in inactivated Human AB serum with 10% DMSO. Samples were initially stored at -80°C alcohol-free freezing containers (Cool cell, Biocision) for 24 hours and then stored at -140˚C until further use.

Healthy donor blood samples were obtained from the blood bank at Rigshospitalet, Copenhagen, Denmark. PBMCs were isolated from whole blood as described for the PBMCs from the patients and cryopreserved at -150°C in fetal calf serum (FCS, Gibco) with 10% dimethyl sulfoxide

(DMSO, Sigma-Aldrich). All healthy donor and patient materials were collected under approval by the Scientific Ethics Committee of the Capital Region, Denmark, with written informed consent obtained according to the Declaration of Helsinki.

**Molecular analysis of tissue biopsies**

Fragments of tumor biopsies stored in RNAlater (Sigma-Aldrich) for DNA and RNA extraction. In short, DNA and RNA were isolated using the AllPrep DNA/RNA kit (Qiagen). For blood samples, genomic DNA was extracted using a Tecan automation workstation (Promega). DNA whole-exome sequencing (WES, Illumina platform) and mRNA expression arrays (Human U133 Plus2.0, Affymetrix) were performed on extracted material.

**Next-generation sequencing data analysis**

The WES and RNA-seq data were processed according to the Genome analysis tool kit best practice guidelines for somatic variant calling[36]. First, raw reads were trimmed to a minimum length of 50 bp and quality-checked to a Phred score of 20 using Trim Galore 0.4.0[37], combined with Cutadapt[38] and FastQC[39]. The human genome (GCh38) was used to align the reads using the Burrows-Wheeler Aligner[40] version 0.7.16a. Duplicate reads were marked with Picard-tools MarkDuplicates version 2.9.1. To reduce false-positive variant calls, base recalibration was performed with GATK version 4.0.1.1. Contamination tables were made by GATK´s Calculate Contamination and used as input for MuTect2[41], which call somatic mutations from matched tumor and normal samples. RNA sequencing was processed by TrimGalore (0.4.0) and Kallisto version 0.42.1 was used to find expression information. HLA alleles of each patient were determined by first filtering the reads and aligning them to the HLA region using RazerS version 3.4.0[42]. Secondly, Optitype 1.2[43] was used to type each patient's HLA alleles.

**Assessment of TMB and neoepitope load**

The total tumor mutational burden of all mutations acquired in each tumor was assessed by counting each entry passing the filtering criteria of GATK4's MuTect2 output VCF file. This VCF file was given as input to the neoepitope predictor MuPeXI 1.2.0[44] together with RNA-seq expression values obtained from Kallisto in transcripts per million (TPM) and the HLA alleles detected by OptiType. The output neopeptides were selected based on an expression above 0.1 TPM and a predicted binding eluted ligand percentile rank (EL %Rank) score below 2. The amount of non-synonymous mutations is determined from the log-files, which is output from MuPeXI, and the mutation types were determined with Variant effect predictor (VEP), version 87 which is incorporated in MuPeXI. The neoepitope predictor MuPeXI provides the corresponding wild-type peptide for any predicted neopeptide. For single nucleotide variants (SNVs) and in-frame indels (deletions and insertions), it is the unmutated amino acid sequence in the reference proteome. However, for frameshift indels, the reference proteome is searched for the most similar peptide with up to four mismatches. This will be defined as the nearest normal peptide to the neopeptide[44].

**Peptides**

All selected mutation-derived and virus control peptides were purchased from Pepscan (Pepscan Presto BV, Lelystad, Netherlands) and dissolved to 10 mM in DMSO and stored at -20˚C.

**Determination of T cell diversity by CDR3 sequence identification from RNA-seq**

MiXCR[45] version 2.1.1 was used to determine CDR3 sequences from bulk RNA-seq data with the optimized setting for this specific purpose[46]. The quality trimmed reads from RNA-seq were used as input to MiXCR, which identify specific clones with reference to known CDR3 sequences from the ImMunoGeneTics (IMGT) database. The clone count of each clone detected refers to the reads aligning to this specific clone of the CDR3 reference library. Shannon entropy[47] was calculated as a T cell diversity measurement[48].

**Tumor Microenvironment analysis including differential expression analysis and microenvironment cell populations-counter**

From bulk tumor RNA sequencing, a differential expression analysis both comparing patient outcome, split by CR/PR/SD and PD as well as the difference in high and low detected NART, split by the median. The analysis was performed with DeSeq2[49] version 1.26.0 from BiocManger in R version 3.6.1 with default option where the input was obtained from Kallisto version 0.42.1. Differentially expressed genes were found with a threshold of adjusted p-value < 0.05 and illustrated using ComplexHeatmap from Bioconductor[50] in R version 4.0.2. The T cell abundancy estimate was found using MCP-counter[51] the Kallisto output from the bulk RNA sequencing data and as input in R version 4.0.2 with the ebecht/MCPcounter packages from GitHub in R version 4.0.2 with Hugo-symbols as feature Type.

**MHC monomer production and generation of specific peptide-MHC complexes**

The production of MHC monomers was performed as previously described[52,53]. In brief, human $\beta_2$ microglobulin ($\beta_2$m) light chain and the heavy chains of the included HLA types were expressed in bacterial Bl21 (DE3) pLysS strain (Novagen, cat#69451) and purified as inclusion bodies. Followed by folding of heavy chain and β2m light chain complexes with a UV-sensitive ligand[54,55], biotinylation with BirA biotin-protein ligase standard reaction kit (Avidity, 318 LLC-Aurora, Colorado), and purification using size-exclusion column (Waters, BioSuite125, 13µm SEC 21.5 × 300 mm) HPLC (Waters 2489). Specific peptide-MHC (pMHC) complexes were generated by UV-induced peptide exchange[52,54].

**Detection of peptide-MHC specific T cells by DNA barcode-labeled multimers and phenotypic characterization**

Patient-specific libraries of predicted neopeptides and virus control peptides were generated as previously described[56]. In brief, PE and/or APC - labeled dextran backbones were first coupled with DNA barcodes followed by the pMHC complexes, generated above. Hence, a specific peptide was given a unique DNA barcode together with either a PE or APC-fluorescent label. Patient samples and healthy donor PBMCs were stained with an up-concentrated pool of all multimers in the presence of 50 nM dasatinib. Followed by staining with an antibody mix composed of CD8-BV480 (BD, cat#566121, clone RPA-T8), dump channel antibodies (CD4-FITC (BD, cat#345768), CD14-FITC (BD, cat#345784), CD19-FITC (BD, cat#345776), CD40-FITC (Serotech, cat#MCA1590F), and CD16-FITC (BD, cat#335035)) and a dead cell marker (LIVE/DEAD Fixable Near-IR; Invitrogen, cat#L10119). The samples included for T cell

phenotypic characterization were stained with a separate antibody cocktail containing T cell lineage markers (CD3-BV786 (BD, cat. #563799, clone SK7), CD4-BV650 (BD, cat. #563876), and CD8-BV480 (BD, cat. #566121, clone RPA-T8)), characterization markers (Ki67-BUV395 (BD, cat. #564071, clone B56), PD1-BV421 (BD, cat. #562516, clone EH12.1), CD27-BV605 (BioLegend, cat. #302830, clone O323), CD45RA-BV711 (BD, cat. #563733, clone HI100), CCR7-FITC (BioLegend, cat. #353215, clone G043H7), CD39-PE-CF594 (BD, cat. #563678, clone Tu66), CD57-PECy7 (BioLegend, cat. #393310, clone QA17A04), GranzymeB-AlexaFlour700 (BioLegend, cat. #372221, clone 581 QA16A02)), TCF-1/7-BB700 (BD, cat. #353988, clone S33-96C) and a dead cell marker (LIVE/DEAD Fixable Near-IR; Invitrogen, cat. #L10119). Multimer-binding T cells were sorted as lymphocytes, single, live, $CD8^+$, $FITC^-$ and $PE^+/APC^+$ and pelleted by centrifugation. DNA barcodes were amplified from the isolated cells and a stored aliquot of the multimer pool used for staining (diluted 50,000× in the final PCR reaction, used as a baseline). PCR products were purified with a QIAquick PCR Purification kit (Qiagen, cat#28104) and sequenced using an Ion Torrent PGM 316 or 318 chip (Life Technologies) at PrimBio, USA. Sequencing data were processed by the software package Barracoda (available online at http://www.cbs.dtu.dk/services/barracoda). Barracoda identifies the DNA barcodes annotated for a given experiment, assigns a sample ID and pMHC specificity to each DNA barcode, and counts the total number of reads and clonally reduced reads for each peptide-MHC-associated DNA barcode. A $Log_2$ fold change value is estimated through mapping read counts in a given sample relative to the mean read counts of the triplicate baseline samples using normalization factors determined by the trimmed mean of M-values method. FDRs were estimated using the Benjamini–Hochberg method. A threshold of at least 1/1,000 reads associated with a given DNA barcode relative to the total number of DNA barcode reads in that given sample was set to avoid false-positive detection of T cell responses due to a low number of reads in the baseline samples. An estimated cell frequency was calculated for each DNA barcode from the read count fraction out of the percentage of $CD8^+$ $multimer^+$ T cells. DNA barcodes with a FDR < 0.1%, equal to $p < 0.001$, were considered to be significant T cell responses. Samples with low viability of $CD8^+$ T cells (< 5000 cells) were excluded and DNA barcodes enriched in both patient samples and healthy donor controls were excluded as technical background.

**Confirmatory tetramer staining**

Patient-specific neopeptides and viral control peptides were diluted to 200 µM in PBS. MHC monomers were diluted to 150 µg/mL and mixed in a 1:1 ratio (vol) with diluted peptides. pMHC complexes were generated by UV-induced peptide exchange. pMHC complexes were centrifuged at 3300 g, 4C for 5 min and the supernatant was transferred to a new plate. APC-labeled streptavidin (BioLegend, 0.2 mg/mL) was then added stepwise to the pMHC complexes. After a cumulative 30 min of incubation on ice, the MHC tetramers (10ug/mL) were incubated with freshly thawed PBMCs in the presence of 50 nM dasatinib. Followed by staining with an antibody mix composed of CD8-BV480 (BD, cat#566121, clone RPA-T8), dump channel antibodies (CD4-FITC (BD, cat#345768), CD14-FITC (BD, cat#345784), CD19-FITC (BD, cat#345776), CD40-

FITC (Serotech, cat#MCA1590F), and CD16-FITC (BD, cat#335035)) and a dead cell marker (LIVE/DEAD Fixable Near-IR; Invitrogen, cat#L10119).

**Flow cytometry and phenotypic analysis**

All flow cytometry experiments were carried out on FACSMelody and FACSAria Fusion instruments (BD Biosciences). Data were analyzed in FlowJo version 10.7.1 (TreeStar, Inc). For UMAP dimensionality reduction, PBMCs or TILs were pre-gated on lymphocytes, singlets, live, $CD3^+$ and $CD8^+$. The $CD8^+$ populations were then concatenated for the PBMCs (n = 25) or the TILs (n = 24) and subsequently down-sampled to 200000 cells with DownSample v3.3. UMAP v3.1 was then run with the selection of Ki67, PD-1, CD27, CD57, CCR7, CD45RA, CD39, GZMb and TCF-1, with default settings (Euclidean distance function, nearest neighbor value of 15, and a minimum distance of 0.5). The unsupervised clustering algorithm, FlowSOM v2.9, was then run with the selection of 15 meta clusters.

**Data analysis**

The graphing and statistical analyses were conducted using GraphPad Prism 9 or R statistical software version 4.0.4. The data were assessed for normal distribution using D'Agostino-Pearson normality test. Non-parametric data were analyzed with unpaired Mann-Withney U-test or Kruskal-Wallis test with Dunn’s correction for multiple comparisons. The correlations were analyzed using Pearson’s correlation.

## References


1. Topalian, S. L. *et al.* Safety, Activity, and Immune Correlates of Anti–PD-1 Antibody in Cancer. *N. Engl. J. Med.* **366**, 2443–2454 (2012).

2. Brahmer, J. R. *et al.* Safety and Activity of Anti–PD-L1 Antibody in Patients with Advanced Cancer. *N. Engl. J. Med.* **366**, 2455–2465 (2012).

3. Robert, C. *et al.* Anti-programmed-death-receptor-1 treatment with pembrolizumab in ipilimumab-refractory advanced melanoma: A randomised dose-comparison cohort of a phase 1 trial. *Lancet* **384**, 1109–1117 (2014).

4. Snyder, A. *et al.* Genetic basis for clinical response to CTLA-4 blockade in melanoma. *N. Engl. J. Med.* **371**, 2189–2199 (2014).

5. Rizvi, N. A. *et al.* Mutational landscape determines sensitivity to PD-1 blockade in non–small cell lung cancer. *Science (80-. ).* **348**, 124–128 (2015).

6. Hellmann, M. D. *et al.* Tumor Mutational Burden and Efficacy of Nivolumab Monotherapy and in Combination with Ipilimumab in Small-Cell Lung Cancer. *Cancer Cell* **33**, 853-861.e4 (2018).

7. Blank, C. U., Haanen, J. B., Ribas, A. & Schumacher, T. N. The 'cancer immunogram'. *Science* vol. 352 658–660 (2016).

8. Bruni, D., Angell, H. K. & Galon, J. The immune contexture and Immunoscore in cancer prognosis and therapeutic efficacy. *Nat. Rev. Cancer* **20**, 662–680 (2020).

9. Bjerregaard, A. M., Nielsen, M., Hadrup, S. R., Szallasi, Z. & Eklund, A. C. MuPeXI: prediction of neo-epitopes from tumor sequencing data. *Cancer Immunol. Immunother.* **66**, 1123–1130 (2017).

10. Yost, K. E. *et al.* Clonal replacement of tumor-specific T cells following PD-1 blockade. *Nat. Med.* **25**, 1251–1259 (2019).

11. Banerjea, A., Bustin, S. A. & Dorudi, S. The immunogenicity of colorectal cancers with high-degree microsatellite instability. *World J. Surg. Oncol.* **3**, 1–9 (2005).

12. Fehlings, M. *et al.* Late-differentiated effector neoantigen-specific CD8+ T cells are enriched in non-small cell lung carcinoma patients responding to atezolizumab treatment. *Eur. J. Cancer* **110**, S2–S3 (2019).

13. Bobisse, S. *et al.* Sensitive and frequent identification of high avidity neo-epitope specific CD8 + T cells in immunotherapy-naive ovarian cancer. *Nat. Commun.* **9**, 1–10 (2018).

14. Fridman, W. H., Pagès, F., Sautès-Fridman, C. & Galon, J. The immune contexture in human tumours: Impact on clinical outcome. *Nat. Rev. Cancer* **12**, 298–306 (2012).

15. Charoentong, P. *et al.* Pan-cancer Immunogenomic Analyses Reveal Genotype-Immunophenotype Relationships and Predictors of Response to Checkpoint Blockade. *Cell Rep.* **18**, 248–262 (2017).

16. Verma, V. *et al.* PD-1 blockade in subprimed CD8 cells induces dysfunctional PD-1+CD38hi cells and anti-PD-1 resistance. *Nat. Immunol.* **20**, 1231–1243 (2019).

17. Di Benedetto, S. *et al.* Impact of age, sex and CMV-infection on peripheral T cell phenotypes: results from the Berlin BASE-II Study. *Biogerontology* **16**, 631–643 (2015).

18. Gordon, C. L. *et al.* Tissue reservoirs of antiviral T cell immunity in persistent human CMV infection. *J. Exp. Med.* **214**, 651–667 (2017).

19. Petitprez, F., Meylan, M., de Reyniès, A., Sautès-Fridman, C. & Fridman, W. H. The Tumor Microenvironment in the Response to Immune Checkpoint Blockade Therapies. *Front. Immunol.* **11**, 1–11 (2020).

20. Gupta, P. K. *et al.* CD39 Expression Identifies Terminally Exhausted CD8+ T Cells. *PLoS Pathog.* **11**, 1–21 (2015).

21. Shevchenko, I. *et al.* Enhanced expression of CD39 and CD73 on T cells in the regulation of anti-tumor immune responses. *Oncoimmunology* **9**, 1–13 (2020).

22. van der Leun, A. M., Thommen, D. S. & Schumacher, T. N. CD8+ T cell states in human cancer: insights from single-cell analysis. *Nat. Rev. Cancer* **20**, 218–232 (2020).

23. Kim, C., Jin, J., Weyand, C. M. & Goronzy, J. J. The transcription factor tcf1 in t cell differentiation and aging. *Int. J. Mol. Sci.* **21**, 1–16 (2020).

24. Escobar, G., Mangani, D. & Anderson, A. C. T cell factor 1: A master regulator of the T cell response in disease. *Sci. Immunol.* **5**, (2020).

25. Chen, Z. *et al.* TCF-1-Centered Transcriptional Network Drives an Effector versus Exhausted CD8 T Cell-Fate Decision. *Immunity* 1–16 (2019) doi:10.1016/J.IMMUNI.2019.09.013.

26. Galletti, G. *et al.* Two subsets of stem-like CD8+ memory T cell progenitors with distinct fate commitments in humans. *Nat. Immunol.* **21**, 1552–1562 (2020).

27. Chowell, D. *et al.* TCR contact residue hydrophobicity is a hallmark of immunogenic CD8+ T cell epitopes. *Proc. Natl. Acad. Sci.* **112**, E1754–E1762 (2015).

28. Schumacher, T. N. & Schreiber, R. D. Neoantigens in cancer immunotherapy. *Science (80-. ).* **348**, 69–74 (2015).

29. Turajlic, S. *et al.* Insertion-and-deletion-derived tumour-specific neoantigens and the immunogenic phenotype: a pan-cancer analysis. *Lancet Oncol.* **18**, 1009–1021 (2017).

30. O'Donnell, J. S., Long, G. V., Scolyer, R. A., Teng, M. W. L. & Smyth, M. J. Resistance to PD1/PDL1 checkpoint inhibition. *Cancer Treat. Rev.* **52**, 71–81 (2017).

31. Anagnostou, V. *et al.* Evolution of Neoantigen Landscape during Immune Checkpoint Blockade in Non–Small Cell Lung Cancer. *Cancer Discov.* **7**, 264–276 (2017).

32. Verdegaal, E. M. E. *et al.* Neoantigen landscape dynamics during human melanoma-T cell interactions. *Nature* **536**, 91–95 (2016).

33. Andersen, R. *et al.* Long-Lasting Complete Responses in Patients with Metastatic

Melanoma after Adoptive Cell Therapy with Tumor-Infiltrating Lymphocytes and an Attenuated IL2 Regimen. *Clin. Cancer Res.* **22**, 3734–3745 (2016).

34. Van der Auwera, G. A. *et al.* From FastQ data to high confidence variant calls: the Genome Analysis Toolkit best practices pipeline. *Curr. Protoc. Bioinforma.* **43**, 11.10.1-33 (2013).

35. Babraham Bioinformatics. Trim Galore!

36. Martin, M. Cutadapt removes adapter sequences from high-throughput sequencing reads. *EMBnet.journal* **17**, 10–12 (2011).

37. Babraham Bioinformatics. FastQC A Quality Control tool for High Throughput Sequence Data.

38. Li, H. & Durbin, R. Fast and accurate short read alignment with Burrows-Wheeler transform. *Bioinformatics* **25**, 1754–60 (2009).

39. Cibulskis, K. *et al.* Sensitive detection of somatic point mutations in impure and heterogeneous cancer samples. *Nat. Biotechnol.* **31**, 213–9 (2013).

40. Weese, D., Holtgrewe, M. & Reinert, K. RazerS 3: faster, fully sensitive read mapping. *Bioinformatics* **28**, 2592–9 (2012).

41. Szolek, A. *et al.* OptiType: precision HLA typing from next-generation sequencing data. *Bioinformatics* **30**, 3310–6 (2014).

42. Bjerregaard, A.-M., Nielsen, M., Hadrup, S. R., Szallasi, Z. & Eklund, A. C. MuPeXI: prediction of neo-epitopes from tumor sequencing data. *Cancer Immunol. Immunother.* **66**, 1123–1130 (2017).

43. Bolotin, D. A. *et al.* MiXCR: software for comprehensive adaptive immunity profiling. *Nat. Methods* **12**, 380–381 (2015).

44. Brown, S. D. *et al.* Defining the clonality of peripheral T cell lymphomas using RNA-seq. *Bioinformatics* **33**, btw810 (2016).

45. Shannon, C. E. A Mathematical Theory of Communication. *Bell Syst. Tech. J.* **27**, 379–423 (1948).

46. Stewart, J. J. *et al.* A Shannon entropy analysis of immunoglobulin and T cell receptor. *Mol. Immunol.* **34**, 1067–82 (1997).

47. Love, M. I., Huber, W. & Anders, S. Moderated estimation of fold change and dispersion for RNA-seq data with DESeq2. *Genome Biol.* **15**, 1–21 (2014).

48. Gu, Z., Eils, R. & Schlesner, M. Complex heatmaps reveal patterns and correlations in multidimensional genomic data. *Bioinformatics* **32**, 2847–2849 (2016).

49. Becht, E. *et al.* Estimating the population abundance of tissue-infiltrating immune and stromal cell populations using gene expression. *Genome Biol.* **17**, 1–20 (2016).

50. Rodenko, B. *et al.* Generation of peptide-MHC class I complexes through UV-mediated ligand exchange. *Nat. Protoc.* **1**, 1120–32 (2006).

51. Hadrup, S. R. *et al.* High-Throughput T-Cell Epitope Discovery Through MHC Peptide Exchange. in *Methods in Molecular Biology* vol. 524 383–405 (2009).

52. Toebes, M. *et al.* Design and use of conditional MHC class I ligands. *Nat. Med.* **12**, 246–251 (2006).

53. Bakker, A. H. *et al.* Conditional MHC class I ligands and peptide exchange technology for the human MHC gene products HLA-A1, -A3, -A11, and -B7. *Proc. Natl. Acad. Sci.* **105**, 3825–3830 (2008).

54. Bentzen, A. K. *et al.* Large-scale detection of antigen-specific T cells using peptide-MHC-I multimers labeled with DNA barcodes. *Nat. Biotechnol.* **34**, 1037–1045 (2016).

# 5 ADDITIONAL RESULTS I

## A method for generating off-the-shelf barcode-labeled MHC tetramers for interrogation of antigen-specific T cells

### Introduction

Higher-order MHC multimers such as the previously introduced dextran-based, Dextramers®, are now routinely used assays for the detection of antigen-reactive T cells. The dextran-based backbones are dually functionalized with both streptavidin and fluorochrome. Streptavidin provides binding sites for biotinylated MHC molecules, whereas the fluorochrome provides a means of sorting multimer-binding T cells. Other than being very expensive reagents, there is currently a limitation with the number of commercially available fluorescent dextran backbones for the assembly of such higher-order multimers (Immudex and Fina Biosolutions, to name a couple), with the availability of only PE and APC labels. There is, however, the flexibility offered with the use of MHC tetramers as opposed to Dextramers®, as there is a large variety of commercially available fluorescent streptavidin reagents, at a more reasonable price. In a similar manner to Dextramers®, MHC tetramers may also be tagged with an oligonucleotide barcode, albeit on the streptavidin core and not the streptavidin-functionalized dextran.

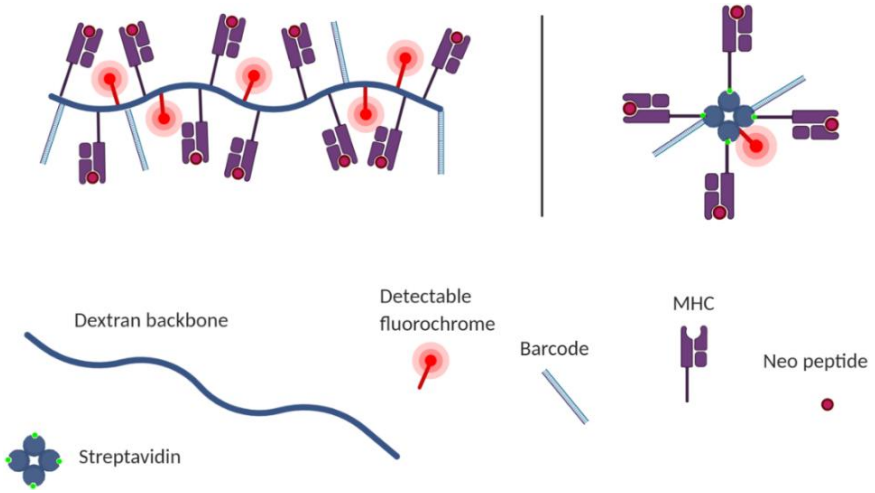


**Figure 1**. Schematic representation of DNA barcode labeled MHC multimers. A) Higher-order Dextramer® assembled from a dextran backbone dually functionalized with streptavidin and fluorochrome, B) Barcoded tetramer assembled from an fluorochrome labeled, oligo-conjugated streptavidin core. Created with BioRender.com

The use of an oligonucleotide tag removes the limitation of fluorochrome spectral overlap or the number of stable isotopes, in flow- and mass-cytometry, respectively. Since the conventional coupling of biotinylated MHC molecules to streptavidin relies on the non-covalent avidin-biotin interaction, there is competition for binding sites on the streptavidin molecule, both for MHC and the DNA oligonucleotide barcode. This results in a balance between the number of MHC molecules to provide sufficient avidity for binding low-frequency antigen-specific T cells, as well as the number of barcodes per tetramer for the detection of the corresponding oligonucleotide signal. On a conventional MHC tetramer, MHC molecules would be occupying all four of the biotin binding sites. If a biotinylated barcode is also attached, there would not be space for the four MHC molecules, and the complex may suffer a reduced avidity or sensitivity. An alternative route of bio-conjugation would be to attach the barcode to streptavidin covalently, thus maintaining all four of the biotin sites for the MHC.

The method utilized for the cellular indexing of transcriptomes and epitopes by sequencing (CITE-seq) technique, previously described by Van Buggenum et al., uses iEDDA-click chemistry to allow specific, directional, and irreversible conjugation of oligonucleotides to protein[1]. For the scope of this thesis, the chemistry will not be provided in detail. However, the chemistry is based on two separate reagents (in short, TCO and Tz) that each possess an NHS ester. The amine-reactive NHS ester on the TCO and Tz reagent is used to label the oligo or protein, respectively. Excess reagent is then filtered off, thereby resulting in a reactive group on both the oligo and protein. Importantly, these two reactive groups are very specific to each other, and the covalent bond is formed in a controlled and directional manner.

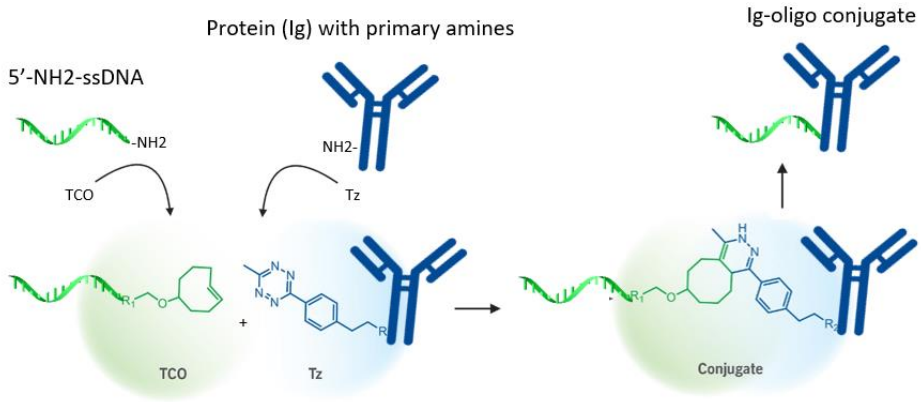


**Figure 2**. Schematic visualization of the mechanism of iEDDA-click chemistry for the conjugation of oligonucleotides to proteins such as immunoglobulins (Ig). In brief, 5' amino-modified single-stranded DNA (ssDNA) oligonucleotides are labeled with TCO and in parallel, primary amine-rich proteins such as Ig or streptavidin are labeled with Tz. The activated biomolecules are then reacted to form a stable protein-oligo conjugate. Modified from[9].

The use of CITE-seq, as an adaptation of conventional fluorescently-labeled antibody staining, has provided an unbiased and high-throughput method for single-cell RNA sequencing (scRNA-seq) for describing heterogeneous cell populations[2]. Whilst bulk analysis of cell subsets was a breakthrough in the late 2000s, whole-transcriptome analysis has reached its capacity for interrogating heterogeneous cell systems, such as antigen-reactive T cells or the immune

contexture of the TME. To obtain phenotypic and functional characteristics of cells more precisely, i.e. cell-specific changes in transcriptome or cellular heterogeneity, analysis on a single-cell resolution may be required. The simultaneous measurement of protein and mRNA expression allows the investigation of the relationship between protein expression and transcript level, to understand further this dynamic interplay.

The RNA expression and protein sequencing assay (REAP-seq) follows a similar principle to CITE-seq, with the use of barcode-labeled antibodies and droplet microfluidics[3]. The use of barcode-labeled antibodies and droplet microfluidics has been incorporated into several commercial platforms i.e. AbSeq® (BD) and TotalSeq ® (BioLegend) for the mapping of immunophenotypes. These systems are then compatible with the widely adopted droplet-based microfluidics platform commercialized by 10x Genomics[4]. Essentially, utilizing poly dT labeled beads for the capture of a polyA tail on the oligonucleotide barcode. However, these approaches require advanced microfluidic systems for single-cell capture and are not yet compatible with conventional flow cytometry. It remains unclear how cellular indexing with barcoded antibodies compares to conventional flow cytometry with fluorochrome-labeled antibodies, for capturing the dynamic range of protein and mRNA expression. Other than barcode-labeled antibodies, a format of oligo-conjugated streptavidin has been commercialized by BioLegend for on-demand MHC tetramer generation and additionally, for coupling to unique biotinylated antibodies that are unavailable in a barcode-labeled format (Bio-Bits® and Flex-T®). All of these technologies have the objective of coupling proteomic analysis with transcriptomic profiling, on a single-cell level, in a single experimental approach. In some cases, it may be to couple cellular protein expression (cell surface markers) with transcript expression of those particular proteins.

In a context more relevant to this thesis, an objective would be to detect antigen-reactive T cells in peripheral blood or tumor biopsies and then further investigate those specific cells, for phenotypic analysis (both on a protein and transcript level). Moreover, there has been a great effort recently to pair information of pMHC recognition with TCR sequencing, on a single-cell basis. In this sense, pMHC recognition on a protein level could be coupled with mRNA sequencing of the corresponding TCR. This would allow further characterization of TCR-pMHC recognition motifs and potentially contribute to the advancement of TCR-based therapeutics.

This work describes a method of generating barcode-labeled fluorescent streptavidin molecules as building blocks for the easy, off-the-shelf generation of MHC tetramers for T cell staining. Potentially, this could provide the capacity to investigate several antigen-reactive T cell populations in a single assay, from one sample. As previously introduced, there are different classes of antigen-reactive T cells, i.e. neoantigen and cancer-germline antigens as well as the viral-derived antigens, which could be interesting to interrogate simultaneously. The study highlights a method for coupling DNA oligonucleotides to streptavidin via click chemistry to generate barcode-labeled molecular cores for assembling MHC tetramers. We apply such a strategy to investigate proof of concept for the generation and use of barcode-labeled MHC-I tetramer reagents for the detection of T cell populations reactive to viral epitopes in healthy donor PBMCs.

## Results and Discussion

### Validation of the experimental workflow in a simplified antibody-oligo system

The preliminary study, in broad terms, consists of an experimental workflow for the conjugation of oligonucleotides to proteins, e.g. immunoglobulins (Ig) or streptavidin (SA), followed by the staining of bulk PBMCs and the isolation of reactive T cells via FACS. The end-point readout of the assay is provided by quantitative PCR (qPCR), whereby the detection of the oligonucleotide (oligo) indicates that firstly the oligo conjugation was successful, secondly, the modification did not disrupt the functionality or binding of the protein, and thirdly, that the oligo was present in sufficient quantities to allow detection. There are however multiple steps in the process that could fail, and hence validation was required along the way.

As an initial test of the click chemistry reagents, as well as to validate that the experimental workflow in a simplified system, the standard CITE-seq protocol was followed to generate antibody (ab)-oligo conjugates for PBMC staining. The antibody of choice here was an anti-human CD3 monoclonal antibody and the oligo was a 75-mer containing a probe binding site to allow quantification. For this initial verification, an unlabeled anti-CD3 was used. Before any cell staining, the antibody-oligo conjugation was validated using a reducing SDS-PAGE (Figure 3A). The SDS-PAGE was run under reducing conditions to allow separation of the antibody heavy (50 kDa) and light chains (25 kDa) so that it was easier to visualize a mobility shift corresponding to the conjugation of oligo (23 kDa). With reference to lanes 2, 3 and 4, a slight shift of the heavy chain band is observed, corresponding to the addition of the Tz reagent (530 Da) on the heavy chain. Lanes 2 and 3 additionally show a distinct band above the heavy chain, corresponding to the conjugation of the oligo. It was apparent that 2µg of ab-oligo conjugate (lane 2) did not produce intense bands, even though the controls (lanes 1, 4 and 5) had the equivalent amount of protein loaded. Hence, there was some protein loss during the filtration steps, whereby excess reagent is de-salted to prevent excessive modification. However, the clear and uniform mobility shift (band at 75 kDa) observed in lane 3, indicated that a substantial fraction of the antibody had been conjugated with an oligo, albeit only on the heavy chain. This may be due to the fewer number and inaccessibility of lysine residues (primary amines) on the light chains. The conjugation is not 100% efficient, considering the band intensity of the unconjugated heavy chain (50 kDa) in lane 3. However, this is fitting, since the chemistry is designed for minimal modification to avoid protein dysfunctionality.

Once the chemical conjugation had been validated, at least in a biochemical manner, separate batches of anti-CD3 (BV421) -oligo were prepared for cell staining. Included among the separate batches was an escalation of the oligo content, ranging from 0.08x to 80x (x: molar excess of oligo). As a reference, the standard CITE-seq protocol suggests a molar ratio of 10x, i.e. (1:10, ab: oligo). Each batch was then used to stain healthy donor PBMCs in separate wells, followed by acquisition and sorting via FACS. From the representative flow plots (Figure 3B) it is apparent that the addition of reagent and oligo, as well as the filtration steps, resulted in a decreased staining capacity for $CD3^+$ cells.

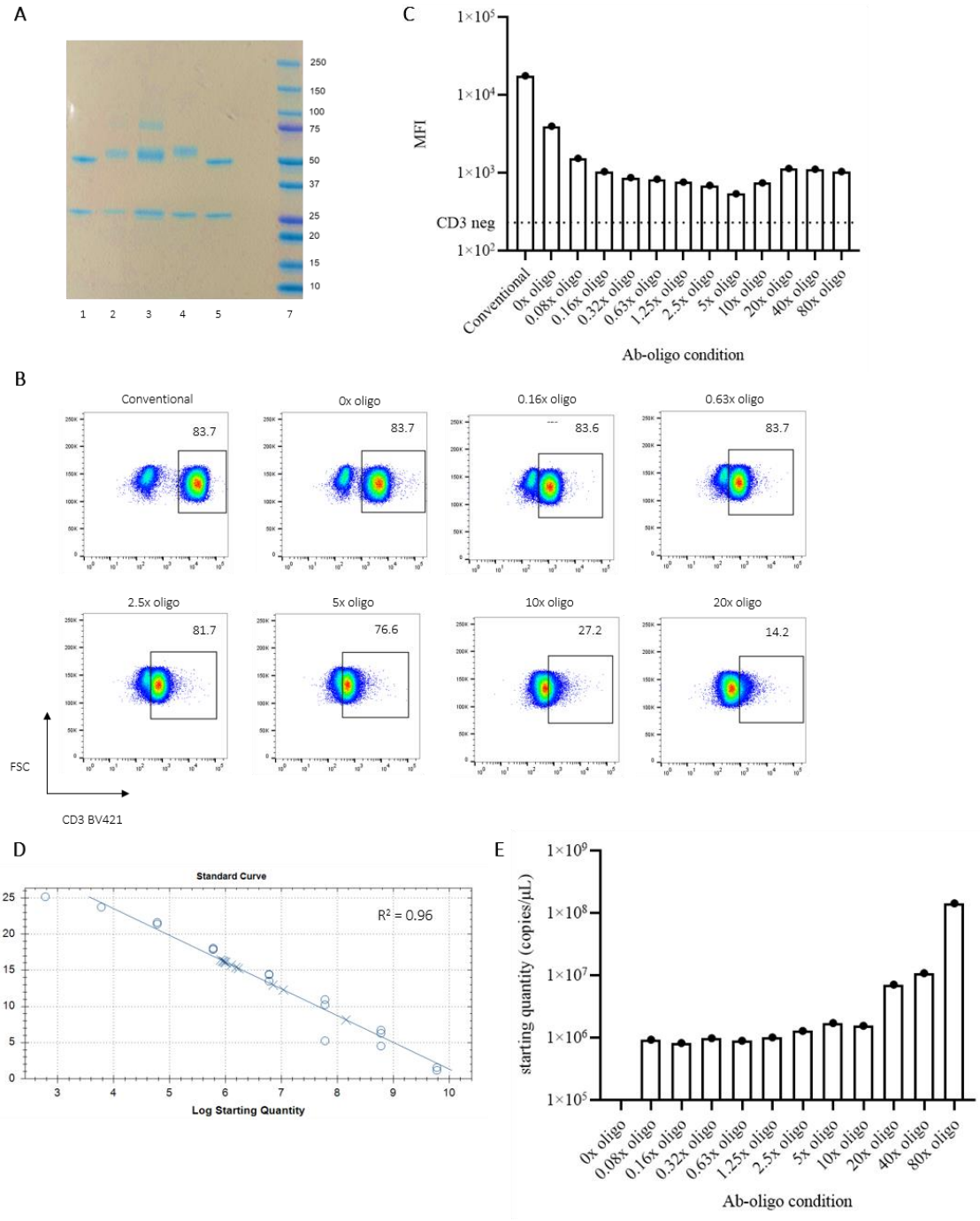


**Figure 3. Verification of the experimental workflow in a simplified antibody-oligo (ab-oligo) system**

**A**, Verification of antibody-oligo conjugation with reducing SDS-PAGE (4-20%). Lanes:1. 2µg Unreacted IgG (1xBBS), 2. 2µg IgG-oligo [10x], 3. 4µg IgG-oligo [10x], 4. 2µg IgG-Tz (-oligo), 5. 2µg IgG unreacted (10% DMSO), 7. MW marker, (x: molar excess of oligo). **B**, Representative FACS plots depicting the anti-CD3 staining of bulk PBMCs with the various ab-oligo conjugates. **C**, Median fluorescence intensity (MFI) values for the corresponding anti-CD3 staining. Dotted horizontal line denotes the MFI of the CD3 negative population. **D**, qPCR standard curve generated for the ssDNA oligo used for the ab-oligo conjugates. **E**, Quantitation of oligo in the FACS samples for the various ab-oligo conditions. (x: molar excess of oligo)

The corresponding median fluorescent intensity (MFI) values (Figure 3C) show this reduction in comparison to a conventional anti-CD3 antibody. The MFI value for the CD3 negative population, denoted as the dotted horizontal line on the plot, indicates that even with a compromised staining capacity, the anti-CD3-oligo conjugates are still able to provide separation in the staining.

After pelleting sorted cells and ab-oligo conjugates, probe-based qPCR was then utilized to detect specifically the oligo in the sorted sample. An oligo standard was run simultaneously, in triplicates, to generate a standard curve (Figure 3D) for the quantitation of oligo in the sorted samples. The correlation coefficient for the oligo standards indicated that the qPCR run was of good quality. It is apparent that, even at the lowest oligo stoichiometry selected (0.08x), the oligo signal can be detected in the sorted samples and there is a tendency for an increased signal detected with the corresponding escalation of oligo stoichiometry (Figure 3E).

**Utilization of barcode-labeled MHC tetramers for the detection of CMV-reactive CD8 T cells**

Once the experimental pipeline had been validated in the ab-oligo setting, the CITE-seq protocol was then adapted for the conjugation of oligo to SA. Similarly, initial verification of the oligo conjugation was done with an unlabeled SA, but this time with an SDS-PAGE in non-reducing conditions (Figure 4A). A reducing agent was not used in this case since the tetrameric form of SA (60 kDa) is not stabilized by disulfide bonds, and thus boiling the samples before running the PAGE was sufficient to separate SA into the monomeric form (15 kDa) to allow easier visualization of a mobility shift. An oligo-only control was included here to rule out any band formation due to free oligo. With reference to lanes 4 – 7, where the oligo has been coupled with an increasing stoichiometry, it is apparent that a mobility shift has occurred resulting in the higher molecular weight bands at 37 kDa. The oligo-SA band (37 kDa) does not seem to intensify with increasing oligo stoichiometry, and again, only a fraction of the protein has been conjugated with oligo. It seems apparent from this that the TCO-oligo is not the limiting reagent; however, it can be assumed that if the Tz modification of SA were increased in the conjugation reaction, more trans–cyclooctene (TCO)-oligo would be able to bind. Again, it was apparent that minimal oligo conjugation was occurring. The faint bands in lanes 2 and 3, at approximately 30 kDa, represent SA in its dimeric form, whereby the boiling of samples before loading the gel was insufficient to fully denature the monomers. This does not influence the outcome here though.

Similarly, once the oligo conjugation was verified biochemically, the unlabeled SA was replaced with either PE- or APC- labeled SA for cell staining purposes. Various batches of PE-SA-oligo or APC-SA-oligo were then prepared in duplicates, representing a range of oligo stoichiometry. These oligo-conjugated, fluorescent SA were then used for the assembly of MHC-I tetramers with a well-characterized CMV-derived epitope. For this particular case, an *in vitro* expanded $CD8^+$ T cell population from a healthy donor PBMC sample, with a known response towards the A0101-restricted CMV-derived epitope, was selected due to the high frequency of viral antigen reactive T cells.

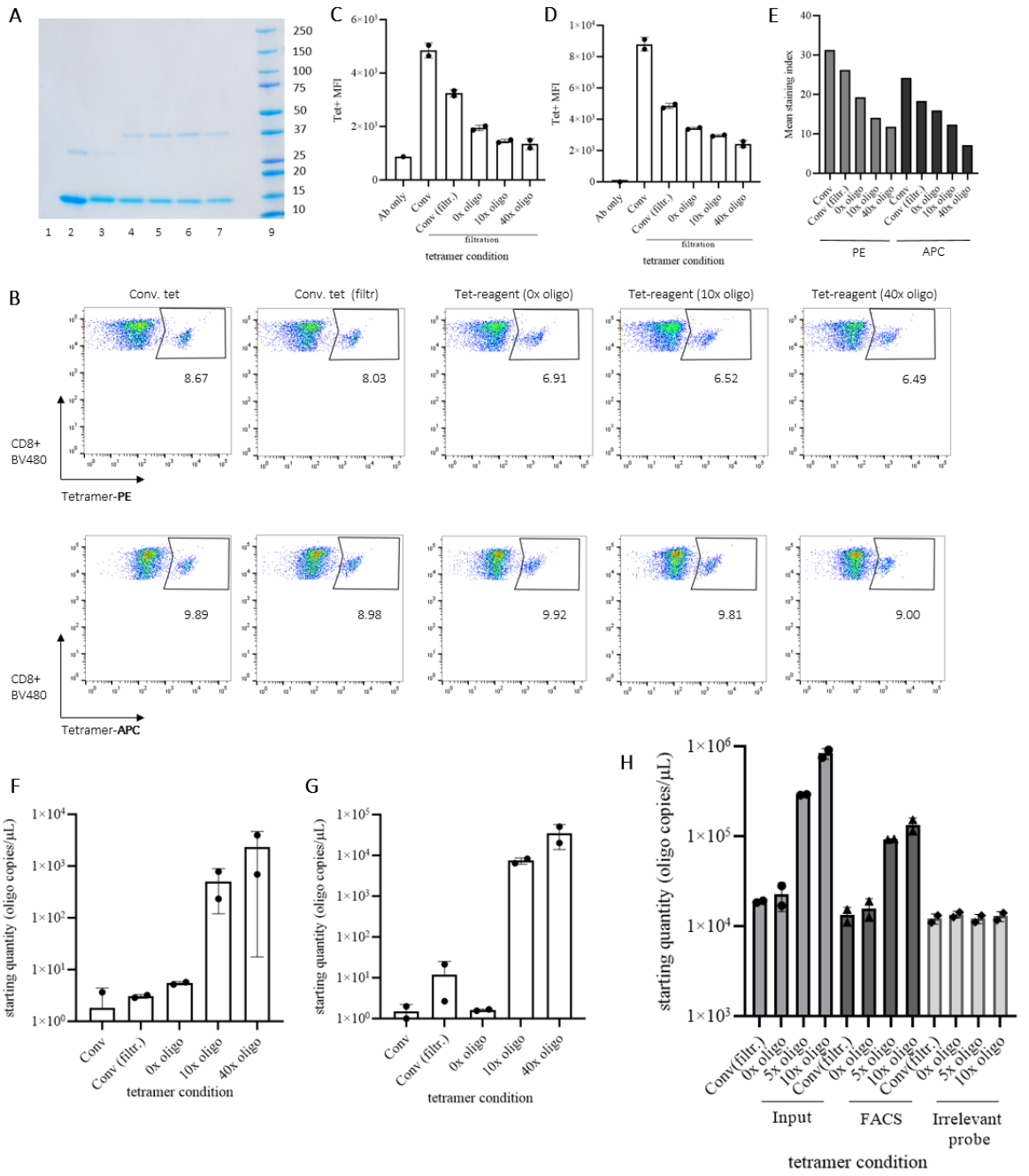


**Figure 4. Utilization of barcode-labeled MHC tetramers for the detection of CMV-reactive CD8+ T cells**

**A,** Verification of streptavidin (SA)-oligo conjugation with non-reducing reducing SDS-PAGE (4-20%) Lanes: 1. 120pmol oligo, 2. SA (1xBBS), 3. SA-Tz, 4. SA-oligo [5x], 5. SA-oligo [10x], 6. SA-oligo [20x], 7. SA-oligo [40x] 9. MW marker· 4ug of SA was loaded for all conditions, (x: molar excess of oligo). **B**, Representative FACS plots depicting tetramer staining of bulk PBMCs (with a 10% spike in of CMV-specific T cells) for the various barcode-tetramer conjugates. **C-D**, Median fluorescence intensity (MFI) values for the corresponding PE barcode-tetramers (n = 2) (C) and APC barcode-tetramers (n = 2) (D). **E**, Mean staining index for PE and APC barcode-tetramers. **F-G**, Quantitation of oligo in the FACS samples for the various PE barcode-tetramers (F) and APC barcode-tetramers (G). **H**, Quantitation of oligo in the staining input and FACS samples, after co-staining with two separate barcode-tetramer batches encoded with two distinct oligos. The irrelevant probe represents the signal obtained from the irrelevant HIV-specific barcode-tetramers. Conv., conventional tetramer; Conv (filtr.), conventional tetramer assembled from a filtered SA. (x: molar excess of oligo).

This specific population of T cells was then spiked into another healthy donor PBMC sample to bulk up the cell numbers so that enough material was available for all of the batches of barcoded tetramers. Representative FACS plots show the detection of the CMV epitope-reactive $CD8^+$ T cells for both PE- and APC-labeled barcoded tetramers (Figure 4B).

The detection of the CMV-positive population was still possible even at the highest oligo stoichiometry, but like the ab-oligo staining, the staining capacity tends to decrease with increasing oligo content. This is also represented as MFI values for PE (Figure 4C) and APC (Figure 4D). This could be due to steric hindrance on the SA molecules, preventing the efficient docking of biotinylated pMHC's and resulting in a decreased tetramer affinity for the T cells. The reduced MFI could be due to oligo conjugation on the PE or APC molecules themselves since these would also contain primary amines. Moreover, it seems that the decrease in MFI cannot be explained just by protein loss due to filtration, since the oligo-SA batches had the equivalent amount of protein. This could have been verified with a protein quantification assay such as a Bradford. A more standardized representation of the staining capacity is provided by the staining index (Figure 4E). This is calculated based on the separation of the positive and negative populations, divided by the spread of the negative population. Although not providing any further information, other than a decrease in staining capacity with the increasing amount of oligo, the staining index is a more comparable value, especially when different fluorochromes are used.

After sorting the PE- and APC- positive populations, respectively, the cell pellets were analyzed by probe-based qPCR. For both PE-labeled (Figure 4F) and APC-labeled (Figure 4G) tetramers, there is a clear distinction in the detected oligo signal when the oligo-conjugated SA's were used for tetramer assembly, and the oligo signal tends to increase correspondingly. In this case, both the tetramer assembly and staining, as well as the qPCR reaction were done in duplicates. This indicates that the oligo remains attached to the tetramers throughout the experimental process and that the oligo is co-isolated with the $tetramer^+$ CD8 T cells and detectable by qPCR.

As a final experiment (Figure 4H), APC-labeled SA was used for similarly generating SA-oligo conjugates as previously. In this setup, however, barcoded tetramer batches of two different pMHC specificities were assembled and encoded by two distinct oligos. One of the batches, same as previous, was the A0101-restricted CMV-derived epitope. The second batch was an irrelevant A0201-restricted HIV-derived epitope. The healthy donor selected for staining, same as previous, was both A0101- and A0201-positive but has not shown any previously reported T cell reactivity towards the HIV-derived epitope. The barcode-tetramer batches were assembled separately, where the CMV-specific tetramers were encoded by an oligo with a FAM probe site, and the HIV-specific, irrelevant tetramers, were encoded by a different oligo with a Quasar670 probe site. The CMV- and HIV-specific tetramers were then pooled, for the respective conditions, and used to co-stain the healthy donor PBMCs. This was done to assess if the oligo signal was detected only when true tetramer-T cell interactions were occurring, and not by chance i.e. oligo non-specifically sticking to cells and resulting in a false positive qPCR signal. In this setup, an additional staining input control was included for each of the tetramer conditions. The staining inputs were kept aside at 4°C and were then diluted at 1:100000 and run alongside the FACS samples in qPCR. A clear increase in the detected oligo signal was observed for the barcode-tetramer conditions, for both the

input and FACS samples (Figure 4H). The signal detected for the inputs were slightly higher, potentially due to insufficient dilution. Compared to the previous experiments, there is a background oligo signal for the oligo-free conditions, denoted by Conv. (filtr.) and 0x oligo. However, this background is equivalent to the signal detected by the irrelevant probe. This indicates that the increased signal detected for the oligo-containing conditions is not a false positive, and additionally, not due to the non-specific amplification of oligo in the qPCR.

In hindsight, an additional confirmatory experiment could be performed to further validate whether the oligo signal detected indeed arises from the specific binding of barcode-tetramers to T cells. This would involve the assembly of two separate barcode-tetramer batches for the CMV-derived epitope, both assembled on APC-SA. One of the batches would be encoded by the oligo with the FAM probe site (oligo-FAM) and the other batch would be encoded by the oligo with the Quasar670 probe site (oligo-q670). The same healthy donor, with known CMV reactivity, would be used again in this setup. The barcode-tetramer batches would be pooled and co-stained, and then the sorted cell/oligo pellet would be used for a multiplexed qPCR reaction, i.e. containing primer-probe sets for both the oligo-FAM and oligo-q670. If a dual signal, for both the FAM and q670 probes, were to be detected, this would imply that there was a specific binding of both the batches of barcode-tetramers to the T cells. This would indicate that the encoding oligos remained attached to the tetramers throughout the experimental workflow, and that signal detected by qPCR was indeed due to a true pMHC-T cell binding event.

This preliminary data indicates that such a chemical conjugation approach could be used to generate oligo-encoded MHC tetramers that are functional in T cell detection but also have encoding capacities. This is a very premature system, however, and further complexity would need to be integrated into the workflow, i.e. use of multiple T cell specificities in a single assay, and further quality assessment would need to be performed. The deconvolution of pMHC specificity with the use of multiple encoding oligos still needs to be assessed. Ideally, the end-point readout would be based on next-generation sequencing, as this would provide a more accurate signal, and would allow the incorporation of a larger range of encoding oligos. This workflow shows promise for a potential strategy of generating libraries of unique SA-oligo conjugates, which could then be stored and used on-demand for the assembly of barcoded tetramers for antigen-specific T cell detection. The commercial availability of various fluorescent SA's, as well as encoding oligos and the reagent kits, would promote the feasibility and utility of such a strategy. As an end-goal application, the encoding oligo system could be adapted to be compatible with various single-cell sequencing platforms to allow the pairing of pMHC specificity with TCR recognition.

## Materials & Methods

### Healthy donor samples

Healthy donor blood samples were obtained from the blood bank at Rigshospitalet, Copenhagen, Denmark. PBMCs were isolated from whole blood as described for the PBMCs from the patients and cryopreserved at -150°C in fetal calf serum (FCS, Gibco) + 10% dimethyl sulfoxide (DMSO, Sigma-Aldrich). All healthy donor and patient materials were collected under approval by the Scientific Ethics Committee of the Capital Region, Denmark, with written informed consent obtained according to the Declaration of Helsinki.

### Generation of oligonucleotide-labeled streptavidin for MHC tetramerization

Oligonucleotide-labeled streptavidin conjugates were prepared via covalent and irreversible conjugation by iEDDA-click chemistry, as previously described in Van Buggenum et al. 2016[1] for antibody-oligo conjugation.

### TCO-oligonucleotide labeling

In Brief, 35 nmol amino-modified 75-mer single-stranded DNA (ssDNA) oligonucleotide (LGC Biosearch Technologies) in nuclease-free H2O was incubated for 30 min in 100 mM TCO-PEG4-NHS (Click Chemistry Tools) in DMSO and 10x borate buffered saline (BBS), with the sequential addition of TCO-PEG4-NHS every 15 mins. After quenching residual NHS groups with 1 M Glycine pH 8.5 for 5 min at room temperature, TCO-labeled oligonucleotide was desalted with Micro Bio-Spin P-6 columns (Bio-Rad) in 1xBBS, according to manufacturer's instructions. The concentration of TCO-labeled oligonucleotide was determined via NanoDrop and adjusted to 100 µM with 1x BBS for storage at -20°C.

### Tetrazine (Tz)-Streptavidin labeling

For initial verification and SDS-PAGE analysis, purified Streptavidin Plus recombinant [SA26] (Agilent/ProZyme) at 1 mg/mL was buffer exchanged using Micro Bio-Spin P-6 columns (Bio-Rad) in 1xBBS. For PBMC staining, PE or APC streptavidin (1 mg/mL, BioLegend) was likewise exchanged in 1x BBS. Streptavidin was then incubated with 2 mM Tz-PEG4-NHS for 30 min at room temperature. After quenching residual NHS groups with 1 M Glycine pH 8.5 for 5 min at room temperature, Tz-streptavidin was desalted using Micro Bio-Spin P-6 columns (Bio-Rad) in 1xBBS.

### Oligonucleotide-streptavidin conjugation

The conjugation reaction was set up with 30 pmol of 100 µM TCO-oligonucleotide per 1 µg mTz-streptavidin and allowed to proceed overnight at room temperature. 10 mM TCO-PEG4-GLY was prepared by incubating 100 mM TCO-PEG4-NHS and 1 M glycine pH 8.5 in H2O, for 1h at room temperature and stored at -20°C. After completion of the oligo-streptavidin conjugation reaction, residual tetrazine sites on Streptavidin were quenched with 10 mM TCO-PEG4-GLY. For verification of successful conjugation, 2 µg of labeled and quenched streptavidin-oligo was run on a non-reducing SDS-PAGE (200V, 400 mA, 35 min), followed by staining with Coomassie Brilliant Blue (Bio-Rad) for band protein visualization. Following verification, streptavidin-oligo

was adjusted to a concentration of 0.5 mg/mL in PBS containing 0.06% Sodium Azide (Sigma Aldrich).

**MHC monomer production and generation of specific peptide-MHC complexes**

The production of MHC monomers was performed as previously described[5,6]. In brief, human $\beta_2$ microglobulin ($\beta_2$m) light chain and the heavy chains of the included HLA types were expressed in bacterial Bl21 (DE3) pLysS strain (Novagen, cat#69451) and purified as inclusion bodies. Followed by folding of heavy chain and β2m light chain complexes with a UV-sensitive ligand[7,8], biotinylation with BirA biotin-protein ligase standard reaction kit (Avidity, 318 LLC-Aurora, Colorado), and purification using size-exclusion column (Waters, BioSuite125, 13µm SEC 21.5 × 300 mm) HPLC (Waters 2489). Specific pMHC complexes were generated by UV-induced peptide exchange[5,7].

**Assembly of barcode-labeled pMHC tetramers and PBMC staining**

Following UV exchange and peptide loading, pMHC complexes were centrifuged at 3300 g, 4°C for 5 min and the supernatant was transferred to a new plate. Fluorescently labeled oligonucleotide-streptavidin conjugates (PE, APC) were then added stepwise to the pMHC complexes. After a cumulative 30 min of incubation on ice, the oligo-labeled MHC tetramers (10ug/mL final concentration) were formulated with 0.02% NaN3 for storage at 4°C. Cryopreserved PBMCs from healthy donors were thawed and seeded at a maximum of 2E6 cells per well in 96-well plates and incubated with dasatinib at a final concentration of 50 nM for 30 min at 37°C. The oligo-labeled MHC tetramers were centrifuged at 3300 g, 4°C for 5 min to pellet unwanted aggregates, followed by the staining of PBMCs for 15 min at 37°C. Without washing, the PBMCs were then stained with an antibody mix composed of CD8-BV480 (BD, cat#566121, clone RPA-T8), dump channel antibodies (CD4-FITC (BD, cat#345768), CD14-FITC (BD, cat#345784), CD19-FITC (BD, cat#345776), CD40-FITC (Serotech, cat#MCA1590F), and CD16-FITC (BD, cat#335035)) and a dead cell marker (LIVE/DEAD Fixable Near-IR; Invitrogen, cat#L10119). Tetramer-binding T cells were sorted as lymphocytes, single, live, $CD8^+$, $FITC^-$ and $PE^+$ and subsequently pelleted by centrifugation at 5000 g, 4°C for 10 min. The resulting cell/barcode pellet was then stored at -20°C for qPCR analysis.

**Flow cytometry**

All flow cytometry experiments were carried out on a FACSMelody instrument (BD Biosciences). Data were analyzed in FlowJo version 10.7.1 (TreeStar, Inc).

**Quantitative PCR**

Sorted cell/oligo pellets were mixed with oligo-specific forward primer [250 nM], reverse primer [250 nM], and a FAM-labeled probe [200 nM] in 2x SsoAdvanced Universal probes Supermix (Bio-Rad) and run for 40 cycles on a CFX96 Real-Time PCR detection system (Bio-Rad) with subsequent analysis using Bio-rad CFX Manager. For the irrelevant pMHC control barcode-tetramers, a second oligo was used with its own primer-probe set. The probe for this irrelevant oligo was labeled with Quasar 670.

## References


1. Van Buggenum, J. A. G. L. *et al.* A covalent and cleavable antibody-DNA conjugation strategy for sensitive protein detection via immuno-PCR. *Sci. Rep.* **6**, 1–12 (2016).
2. Stoeckius, M. *et al.* Simultaneous epitope and transcriptome measurement in single cells. *Nat. Methods* **14**, 865–868 (2017).
3. Peterson, V. M. *et al.* Multiplexed quantification of proteins and transcripts in single cells. *Nat. Biotechnol.* **35**, 936–939 (2017).
4. Zheng, G. X. Y. *et al.* Massively parallel digital transcriptional profiling of single cells. *Nat. Commun.* **8**, (2017).
5. Rodenko, B. *et al.* Generation of peptide-MHC class I complexes through UV-mediated ligand exchange. *Nat. Protoc.* **1**, 1120–32 (2006).
6. Hadrup, S. R. *et al.* High-Throughput T-Cell Epitope Discovery Through MHC Peptide Exchange. in *Methods in Molecular Biology* vol. 524 383–405 (2009).
7. Toebes, M. *et al.* Design and use of conditional MHC class I ligands. *Nat. Med.* **12**, 246–251 (2006).
8. Bakker, A. H. *et al.* Conditional MHC class I ligands and peptide exchange technology for the human MHC gene products HLA-A1, -A3, -A11, and -B7. *Proc. Natl. Acad. Sci.* **105**, 3825–3830 (2008).
9. TCO – Tetrazine Ligation | Click Chemistry Tools. https://clickchemistrytools.com/tco-tetrazine-ligation/.

# 6 ADDITIONAL RESULTS II

## Molecular encoding of mRNA nanocarriers for optimizing the delivery of therapeutic cargo

### Introduction

#### Applications of mRNA-NP therapeutics in the clinic

The use of nanoparticle (NP) delivery systems has greatly advanced the clinical utility of nucleic acid-based therapies over recent years, bringing previously un-druggable agents to patients by facilitating new therapeutic strategies. A recent highlight in the realm of NP-based mRNA delivery is showcased by the Pfizer-BioNTech COVID-19 vaccine (BNT162b2)[1], which is a lipid nanoparticle (LNP) - based mRNA vaccine. In the context of cancer, NPs have facilitated the re-emergence of the concept of therapeutic cancer vaccination. Since the observation that the systemic delivery of mRNA encoding for vaccine antigens was able to induce strong effector and memory T cell responses[2], it is becoming increasingly evident that therapeutic cancer vaccines are a resurging avenue to provide synergy with existing immunotherapies such as immune checkpoint blockade[3]. The molecular nature of mRNA allows its utility as cargo for both immunogenic and non-immunogenic purposes. The single-stranded RNA structure, as well as the presence of specific motifs, provides adjuvant effects for vaccine strategies[4]. On the other hand, advancements in synthesis routes, e.g. with the use of *in vitro* transcription[5], and subsequent modification of the mRNA molecules, have enabled the use of mRNA in non-immunogenic applications such as chimeric antigen receptor- or TCR-based therapies[6].

#### Screening for effective LNP-based delivery systems

The use of LNPs is now considered one of the primary delivery mechanisms for RNA-based therapeutics. One of the principal components of LNP formulations is cationic lipids, due to their inherent ability to encapsulate negatively charged molecules such as DNA or RNA. This encapsulation provides stability for such molecules whilst in circulation, but also provides a means of cell entry and endosomal escape by membrane fusion[7]. The high positive surface charge of cationic LNPs, however, results in substantial cytotoxicity, e.g. inflammation and more severe cases, cytokine release syndrome[8]. Generally, LNPs undergo rapid clearance by the liver following systemic delivery, which limits the therapeutic efficacy substantially. Consequently, much effort over the decades has resulted in the emergence of a vast variety of lipids and lipid-like molecules to reduce the associated cytotoxicity and improve therapeutic efficacy. This has resulted in an enormous combinatorial chemical space that represents all the potential materials that be used in LNP formulations. This makes the screening for optimal parameters extremely laborious, as generally, lipid components are systematically evaluated through a one-factor-at-a-time technique[9]. However, novel strategies have recently been approached to facilitate the simultaneous assessment of LNP delivery to cells both in an *in vitro* and *in vivo* setting[10,11].

These approaches, based on the inclusion of DNA barcodes in the LNP design, have provided a means of molecular encoding and have facilitated the screening for effective delivery formulations in a high-throughput manner.

## Results and Discussion

This dataset consists of preliminary experiments to assess LNP -mediated transfection of mRNA in a tumor cell line and bulk PBMCs, *in vitro*. A reporter mRNA encoding for enhanced green fluorescent protein (herein referred to as GFP) has been used as a model mRNA cargo, enabling the quantification of mRNA transfection in cells via flow cytometry. The lipid nanoparticles utilized consisted of a commercial mRNA transfection reagent (referred to as LFN MMAX) as well as various cationic LNP formulations prepared in-house with commercially available lipid materials. This early experimental work aimed at exploring conditions for LNP-mediated mRNA transfection *in vitro*, with the end objective of incorporating DNA barcodes as encoding elements into the LNP formulation.

**GFP mRNA transfection of K562 cell line with a small library of lipid nanoparticles reveals high transfection efficiency but substantial cytotoxicity**

Considering the enormous chemical space of the constituents that can potentially be used for LNP formulation, as highlighted in the introductory section, a small but diverse library of LNPs were individually formulated with GFP mRNA and used to transfect an immortalized myelogenous leukemia cell line (K562) *in vitro*. After 24 h transfection in cell culture media, the K562 cells were stained with a Live/dead cell marker, without fixation, and acquired on the flow cytometer. A representative gating strategy for the quantification of GFP mRNA transfection in K562 cells is given in Figure 1A. Four representative GFP plots are given for a selection of LNP candidates. LFN MMAX, the commercial reagent, was used throughout the experiments, as a positive control for mRNA transfection, and showed a robust transfection efficiency of 11%. The other candidates showed a range of transfection efficiencies from 0.17% (2200) to 98.1% (1003). The transfection efficiency values are summarized for all the tested formulation in Figure 1B (represented by % $GFP^+$). An untransfected control, i.e. kept under the same culturing conditions, was included in every experimental setup to assess for any background autofluorescence. It may be appreciated from the summary of the transfection efficiencies that many of the in-house assembled LNP formulations seem to result in a larger fraction of $GFP^+$ K562 cells in comparison to LFN MMAX. This was the case at least in terms of the frequency of $GFP^+$ cells. When assessing the median fluorescence intensity (MFI) of the $GFP^+$ cells, it is apparent that LFN MMAX was still the most efficient LNP formulation in terms of GFP protein expression (Figure 1C). Moreover, when evaluating the viability of the K562 cells after 24 h transfection with the LNPs, it was very apparent that the majority of the in-house assembled formulations were associated with severe cytotoxicity, compared to LFN MMAX and the untransfected control.

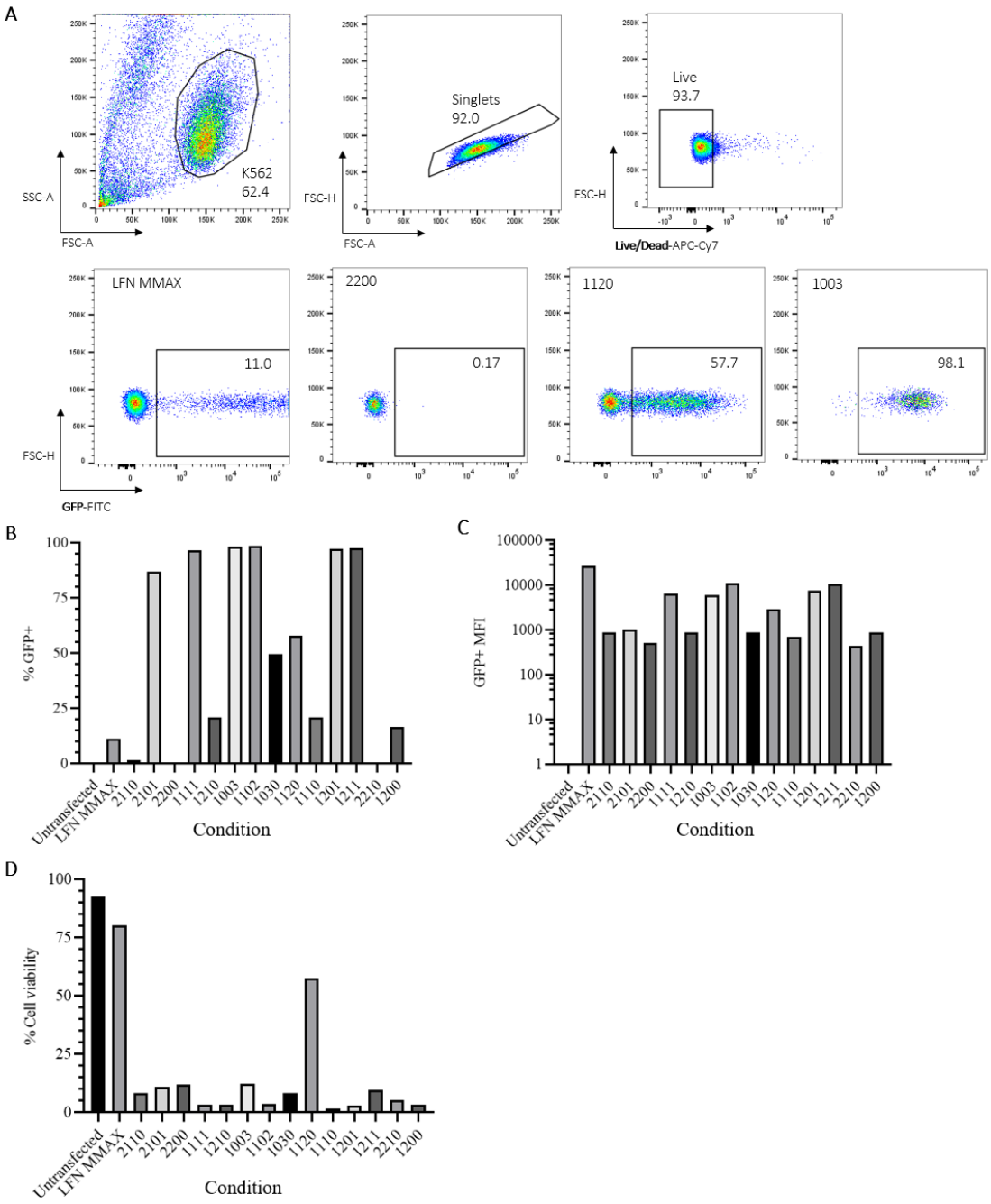


**Figure 1. GFP mRNA transfection of K562 cell line with a small library of lipid nanoparticles reveals high transfection efficiency but substantial cytotoxicity**

**A**, Representative gating strategy for the measurement of GFP expression in K562 cell line after 24 h incubation with GFP mRNA lipid nanoparticles composed of DOTAP, DOPE, cholesterol and COASTSOME in various molar ratios. Gated on K562, singlets and live. A commercial mRNA transfection reagent (LFN MMAX) was used for comparison. **B,** Frequency of GFP+, live K562 cells after 24 h transfection with various mRNA lipid nanoparticle formulations. **C,** Median fluorescence intensity (MFI) of GFP+, live K562 cells after 24 h transfection with various mRNA lipid nanoparticle formulations. **D,** Cell viability of K562 cells After 24 h transfection with various mRNA lipid nanoparticle formulations.

From this initial experiment, it appears that despite the in-house formulation's capacity to induce uptake of GFP mRNA in K562 cells, the corresponding MFI values indicate that GFP mRNA is not as efficiently translated into protein within the cells. This relates to the phenomena of endosomal escape, as previously introduced. The proprietary components within the LFN MMAX formulation have been optimized for enhancing endosomal escape, as this has been a bottleneck in the field. Additionally, the in-house LNP formulations demonstrated severe cytotoxicity under these transfection conditions. In hindsight, however, considering the nature of the amine-reactive dye used as the Live/Dead marker, this would label cells as dead or transitioning to death just from the process of lipid-mediated transfection. The membrane fusion events leading to uptake of the LNPs may also result in the cell entry of the Live/Dead marker. Implying that these transfected cells that display "cytotoxicity" may not actually be dead cells and that alternative apoptotic markers could be utilized instead, e.g. Annexin V and propidium iodide staining, which more accurately label apoptotic cells.

**GFP intracellular staining confirms mRNA transfection and true GFP protein expression in K562 cells**

As a follow-up experiment, to assess any auto-fluorescence-induced false-positive GFP signal, K562 cells were stained with α-GFP antibody after 24 h transfection with GFP LNPs formulated with LFN MMAX (Figure 2A). This was performed to verify that the GFP signal detected in K562 cells with flow cytometry was not an artifact of cellular autofluorescence, which has been a phenomenon associated with the use of transfection reagents[12]. Representative GFP/ α-GFP flow plots, pre-gated on K562 cells, singlets and live cells, are given in Figure 2A, where the frequency of either GFP single-positive or GFP/ α-GFP double-positive cells has been denoted in the plots. It is apparent from the untransfected and free lipid controls, that there is no false GFP signal due to autofluorescence. The GFP transfected sample shows a signal only in the GFP (FITC) channel. In the transfected samples stained with α-GFP (in triplicates), it is apparent that the majority of the $GFP^+$ cells were also α-$GFP^+$, which confirms the GFP signal as a true measurement of GFP protein expression in the cells. The transfection efficiencies in this experiment were not as high as previously demonstrated with LFN MMAX, potentially due to the harsh nature of the intracellular staining kit used. Fixative agents in such staining kits are typically quite destructive for fluorescent proteins. Additionally, the permeabilization process may result in leakage of GFP protein out of the cells.

A

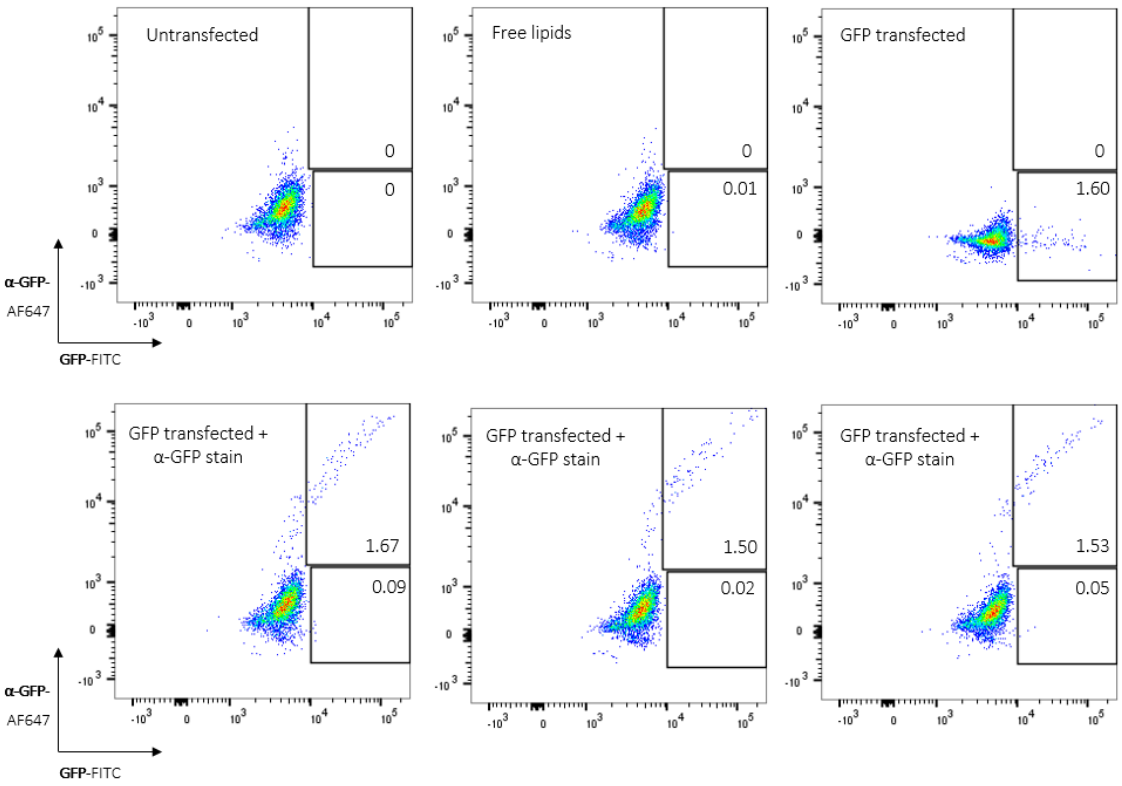


**Figure 2. GFP intracellular staining confirms mRNA transfection and true GFP protein expression in K562 cells**
**A**, K562 cells, pre-gated on singlets and live after 24 h transfection with commercial transfection reagent LFN MMAX. followed by GFP intracellular staining ,in triplicates. Untransfected and free lipid controls were included.

## Optimization of GFP mRNA transfection in bulk PBMCs shows a dose-effect on the transfection of CD8$^+$ T cells

As it was apparent that LNP-mediated mRNA transfection was possible in a leukemia cell line, transfection conditions were then assessed in a primary cell system that is typically "hard-to-transfect"[13]. In line with this, PBMCs from a healthy donor were utilized and transfection was assessed in the CD3$^-$, CD3$^+$ or CD3$^+$/CD8$^+$ compartments. A representative gating strategy for the assessment of GFP expression in these broad subsets is provided in Figure 3A. This experimental setup compared two distinct LNP formulations, LFN MMAX and the in-house assembled "1120" formulation, that was assessed in Figure 1. Instead of varying the lipid components, this time the final concentration of lipid reagents in the transfection condition was varied. This final concentration was adapted based on the findings from Figure 1. Since the concentration of the LFN MMAX reagent is not given by the supplier, the concentration is denoted by x, e.g. 1x is the recommended dose in a 24-well plate format. The cell viability, out of total singlets, for the various transfection conditions, is given in Figure 3B. The increasing amount of LFN MMAX reagent does not appear to be associated with more cytotoxicity, whereas, there is a substantial degree of cytotoxicity associated with the 1120 formulation (referred to as lipoplex). However, even at the highest concentration tested in this setup (40 µM),

a viability of approximately 75% was observed, which was a substantial improvement from the initial tests in K562. The transfection efficiency, i.e. GFP expression, is given for the $CD3^-$, $CD3^+$ or $CD3^+/CD8^+$ compartments (Figure 3C-E). For both LFN MMAX and the in-house assembled 1120 formulations, an apparent dose-effect was observed for the increasing lipid concentrations, in all three of the compartments. Importantly, the amount of GFP mRNA was kept constant between the conditions, so this implies a direct effect of increased mRNA uptake due to the use of more cationic lipid components. This experiment provides an initial verification that mRNA transfection of T cells, in a heterogeneous cell system, is indeed possible. However, further optimization of the lipid components in the formulations would need to be performed to achieve a more efficient transfection, with reduced cytotoxicity, in primary cells *in vitro*.

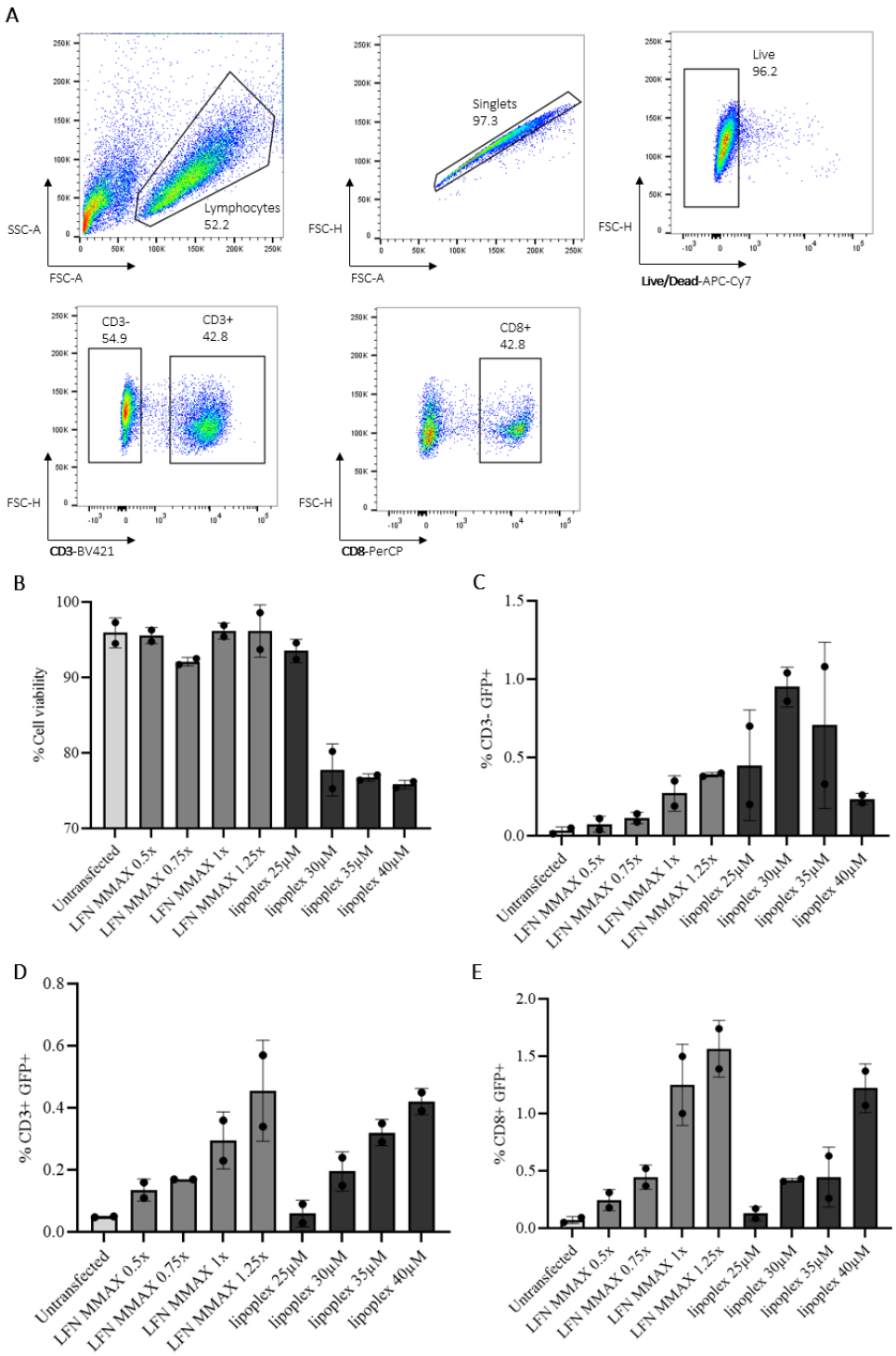


**Figure 3. Optimization of GFP mRNA transfection in bulk PBMCs shows a dose-effect on the transfection of CD8+ T cells**

**A**, Representative gating strategy for assessing GFP mRNA transfection in bulk PBMCs from a healthy donor after 24 h transfection with commercial transfection reagent LFN MMAX and DOTAP/DOPE/Cholesterol lipid nanoparticles (formulation 1120, i.e. lipoplexes) at various concentrations. For LFN MMAX, the recommended dose is 1x. The lipid concentration refers to the final concentration of lipids in the culture media. **B,** Cell viability of K562 cells After 24 h transfection with various mRNA lipid nanoparticle formulations. **C-E**, Frequency of $CD3^-$ $GFP^+$ (C) $CD3^+$ $GFP^+$ (D) and $CD8^+$ $GFP^+$ after 24 h transfection with various mRNA lipid nanoparticle formulations.

**Co-transfection of GFP mRNA and ssDNA barcode in a preliminary attempt to encode lipid nanoparticles**

All of this experimental workflow was done with the final objective in mind of developing a screening platform for LNPs based on molecular encoding, to provide a method of assessing functional delivery of mRNA cargos to cells *in vivo*, in a high-throughput manner. However, due to practical constraints, this objective was not feasible. Rather, preliminary proof of concept for the co-delivery of mRNA and DNA barcode to cells was assessed *in vitro*. The workflow here consisted of the co-encapsulation of GFP mRNA with a single-stranded DNA (ssDNA) oligonucleotide "barcode", followed by the transfection of K562 cells and then sorting of $GFP^+$ and $GFP^-$ cells via FACS. End-point quantification of the co-delivered DNA barcode was provided by probe-based quantitative PCR (qPCR). This setup was shifted back to the K562 setting, since this cell line showed more robust GFP transfection, especially considering a substantial quantity of $GFP^+$ cells would be required for the post-sort qPCR analysis. A representative gating strategy for the sorting of $GFP^-$ or $GFP^+$ K562 cells, with the use of either LFN MMAX or the in-house assembled 1120 formulation, is given in Figure 4A. The sort gates, indicated in the plots, were placed so that there was a substantial separation of the $GFP^-$ and $GFP^+$ populations. It is apparent in figure 1A that LFN MMAX, again, resulted in a more efficient expression of GFP protein. The 1120 in-house formulation did not perform as well as previously. However, there was still sufficient GFP transfection in either condition to allow for sorting of 3000 $GFP^+$ cells. After sorting, the cells were pelleted by centrifugation and analyzed by probe-based qPCR. The oligo co-encapsulated with the mRNA contained a FAM-probe site, allowing such quantitation. LNP-GFP (-oligo) was also included in the setup as controls. The results from the qPCR quantitation are summarized in Figure 4B. From this preliminary experiment, it appears that there is no difference in the detected barcode signal between $GFP^-$ and $GFP^+$ cells. There is however a clear increase in barcode signal in the +oligo conditions. This could imply that there is preferential uptake of barcode-LNPs by the cells and not GFP-barcode-LNPs. It could also infer that despite GFP-barcode-LNP uptake, GFP may not be efficiently expressed in those cells within the timeframe. Further speculation could also infer that potentially the GFP-barcode-LNPs may be sticking to the surface of the cells, thereby preventing the translation of GFP protein in the cytoplasm. A final, unfavorable, speculation could be that free DNA barcode is just sticking to the surface of the cells, thereby being co-isolated with the cells and resulting in the signal detectable by qPCR. However, this is quite unlikely due to the nature of how cells are sorted by FACS. This very preliminary experiment shows that there is not an observed correlation between GFP expression and barcode signal, and as such, currently the barcode cannot be used to monitor protein expression.

A

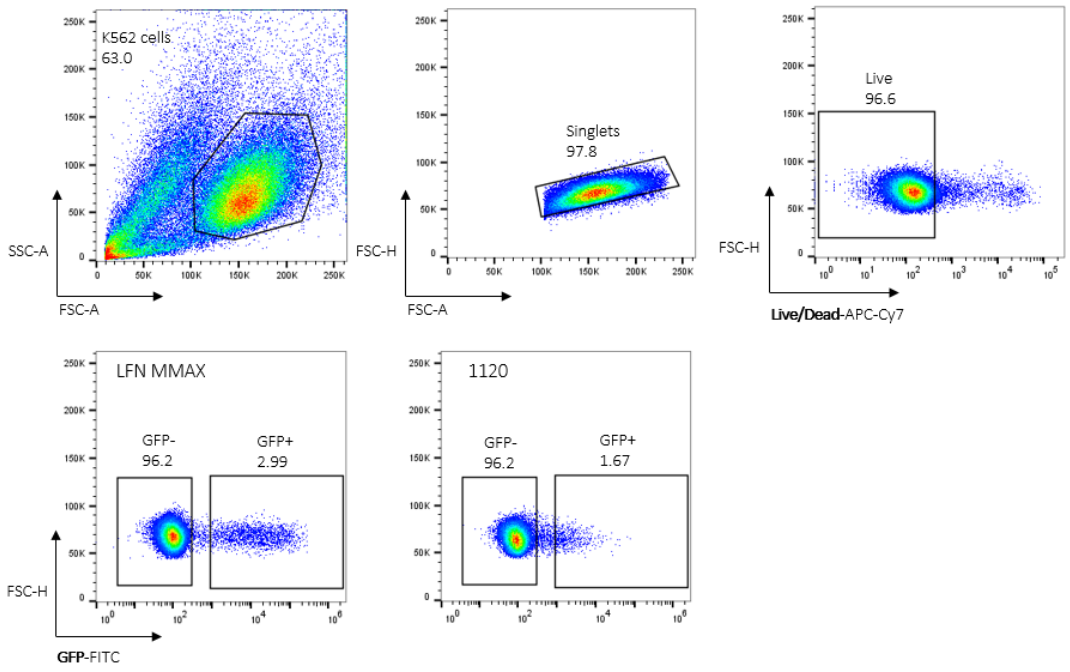


B

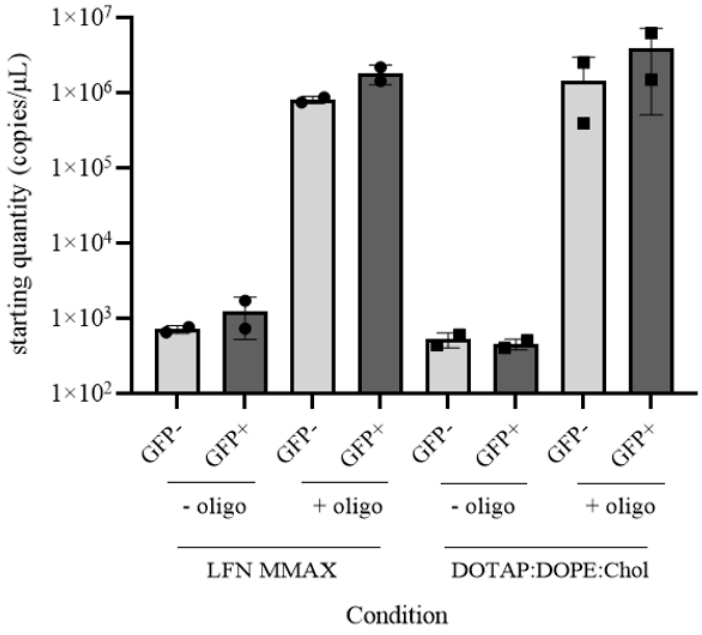


**Figure 4. Co-transfection of GFP mRNA and ssDNA barcode in a preliminary attempt to encode lipid nanoparticles**

**A**, Representative gating strategy for assessing GFP expression in K562 cell line after 24 h transfection with GFP mRNA/single-stranded DNA (ssDNA) lipid nanoparticles (LNPs), i.e. barcoded nanoparticles. Using either commercial LFN MMAX reagent or DOTAP/DOPE/Cholesterol (1120) LNPs.

**B**, Probe-based qPCR quantification of ssDNA barcode after sorting $GFP^+$ or $GFP^-$ K562 cells. The ssDNA barcode has a FAM probe site for quantification.

## Methods and Materials

### Cell line and culturing

The chronic myelogenous leukemia cell line (K562 (CCL.243)) was purchased from ATCC, cultured and expanded in 75 $cm^2$ flasks containing RPMI with 10% FCS and 1% Penicillin-streptomycin (R10 media). Cells were then cryopreserved at a density of $1x10^6$ cells/mL in FCS containing 10% DMSO and stored at -180°C. Before transfection experiments, K562 cells were thawed and washed in R10 media and then cultured in 75 $cm^2$ flasks containing R10 media. K562 cells were allowed to settle and expand for at least 2-3 days before transfection. For transfection, K562 cells were seeded at $1\text{-}5x10^6$ cells/mL in 96-well or 24-well culture plates. All culturing was done at 37°C with 5% CO2.

### Healthy donor samples

Healthy donor blood samples were obtained from the blood bank at Rigshospitalet, Copenhagen, Denmark. PBMCs were isolated from whole blood as described for the PBMCs from the patients and cryopreserved at -150°C in fetal calf serum (FCS, Gibco) + 10% dimethyl sulfoxide (DMSO, Sigma-Aldrich). All healthy donor and patient materials were collected under approval by the Scientific Ethics Committee of the Capital Region, Denmark, with written informed consent obtained according to the Declaration of Helsinki. Before transfection, bulk PBMCs were thawed and washed in R10 media, followed by transfer into 24-well or 96-well culture plates, containing X-VIVO 15 media with 5% human serum and 100U/mL IL-2. All culturing was done at 37°C with 5% CO2.

### Lipid nanoparticle preparation

CleanCap EGFP mRNA (5-methoxyuridine) was purchased from TriLink Biotechnologies, resolved to 1 mg/mL in nuclease-free water and 1x-use aliquots were prepared and stored at -20°C. Lipofectamine MessengerMAX (LFN MMAX) was purchased from ThermoFisher and stored at 4°C. DOTAP (COATSOME® CL-8181TA), DOPE (COATSOME ME-8181) and COATSOME (SS-33/4PE-15) were purchased from NOF America, cholesterol (C3045-5G) was purchased from SigmaAldrich. Lipids were resolved in ethanol at 10 mM and stored at -20°C. For lipid nanoparticle assembly, lipids in ethanol (1 mM) were mixed with EGFP mRNA (0.1 mg/mL) in serum-free RPMI, briefly vortexed and allowed to assemble at room temperature for 5 min. For LFN MMAX, the supplier's recommendation was followed. In brief, 0.5 µg mRNA in 25µL RMPI was mixed with 1 µL of LFN MMAX in 25µL RMPI and allowed to complex for 5 min at room temperature. The LNP-mRNA complexes were then directed administered to cells and given a 24 h transfection at 37°C with 5% CO2. For mRNA-DNA co-transfection, mRNA (0.1 mg/mL) was pre-mixed with ssDNA (10 µM) at a 10:1 mass ratio (mRNA:DNA) in serum-free RPMI, before mixing with lipids in ethanol (1 mM).

## Cell staining and Flow cytometry

After transfection, K562 cells were washed in PBS containing 10% FCS (FACS buffer) and stained with a dead cell marker (LIVE/DEAD Fixable Near-IR; Invitrogen, cat#L10119). For GFP intracellular staining, Alexa Fluor 647 mouse α-GFP (BD, cat. #565197, clone 1A12-6-18) was used with the eBioscience Intracellular Fixation & Permeabilization buffer set (cat. # 88-8824-00). For PBMC staining, antibody mix containing CD3-BV421 (BD, cat. # 562426, clone UCTH1), CD8-PerCP (Invitrogen, cat. # MHCD0831, clone 3B5) and dead cell marker (LIVE/DEAD Fixable Near-IR; Invitrogen, cat#L10119). All flow cytometry experiments were carried out either a FACSCanto or FACSMelody instrument (BD Biosciences). Data were analyzed in FlowJo version 10.7.1 (TreeStar, Inc).

## Quantitative PCR

Sorted cell/oligo pellets were mixed with oligo-specific forward primer [250 nM], reverse primer [250 nM], and a FAM-labeled probe [200 nM] in 2x SsoAdvanced Universal probes Supermix (Bio-Rad) and run for 40 cycles on a CFX96 Real-Time PCR detection system (Bio-Rad) with subsequent analysis using Bio-rad CFX Manager.

## References


1. Sahin, U. *et al.* COVID-19 vaccine BNT162b1 elicits human antibody and TH1 T cell responses. *Nature* **586**, 594–599 (2020).

2. Kranz, L. M. *et al.* Systemic RNA delivery to dendritic cells exploits antiviral defence for cancer immunotherapy. *Nature* **534**, 396–401 (2016).

3. Saxena, M., van der Burg, S. H., Melief, C. J. M. & Bhardwaj, N. Therapeutic cancer vaccines. *Nat. Rev. Cancer* **909**, 139–167 (2021).

4. Pastor, F. *et al.* An rna toolbox for cancer immunotherapy. *Nat. Rev. Drug Discov.* **17**, 751–767 (2018).

5. Devoldere, J. *et al.* Evading innate immunity in nonviral mRNA delivery: Don't shoot the messenger. *Drug Discov. Today* **116**, 11–25 (2016).

6. Parayath, N. N., Stephan, S. B., Koehne, A. L., Nelson, P. S. & Stephan, M. T. In vitro-transcribed antigen receptor mRNA nanocarriers for transient expression in circulating T cells in vivo. *Nat. Commun.* **11**, (2020).

7. Stewart, M. P., Lorenz, A., Dahlman, J. & Sahay, G. Challenges in carrier-mediated intracellular delivery: Moving beyond endosomal barriers. *Wiley Interdiscip. Rev. Nanomedicine Nanobiotechnology* **8**, 465–478 (2016).

8. Elsabahy, M. & Wooley, K. L. Cytokines as biomarkers of nanoparticle immunotoxicity. *Chem. Soc. Rev.* **42**, 5552 (2013).

9. Kauffman, K. J. *et al.* Optimization of Lipid Nanoparticle Formulations for mRNA Delivery in Vivo with Fractional Factorial and Definitive Screening Designs. *Nano Lett.* **15**, 7300–7306 (2015).

10. Dahlman, J. E. *et al.* Barcoded nanoparticles for high throughput in vivo discovery of targeted therapeutics. *Proc. Natl. Acad. Sci.* **114**, 2060–2065 (2017).

11. Paunovska, K. *et al.* A Direct Comparison of in Vitro and in Vivo Nucleic Acid Delivery Mediated by Hundreds of Nanoparticles Reveals a Weak Correlation. *Nano Lett.* **18**, 2148–2157 (2018).

12. B. Guo, A.G. Pearce, K. E. A., Traulsen, A.C. Rintala, A. & Lee, H. Fluorescence Produced by Transfection Reagents Can Be Confused with Green Fluorescent Proteins in Mammalian Cells. *Biotechniques* **31**, 314–321 (2001).

13. Palchetti, S. *et al.* Manipulation of lipoplex concentration at the cell surface boosts transfection efficiency in hard-to-transfect cells. *Nanomedicine Nanotechnology, Biol. Med.* **13**, 681–691 (2017).

# 7 EPILOGUE

The research presented in this PhD thesis has covered three somewhat distinct topics, generally in the context of T cells and cancer. A connection can be made based on the utilization of DNA barcodes to provide an encoding aspect for biomolecules such as dextran- or streptavidin-based MHC reagents, as well as nanoparticle-mRNA formulations.

In manuscript I, molecular encoding of MHC multimers was implemented for the high-throughput detection and interrogation of NARTs. The use of such dextran-based MHC multimers is already a fairly established approach for the detection of antigen-reactive T cells. For this study, however, the approach was adapted to incorporate the combined analysis of T cell recognition with T cell phenotyping. As highlighted in the main introductory section and manuscript I, it is becoming increasingly apparent that in order to achieve success in strategies such as ICB, not only is the presence of tumor-reactive T cells important, but these T cells also need to have a functional phenotype. The utilization of such a screening approach has facilitated the assessment of the characteristics of NARTs, such as the breadth and magnitude, but also the corresponding functional or activation state. These properties could form a combined parameter that could be integrated into the ever-expanding list of immune predictors of clinical outcome to immunotherapy-based strategies. This would enable a more effective design of therapies based on the molecular profile of the given cancer type or patient.

In the additional results section I, the use of a DNA barcode was evaluated for a proof of concept development of novel encoded MHC tetramer reagents for the detection of antigen-reactive T cells. This is a parallel technology to the dextran-based multimers and is based on similar principles, however, some advancements are provided. The commercial availability of fluorescent streptavidin could enable the generation of a larger range of fluorescent MHC tetramers, for expanding the number of different classes of antigen-reactive T cells that can be detected simultaneously. The availability of encoding oligos and chemical reagents would facilitate the molecular encoding of the MHC tetramers. With some oligo adaptation, such encoded MHC tetramers could be incorporated into scRNA-seq platforms to enable the pairing of pMHC recognition with TCR information. Ideally, an off-the-shelf product could be developed. Such a product would entail libraries of barcode-conjugated fluorescent streptavidin in a plate format. Whereby each streptavidin would be encoded by a unique barcode. These plates could be stored and then used on-demand for the assembly of MHC tetramers for the given screening application. For the interrogation of antigen-reactive T cells by FACS, the different classes of reactive T cells, e.g. those reactive towards neoantigens, cancer germline antigens and even the different classes of viral antigens, could be distinguished based on the fluorescent label. These populations could then be sorted and processed for scRNA-seq. The unique barcode encoding for the antigenic epitope would identify the specificity of the reactive T cells, but also provide a means of cell capture for the scRNA-seq workflow. As such, from a single assay, one could obtain the pMHC information on a protein level but also acquire the RNA encoding for the TCR. This pairing of information, at

a single-cell resolution, would enable the further mapping of pMHC-TCR pairs, which would guide the design of novel TCR-based therapies.

In the additional results section II, a very preliminary assessment of the use of DNA barcodes to encode nanoparticle-mRNA formulations is provided. In this scenario, instead of encoding a pMHC specificity, the barcode would encode the specific composition of the given nanoparticle. This would allow the assembly of diverse nanoparticle libraries, which could then be pooled and simultaneously assessed for the delivery of cargo to cells either *in vitro* or directly *in vivo*. Considering the vast chemical space of the nanoparticle realm, a high-throughput approach enabling the simultaneous assessment of effective nanoparticle formulations would be a great asset to the field. Although, as introduced, this concept has already been pioneered. Nonetheless, such nanoparticle screening approaches are still not as widely utilized as they should be. There are still potentially many current nanotherapeutic strategies that could be improved with the use of a high-throughput screening platform. Additionally, optimized nanoparticle delivery systems could enable the development of novel treatment strategies and combination therapies.

I envision a future for cancer therapy, whereby various strategies are combined to provide therapeutic synergy. A relevant example of this would be the combination of ICB with therapeutic cancer vaccination. In an ideal world, the vaccine targets, e.g. neoantigens, could be identified using encoded MHC multimers. In parallel, a nanoparticle screening technique could be used to identify the optimal formulation for delivery to the cells of interest via the desired administration route. The neoantigen could then be synthesized in either a peptide, DNA or RNA format, which could then be formulated with the optimized nanoparticle. The synergy provided by such a combination approach may enable a more widespread favorable clinical outcome for the majority of patients.

# 8 BIBLIOGRAPHY


1. Sewell, A. K. Why must T cells be cross-reactive? *Nat. Rev. Immunol.* **12**, 669–677 (2012).

2. Davis, M. M. & Bjorkman, P. J. The T cell receptor genes and T-cell recognition. *Nature* **334**, 395–402 (1988).

3. Davis, M. M. *et al.* Ligand recognition by αβ T cell receptors. *Annu. Rev. Immunol.* **16**, 523–544 (1998).

4. Lefranc, M. P. *et al.* IMGT®, the international ImMunoGeneTics information system®. *Nucleic Acids Res.* **37**, 1006–1012 (2009).

5. Rudolph, M. G., Stanfield, R. L. & Wilson, I. A. How TCRs bind MHCs, peptides, and coreceptors. *Annu. Rev. Immunol.* **24**, 419–466 (2006).

6. Yaneva, R., Schneeweiss, C., Zacharias, M. & Springer, S. Peptide binding to MHC class I and II proteins : New avenues from new methods. **47**, 649–657 (2010).

7. Fritsch, E. F. *et al.* HLA-Binding Properties of Tumor Neoepitopes in Humans. *Cancer Immunol. Res.* **2**, 522–529 (2014).

8. Jerne, N. K. The somatic generation of immune recognition. *Dev. Comp. Immunol.* **4**, 189 (1980).

9. La Gruta, N. L., Gras, S., Daley, S. R., Thomas, P. G. & Rossjohn, J. Understanding the drivers of MHC restriction of T cell receptors. *Nat. Rev. Immunol.* **18**, 467–478 (2018).

10. Starr, T. K., Jameson, S. C. & Hogquist, K. A. Positive and negative selection of T cells. *Annu. Rev. Immunol.* **21**, 139–176 (2003).

11. Roche, P. A. & Cresswell, P. Antigen Processing and Presentation Mechanisms in Myeloid Cells. *Myeloid Cells Heal. Dis.* 209–223 (2017) doi:10.1128/9781555819194.ch11.

12. Li, Y., Yin, Y. & Mariuzza, R. A. Structural and biophysical insights into the role of CD4 and CD8 in T cell activation. *Front. Immunol.* **4**, 1–11 (2013).

13. Van Den Broek, T., Borghans, J. A. M. & Van Wijk, F. The full spectrum of human naive T cells. *Nat. Rev. Immunol.* **18**, 363–373 (2018).

14. Togashi, Y., Shitara, K. & Nishikawa, H. Regulatory T cells in cancer immunosuppression — implications for anticancer therapy. *Nat. Rev. Clin. Oncol.* **16**, 356–371 (2019).

15. Dominguez-Villar, M. & Hafler, D. A. Regulatory T cells in autoimmune disease. *Nat. Immunol.* **19**, 665–673 (2018).

16. Kumar, B. V., Connors, T. J. & Farber, D. L. Human T Cell Development, Localization, and Function throughout Life. *Immunity* **48**, 202–213 (2018).

17. Actor, J. K. T-Cell Immunity. *Elsevier's Integr. Rev. Immunol. Microbiol.* 25–32 (2012)

doi:10.1016/b978-0-323-07447-6.00004-1.

18. ElTanbouly, M. A. & Noelle, R. J. Rethinking peripheral T cell tolerance: checkpoints across a T cell's journey. *Nat. Rev. Immunol.* (2020) doi:10.1038/s41577-020-00454-2.

19. Kurts, C. *et al.* CD8 T cell ignorance or tolerance to islet antigens depends on antigen dose. *Proc. Natl. Acad. Sci. U. S. A.* **96**, 12703–12707 (1999).

20. Rocha, B., Tanchot, C. & Von Boehmer, H. Clonal anergy blocks in vivo growth of mature T cells and can be reversed in the absence of antigen. *J. Exp. Med.* **177**, 1517–1521 (1993).

21. Kragten, N. A. M. *et al.* Blimp-1 induces and Hobit maintains the cytotoxic mediator granzyme B in CD8 T cells. *Eur. J. Immunol.* **48**, 1644–1662 (2018).

22. Di Benedetto, S. *et al.* Impact of age, sex and CMV-infection on peripheral T cell phenotypes: results from the Berlin BASE-II Study. *Biogerontology* **16**, 631–643 (2015).

23. Gordon, C. L. *et al.* Tissue reservoirs of antiviral T cell immunity in persistent human CMV infection. *J. Exp. Med.* **214**, 651–667 (2017).

24. Kumar, B. V. *et al.* Human Tissue-Resident Memory T Cells Are Defined by Core Transcriptional and Functional Signatures in Lymphoid and Mucosal Sites. *Cell Rep.* **20**, 2921–2934 (2017).

25. Gattinoni, L. *et al.* A human memory T cell subset with stem cell-like properties. *Nat. Med.* **17**, 1290–1297 (2011).

26. Kim, C., Jin, J., Weyand, C. M. & Goronzy, J. J. The transcription factor tcf1 in t cell differentiation and aging. *Int. J. Mol. Sci.* **21**, 1–16 (2020).

27. Escobar, G., Mangani, D. & Anderson, A. C. T cell factor 1: A master regulator of the T cell response in disease. *Sci. Immunol.* **5**, (2020).

28. Chen, Z. *et al.* TCF-1-Centered Transcriptional Network Drives an Effector versus Exhausted CD8 T Cell-Fate Decision. *Immunity* 1–16 (2019) doi:10.1016/J.IMMUNI.2019.09.013.

29. Galletti, G. *et al.* Two subsets of stem-like CD8+ memory T cell progenitors with distinct fate commitments in humans. *Nat. Immunol.* **21**, 1552–1562 (2020).

30. Fuertes Marraco, S. A., Neubert, N. J., Verdeil, G. & Speiser, D. E. Inhibitory receptors beyond T cell exhaustion. *Front. Immunol.* **6**, 1–14 (2015).

31. Legat, A., Speiser, D. E., Pircher, H., Zehn, D. & Fuertes Marraco, S. A. Inhibitory receptor expression depends more dominantly on differentiation and activation than 'exhaustion' of human CD8 T cells. *Front. Immunol.* **4**, 1–15 (2013).

32. Magen, A. *et al.* Single-Cell Profiling Defines Transcriptomic Signatures Specific to Tumor-Reactive versus Virus-Responsive CD4+ T Cells. *Cell Rep.* **29**, 3019-3032.e6 (2019).

33. Schietinger, A. *et al.* Tumor-Specific T Cell Dysfunction Is a Dynamic Antigen-Driven

Differentiation Program Initiated Early during Tumorigenesis. *Immunity* **45**, 389–401 (2016).

34. Verma, V. *et al.* PD-1 blockade in subprimed CD8 cells induces dysfunctional PD-1+CD38hi cells and anti-PD-1 resistance. *Nat. Immunol.* **20**, 1231–1243 (2019).

35. Speiser, D. E., Ho, P. C. & Verdeil, G. Regulatory circuits of T cell function in cancer. *Nat. Rev. Immunol.* **16**, 599–611 (2016).

36. Mak, T. W. & Saunders, M. E. T Cell Activation. in *The Immune Response* vol. 35 373–401 (Elsevier, 2006).

37. Goronzy, J. J. & Weyand, C. M. Mechanisms underlying T cell ageing. *Nat. Rev. Immunol.* **19**, 573–583 (2019).

38. Akbar, A. N., Henson, S. M. & Lanna, A. Senescence of T Lymphocytes: Implications for Enhancing Human Immunity. *Trends Immunol.* **37**, 866–876 (2016).

39. Libri, V. *et al.* Cytomegalovirus infection induces the accumulation of short-lived, multifunctional CD4+CD45RA+CD27- T cells: The potential involvement of interleukin-7 in this process. *Immunology* **132**, 326–339 (2011).

40. Hanahan, D. & Weinberg, R. A. Hallmarks of cancer: The next generation. *Cell* **144**, 646–674 (2011).

41. Binnewies, M. *et al.* Understanding the tumor immune microenvironment (TIME) for effective therapy. *Nat. Med.* **24**, 541–550 (2018).

42. Duan, Q., Zhang, H., Zheng, J. & Zhang, L. Turning Cold into Hot: Firing up the Tumor Microenvironment. *Trends in Cancer* **6**, 605–618 (2020).

43. Gajewski, T. F. The Next Hurdle in Cancer Immunotherapy: Overcoming the Non–T-Cell–Inflamed Tumor Microenvironment. *Semin. Oncol.* **42**, 663–671 (2015).

44. Lussier, D. M. & Schreiber, R. D. *Cancer Immunosurveillance: Immunoediting*. *Encyclopedia of Immunobiology* vol. 4 (Elsevier, 2016).

45. Wilkie, K. P. & Hahnfeldt, P. Mathematical models of immune-induced cancer dormancy and the emergence of immune evasion. *Interface Focus* **3**, (2013).

46. Wu, X. *et al.* Immune microenvironment profiles of tumor immune equilibrium and immune escape states of mouse sarcoma. *Cancer Lett.* **340**, 124–133 (2013).

47. Cabrita, R. *et al.* Tertiary lymphoid structures improve immunotherapy and survival in melanoma. *Nature* **577**, 561–565 (2020).

48. Spranger, S. & Gajewski, T. F. Mechanisms of Tumor Cell-Intrinsic Immune Evasion. *Annu. Rev. Cancer Biol.* **2**, 213–228 (2018).

49. Marijt, K. A. *et al.* Metabolic stress in cancer cells induces immune escape through a PI3K-dependent blockade of IFNγreceptor signaling. *J. Immunother. Cancer* **7**, 1–12 (2019).

50. Disis, M. L. Immune regulation of cancer. *J. Clin. Oncol.* **28**, 4531–4538 (2010).

51. Ostroumov, D., Fekete-Drimusz, N., Saborowski, M., Kühnel, F. & Woller, N. CD4 and CD8 T lymphocyte interplay in controlling tumor growth. *Cell. Mol. Life Sci.* **75**, 689–713 (2018).

52. Burkholder, B. *et al.* Tumor-induced perturbations of cytokines and immune cell networks. *Biochim. Biophys. Acta - Rev. Cancer* **1845**, 182–201 (2014).

53. Giordano, M. *et al.* Molecular profiling of CD 8 T cells in autochthonous melanoma identifies Maf as driver of exhaustion . *EMBO J.* **34**, 2042–2058 (2015).

54. Prendergast, G. C. Immune escape as a fundamental trait of cancer: Focus on IDO. *Oncogene* **27**, 3889–3900 (2008).

55. Coulie, P. G., Van Den Eynde, B. J., Van Der Bruggen, P. & Boon, T. Tumour antigens recognized by T lymphocytes: At the core of cancer immunotherapy. *Nat. Rev. Cancer* **14**, 135–146 (2014).

56. Vlad, A. M., Kettel, J. C., Alajez, N. M., Carlos, C. A. & Finn, O. J. MUC1 Immunobiology: From Discovery to Clinical Applications. *Adv. Immunol.* **82**, 249–293 (2004).

57. Ramos, J. C. & Lossos, I. S. Newly emerging therapies targeting viral-related lymphomas. *Curr. Oncol. Rep.* **13**, 416–426 (2011).

58. van der Burg, S. H. & Melief, C. J. M. Therapeutic vaccination against human papilloma virus induced malignancies. *Curr. Opin. Immunol.* **23**, 252–257 (2011).

59. Forrester, J. V., Xu, H., Lambe, T. & Cornall, R. Immune privilege or privileged immunity? *Mucosal Immunol.* **1**, 372–381 (2008).

60. Wong, K. K., Hassan, R. & Yaacob, N. S. Hypomethylating Agents and Immunotherapy: Therapeutic Synergism in Acute Myeloid Leukemia and Myelodysplastic Syndromes. *Front. Oncol.* **11**, 1–16 (2021).

61. Schumacher, T. N. & Schreiber, R. D. Neoantigens in cancer immunotherapy. *Science (80-. ).* **348**, 69–74 (2015).

62. Jamal-Hanjani, M., Quezada, S. A., Larkin, J. & Swanton, C. Translational implications of tumor heterogeneity. *Clin. Cancer Res.* **21**, 1258–1266 (2015).

63. McGranahan, N. *et al.* Clonal neoantigens elicit T cell immunoreactivity and sensitivity to immune checkpoint blockade. *Science (80-. ).* **351**, 1463–1469 (2016).

64. Segal, N. H. *et al.* Epitope landscape in breast and colorectal cancer. *Cancer Res.* **68**, 889–892 (2008).

65. Bjerregaard, A. M., Nielsen, M., Hadrup, S. R., Szallasi, Z. & Eklund, A. C. MuPeXI: prediction of neo-epitopes from tumor sequencing data. *Cancer Immunol. Immunother.* **66**, 1123–1130 (2017).

66. Karpanen, T. & Olweus, J. The potential of donor T-cell repertoires in neoantigen-targeted cancer immunotherapy. *Front. Immunol.* **8**, 1–8 (2017).

67. Strønen, E. *et al.* Targeting of cancer neoantigens with donor-derived T cell receptor repertoires. *Science (80-. ).* **352**, 1337–1341 (2016).

68. Ali, M. *et al.* Induction of neoantigen-reactive T cells from healthy donors. *Nat. Protoc.* **14**, 1926–1943 (2019).

69. McCutcheon, M. *et al.* A sensitive ELISPOT assay to detect low-frequency human T lymphocytes. *J. Immunol. Methods* **210**, 149–166 (1997).

70. Altman, J. D. *et al.* Phenotypic analysis of antigen-specific T lymphocytes. *Science (80-. ).* **274**, 94–96 (1996).

71. Toebes, M. *et al.* Design and use of conditional MHC class I ligands. *Nat. Med.* **12**, 246–251 (2006).

72. Bakker, A. H. *et al.* Conditional MHC class I ligands and peptide exchange technology for the human MHC gene products HLA-A1, -A3, -A11, and -B7. *Proc. Natl. Acad. Sci.* **105**, 3825–3830 (2008).

73. Rodenko, B. *et al.* Generation of peptide-MHC class I complexes through UV-mediated ligand exchange. *Nat. Protoc.* **1**, 1120–32 (2006).

74. Bentzen, A. K. & Hadrup, S. R. Evolution of MHC-based technologies used for detection of antigen-responsive T cells. *Cancer Immunol. Immunother.* **0**, 0 (2017).

75. Bentzen, A. K. & Hadrup, S. R. Evolution of MHC-based technologies used for detection of antigen-responsive T cells. *Cancer Immunol. Immunother.* **66**, 657–666 (2017).

76. Andersen, R. S. *et al.* Parallel detection of antigen-specific t cell responses by combinatorial encoding of MHC multimers. *Nat. Protoc.* **7**, 891–902 (2012).

77. Newell, E. W. *et al.* Combinatorial tetramer staining and mass cytometry analysis facilitate T-cell epitope mapping and characterization. *Nat. Biotechnol.* **31**, 623–629 (2013).

78. Dolton, G. *et al.* Comparison of peptide-major histocompatibility complex tetramers and dextramers for the identification of antigen-specific T cells. *Clin. Exp. Immunol.* **177**, 47–63 (2014).

79. Schmitt, T. M. *et al.* Enhanced-affinity murine T-cell receptors for tumor/self-antigens can be safe in gene therapy despite surpassing the threshold for thymic selection. *Blood* **122**, 348—356 (2013).

80. Christophersen, A. Peptide-MHC class I and class II tetramers: From flow to mass cytometry. *Hla* **95**, 169–178 (2020).

81. Uchtenhagen, H. *et al.* Efficient ex vivo analysis of CD4+ T-cell responses using combinatorial HLA class II tetramer staining. *Nat. Commun.* **7**, (2016).

82. Cole, D. K. *et al.* Human TCR-Binding Affinity is Governed by MHC Class Restriction. *J. Immunol.* **178**, 5727–5734 (2007).

83. Huang, J. *et al.* Detection, phenotyping, and quantification of antigenspecific T cells using

a peptide-MHC dodecamer. *Proc. Natl. Acad. Sci. U. S. A.* **113**, E1890–E1897 (2016).

84. Batard, P. *et al.* Dextramers: New generation of fluorescent MHC class I/peptide multimers for visualization of antigen-specific CD8+ T cells. *J. Immunol. Methods* **310**, 136–148 (2006).

85. Bentzen, A. K. *et al.* Large-scale detection of antigen-specific T cells using peptide-MHC-I multimers labeled with DNA barcodes. *Nat. Biotechnol.* **34**, 1037–1045 (2016).

86. Kula, T. *et al.* T-Scan: A Genome-wide Method for the Systematic Discovery of T Cell Epitopes. *Cell* **178**, 1016-1028.e13 (2019).

87. Decker, W. K. & Safdar, A. Bioimmunoadjuvants for the treatment of neoplastic and infectious disease: Coley's legacy revisited. *Cytokine Growth Factor Rev.* **20**, 271–281 (2009).

88. Intlekofer, A. M. & Thompson, C. B. At the Bench: Preclinical rationale for CTLA-4 and PD-1 blockade as cancer immunotherapy. *J. Leukoc. Biol.* **94**, 25–39 (2013).

89. Jain, N., Nguyen, H., Chambers, C. & Kang, J. Dual function of CTLA-4 in regulatory T cells and conventional T cells to prevent multiorgan autoimmunity. *Proc. Natl. Acad. Sci.* **107**, 1524–1528 (2010).

90. Waldman, A. D., Fritz, J. M. & Lenardo, M. J. A guide to cancer immunotherapy: from T cell basic science to clinical practice. *Nat. Rev. Immunol.* (2020) doi:10.1038/s41577-020-0306-5.

91. Francisco, L. M., Sage, P. T. & Sharpe, A. H. The PD-1 pathway in tolerance and autoimmunity. *Immunol. Rev.* **236**, 219–242 (2010).

92. Boyiadzis, M. M. *et al.* Significance and implications of FDA approval of pembrolizumab for biomarker-defined disease. *J. Immunother. Cancer* **6**, 1–7 (2018).

93. Latchman, Y. *et al.* PD-L2 is a second ligand for PD-1 and inhibits T cell activation. *Nat. Immunol.* **2**, 261–268 (2001).

94. Dong, H. *et al.* Tumor-associated B7-H1 promotes T-cell apoptosis: A potential mechanism of immune evasion. *Nat. Med.* **8**, 793–800 (2002).

95. Waterhouse, P. *et al.* Lymphoproliferative Disorders with Early Lethality in Mice Deficient in Ctla-4 Published by : American Association for the Advancement of Science Stable URL : http://www.jstor.org/stable/2888113 JSTOR is a not-for-profit service that helps scholars , rese. *Science (80-. ).* **270**, 985–988 (1995).

96. Nishimura, H., Nose, M., Hiai, H., Minato, N. & Honjo, T. Development of lupus-like autoimmune diseases by disruption of the PD-1 gene encoding an ITIM motif-carrying immunoreceptor. *Immunity* **11**, 141–151 (1999).

97. Kumar, V. *et al.* Current diagnosis and management of immune related adverse events (irAEs) induced by immune checkpoint inhibitor therapy. *Front. Pharmacol.* **8**, (2017).

98. Postow, M. A., Sidlow, R. & Hellmann, M. D. Immune-Related Adverse Events Associated with Immune Checkpoint Blockade. *N. Engl. J. Med.* **378**, 158–168 (2018).

99. Fridman, W. H., Pagès, F., Sautès-Fridman, C. & Galon, J. The immune contexture in human tumours: Impact on clinical outcome. *Nat. Rev. Cancer* **12**, 298–306 (2012).

100. Yost, K. E. *et al.* Clonal replacement of tumor-specific T cells following PD-1 blockade. *Nat. Med.* **25**, 1251–1259 (2019).

101. Krishna, S. *et al.* Stem-like CD8 T cells mediate response of adoptive cell immunotherapy against human cancer. *Science (80-. ).* **370**, 1328–1334 (2020).

102. Gupta, P. K. *et al.* CD39 Expression Identifies Terminally Exhausted CD8+ T Cells. *PLoS Pathog.* **11**, 1–21 (2015).

103. Shevchenko, I. *et al.* Enhanced expression of CD39 and CD73 on T cells in the regulation of anti-tumor immune responses. *Oncoimmunology* **9**, 1–13 (2020).

104. van der Leun, A. M., Thommen, D. S. & Schumacher, T. N. CD8+ T cell states in human cancer: insights from single-cell analysis. *Nat. Rev. Cancer* **20**, 218–232 (2020).

105. Hamanishi, J. *et al.* Programmed cell death 1 ligand 1 and tumor-infiltrating CD8+ T lymphocytes are prognostic factors of human ovarian cancer. *Proc. Natl. Acad. Sci. U. S. A.* **104**, 3360–3365 (2007).

106. Lim, S. H. *et al.* Pembrolizumab for the treatment of non-small cell lung cancer. *Expert Opin. Biol. Ther.* **16**, 397–406 (2016).

107. Rizvi, N. A. *et al.* Mutational landscape determines sensitivity to PD-1 blockade in non–small cell lung cancer. *Science (80-. ).* **348**, 124–128 (2015).

108. Eroglu, Z. *et al.* High response rate to PD-1 blockade in desmoplastic melanomas. *Nature* **553**, 347–350 (2018).

109. Vandeven, N. A. & Nghiem, P. Merkel cell carcinoma: An unusually immunogenic cancer proves ripe for immune therapy. *J. Oncol. Pract.* **12**, 649–650 (2016).

110. Banerjea, A., Bustin, S. A. & Dorudi, S. The immunogenicity of colorectal cancers with high-degree microsatellite instability. *World J. Surg. Oncol.* **3**, 1–9 (2005).

111. Blank, C. U., Haanen, J. B., Ribas, A. & Schumacher, T. N. The 'cancer immunogram'. *Science* vol. 352 658–660 (2016).

112. Bruni, D., Angell, H. K. & Galon, J. The immune contexture and Immunoscore in cancer prognosis and therapeutic efficacy. *Nat. Rev. Cancer* **20**, 662–680 (2020).

molecular pharmaceutics

Review

Cite This: *Mol. Pharmaceutics* 2019, 16, 2265−2277

pubs.acs.org/molecularpharmaceutics

# Lipid Nanoparticles for Delivery of Therapeutic RNA Oligonucleotides

Keith Henry Moss,[†] Petya Popova,[‡] Sine R. Hadrup,[†] Kira Astakhova,*[,‡] and Maria Taskova*[,‡]

[†]DTU Health Technology, 202 Kemitorvet, 2800 Kongens Lyngby, Denmark

[‡]DTU Chemistry, 206-207 Kemitorvet, 2800 Kongens Lyngby, Denmark

**ABSTRACT:** Gene therapy is an exciting field that has the potential to address emerging scientific and therapeutic tasks. RNA-based gene therapy has made remarkable progress in recent decades. Nevertheless, efficient targeted delivery of RNA therapeutics is still a prerequisite for entering the clinics. In this review, we introduce current delivery methods for RNA gene therapeutics based on lipid nanoparticles (LNPs). We focus on the clinical appeal of recent RNA NPs and discuss existing challenges of fabrication and screening LNP candidates for effective translation into drugs of human metabolic diseases and cancer.

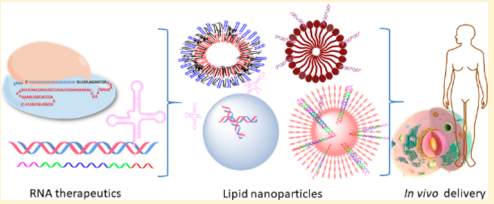


**KEYWORDS:** *gene therapy, RNA, delivery, lipid nanoparticle (LNP), LNP fabrication, LNP screening*



## INTRODUCTION

RNA therapeutics is a broad group of RNA oligo- and polymers that knock down, insert, or replace a disease-associated RNA (Figure 1). RNA therapeutics act via diverse biological mechanisms, including antisense oligonucleotides (ASOs), RNA interference oligonucleotides, messenger RNAs (mRNAs), and single-guide RNA (sgRNA)/CRISPR systems. Some RNA therapeutics have already reached clinical trials and have been approved by the FDA (Table 1). For instance, Eteplirsen, a 30-nucleotide long phosphorodiamidate morpholino oligomer (PMO), is a splice switching oligo (SSO) that excises exon 51 in dystrophin RNA. The excision results in production of a functional dystrophin gene in duchenne muscular dystrophy (DMD) patients.[1] Improved symptoms, however, were observed in only 16% of patients. The specific challenges that Eteplirsen faced were low efficacy and rapid clearance of the PMO.[2,3]

Very recently, the small interfering (siRNA) therapeutic, Patisiran, became the first FDA-approved siRNA therapy for hereditary transthyretin-mediated familial amyloidosis. It contains several 2′ OMe modifications on the uridine nucleotides. Patisiran contains a lipid nanoparticle (LNP) formulation, which consists of a pH-sensitive fusogenic amino lipid (MC3), phosphatidylcholine (DSPC), cholesterol, and dimyristolglycerol-PEG.[4] In a phase III clinical trial, Patisiran, administered intravenously, showed high therapeutic activity with no apparent side effects. Serum levels of transthyretin were 75% lower in patients treated with the drug compared to the placebo group.[5] Lumasiran (ALN-GO1) is another promising siRNA therapeutic that reached clinical trials, developed for treatment of primary hyperoxaluria (PH1). In Lumasiran, the RNA drug is conjugated to *N*-acetylgalactosamine (GalNAc), and it targets glycolate oxidase in human hepatocytes. Recently conducted phase I/II clinical trial studies reported a 75% decrease in urine excretion of oxalates.

Excitingly, RNA therapy has the potential to provide a treatment option for multiple genetic diseases. Nevertheless, there are challenges with RNA stability, intracellular delivery, and off-target effects in vivo. In comparison to antibodies, that can only bind receptors on the cell surface to reach their cellular target, RNA therapeutics must cross cellular membranes and reach the desired intracellular compartment. Nuclease degradation, poor cellular uptake, and a low binding affinity to complementary target sequences are issues that need to be addressed. Due to the evolutionarily conserved viral defense pathway that is built into mammalian cells, especially immune cells, an innate immune system might be activated by exogenous RNA. This immune activation is driven by recognition of specific molecular patterns associated with pathogens by pattern-recognition receptors (PRRs), which act as RNA sensors. These RNA sensors, e.g., toll-like receptors (TLRs) and retinoic acid-inducible gene I (RIG-I), are located in intracellular compartments, such as the endosome and cytosol, respectively.[6] In order to reduce immunogenicity while improving biodistribution and pharmacokinetic properties, chemical modifications of RNA can be introduced in the phosphodiester linkages, nucleobases, and/or ribose backbone.[7] Furthermore, to address kidney filtration and to improve delivery, chemical conjugation and nanoparticle (NP)-based delivery methods can be applied.

To date, various NPs and nanomaterials (Figure 2) have been proposed for the delivery of therapeutic RNA.[8−10] To mention a few, organic polymers, carbohydrate, and peptide-based formulations have been prepared and tested (Figure 2). LNPs and their modifications are among those systems that

**Received:** December 13, 2018
**Revised:** May 3, 2019
**Accepted:** May 7, 2019
**Published:** May 7, 2019




DOI: 10.1021/acs.molpharmaceut.8b01290
*Mol. Pharmaceutics* 2019, 16, 2265−2277

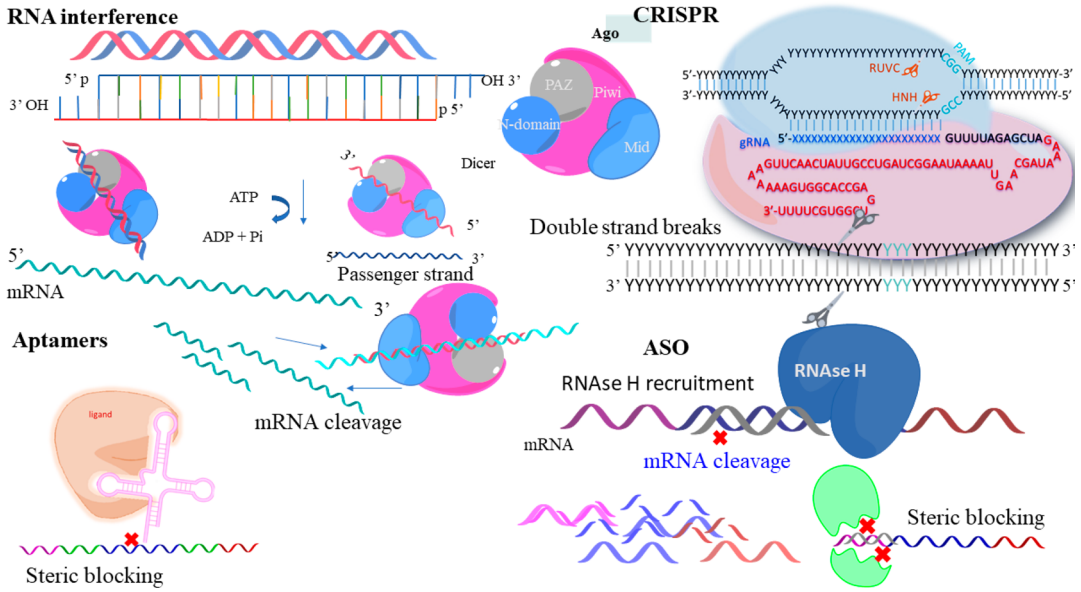


**Figure 1.** RNA therapeutics mechanism of action. (Left) RNA interference and aptamers; (right) CRISPR and ASOs.

**Table 1. List of FDA-Approved RNA Therapeutics**[a]

| name | RNA drug type | target site |
|---|---|---|
| Mipomersen, 2013 | AS 20nt PS 2′ MOE gapmer | apoB mRNA in homozygous familial hypercholesterolemia |
| Exondys 51, 2016 | 30nt PMO | DMD |
| Defibrotide | 9−80nt, 90% ss ON, 10% ds; from pig's intestinal mucosa | liver veno-occlusive disease |
| Spinraza, Nusinersen | 18nt PS 2′-O-methoxyethoxy ASO, all cytidines have methyl modification at 5′ end | inclusion of exon 7 in spinal muscular atrophy mRNA |
| Vitraven, Fomivirsen, 1998 (discontinued by Novataris, 2006) | 21nt PS | cytomegalovirus (CMV) retinitis |
| Macugen, 2004 | 2′ OMe and the pyrimidine ribose sugars all 2′-F | VEGF1656, pM range affinity binding, macular degeneration |
| Patisiran, 2018 | siRNA, 2′ OME, lipid NP delivery | tansthyretin in hereditary transthyretin amyloidosis |
| Tegsedi (Inotersen), 2018 | 20nt, AS, 2′ MOE RNA, PS, all cytidines have methyl modification at 5′ end | transthyretin in hereditary transthyretin amyloidosis |

[a]ON, oligonucleotide; AS, antisense; PS, phosphorothioate; and PMO, phosphomorpholidate.

have been recently approved by FDA and therefore represent an extremely attractive object of studies.[11−13]

In this review, we present the most recent delivery strategies for RNA gene therapeutics with a focus on emerging LNP solutions. Our focus is being paid to formulations in clinical translation, their unique features, challenges with preparation and screening, and ways to promote the development of new RNA LNP formulations.

## LIPID NANOPARTICLES IN RNA THERAPY

**Charged Cationic Lipids.** LNPs gained much attention in the field of nucleic acid delivery when Felgner and colleagues, in 1987, demonstrated that cationic lipids, 1,2-di-*O*-octadecenyl-3-trimethylammonium propane (DOTMA) and dioleyl phophatidylethanolamine (DOPE), when formulated with pDNA, resulted in the formation of liposomes capable of in vitro transfection.[11] Only a couple years later, in 1989, DOTMA and DOPE were used to complex with luciferase mRNA to form LNPs for transfection of human, mouse, rat, drosophila, and *Xenopus* cells.[12]

LNP formation with nucleic acids in an aqueous environment is driven by a process of self-assembly, which is influenced by the degree of hydrophilicity and hydrophobicity within the regions of the lipid components. Cellular membranes, consisting of phospholipids in a lamellar or bilayer assembly, represent a classical example of lipid self-assembly occurring in vivo.[14] In order to improve intracellular delivery of nucleic acids with LNPs, a transition from lamellar to the reversed hexagonal phase of the self-assembled lipid complex is required.[15] The transition induces cell membrane destabilization, which is necessary for internalization of the cationic lipid−nucleic acid complex into the cytosol.[15]

Inspired by initial success, extensive effort has been put into the synthesis of cationic lipids for use in gene delivery both in vitro and in vivo. This has outlined key requirements in the structural design and properties of the cationic lipid, a positively charged headgroup (monocation or polycation, linear or heterocyclic) attached, via a linker bond, to a hydrophobic group (cholesterol or aliphatic).[13] Several subtypes of cationic lipids exist, including monovalent and multivalent aliphatic lipids and cholesterol derivatives. The lipid structure, i.e., nature of the charged headgroup (primary, secondary, and tertiary amine or quaternary ammonium salt), is a critical determinant of transfection efficiency and the associated cytotoxicity.[16] For instance, cationic derivatives of


DOI: 10.1021/acs.molpharmaceut.8b01290
*Mol. Pharmaceutics* 2019, 16, 2265−2277

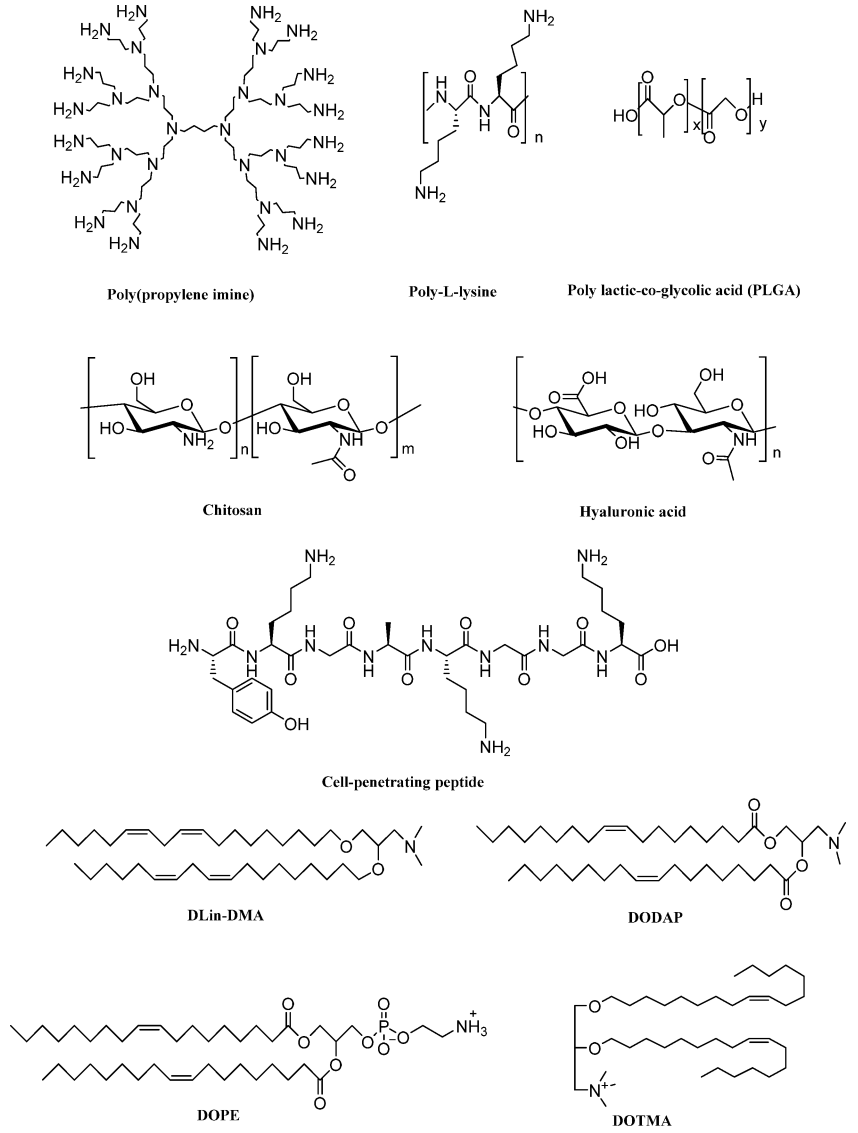


**Figure 2.** Examples of NP constituent chemical structures of polymers (poly(propylene imine), poly-L-lysine, and PLGA), carbohydrates (chitosan and hyaluronic acid), cell penetrating peptide, and lipids (DLin-DMA, DODAP, and DOPE).[8−13]

cholesterol with quaternary head groups have been reported to display higher toxicity than their tertiary counterparts.[17]

The transfection efficiency of cationic lipids depends on several factors, such as the ability to complex with nucleic acids, to promote cellular uptake, and successive endosomal escape. It was later hypothesized, that, following endocytosis, an interaction between cationic lipids of the liposome and anionic phospholipids in the endosomal membrane promotes membrane disruption and subsequent release of LNP cargo into the cytosol.[18] The length of the hydrophobic anchor or aliphatic chain as well as the degree of saturation also influence transfection efficiency and cytotoxicity. It has been reported, that, in a homologous series of lipids with alkyl chains spanning from $C_{14}$ to $C_{18}$, the shorter chain resulted in a bilayer with increased fluidity, which enhanced intermembrane mixing and the subsequent transfection process.[13,19] Intermembrane mixing, driven by membrane destabilization, is dependent on the transition temperature of the lipids in the lipoplex. A lower transition temperature indicates that lipids will more readily shift from the high stability lamellar phase to the low stability hexagonal phase.[20] Unsaturated alkyl chains (i.e., oleoyl-based lipids) have proven to be the most effective for gene delivery, with double-chained lipids being predominant in LNP investigations, as they are able to form lamellar phases without the need of helper lipids.[21] The linker group typically consists of amide, ester, or ether bonds connecting the hydrophobic and hydrophilic regions of the lipid. Ether bonds are stable with high transfection efficiency; however, they also display toxicity. Ester bonds are biodegradable with reduced toxicity but can result in the premature release of cargo due to lipases and/or nucleases present in the endosome and lysosome, respectively.[22] Additionally, carbamate-based linkers that show stability in circulation are hydrolyzed in the acidic endosomal compartment and are associated with reduced cytotoxicity.[23]

There are several commercial products built on the success of cationic lipids, which have been applied as transfection reagents. The first transfection reagent for DNA in mammalian cells, lipofectin, consisted of DOTMA/DOPE.[11] The use of lipid-mediated transfection reagents, i.e. lipofectamine reagents, is now accepted as the gold standard for delivery of exogenous DNA or RNA into cells, despite their well-known cytotoxicity.[24] The inclusion of amphiphilic lipid molecules,


DOI: 10.1021/acs.molpharmaceut.8b01290
Mol. Pharmaceutics 2019, 16, 2265−2277

such as cationic lipids, in LNP formulations has proven to be an effective means of RNA encapsulation, cytoplasmic delivery, and endosomal escape. LNPs are hence regarded as one of the principle strategies for nonviral gene delivery,[25] with several formulations progressing into clinical trials.[26,27]

**Toxicity of LNPs and Strategies To Overcome It.** A major drawback with the use of cationic lipids for gene delivery is the high net positive charge associated with the headgroup, as well as induction of immune response and short circulation time due to rapid plasma clearance.[28,29] Furthermore, particles of cationic nature are known to undergo accumulation in the liver, lung, and spleen.[30] Lipoplexes, i.e., lipid−nucleic acid complexes, formulated with cationic lipids have been reported to induce inflammatory responses and immune cell activation following systemic administration, and the majority are endocytosed by Kupffer cells in the liver.[31] Consequently, a great effort has been focused on the rational design of lipids with reduced toxicity for application in nucleic acid delivery. Nevertheless, even with the emergence of a vast variety of their analogues for gene therapy,[32] gene expression was still associated with a substantial degree of cytotoxicity.[33]

In general, toxicity is a combination of biochemical processes that leads to inflammation and short-term[34] or long-term[35] effects in an exposed organism. Toxicity of a low to moderate level can be beneficial to the treatment. Kranz et al. studied the immunological effects of intravenously administrated RNA lipoplexes.[36] RNA lipoplexes trigger interferon-$\alpha$ release by dendritic cells and macrophages that are similar to the response of an early viral infection. In this case, interferon-$\alpha$ speeds up T cell maturation, which is beneficial for tumor treatment using RNA lipoplexes as a vaccine.[36] Moreover, combinational treatment by mRNA-LNP and FDA-approved TLR agonist, monophosphoryl lipid A, allowed for high antigen expression with controlled interferon release, showing a path for even safer strategies to induce T cell immunity toward cancer.[37]

Nevertheless, toxicity due to uncontrolled cytokine release can be dangerous to a patient. Cytokine release syndrome (CRS) is a life-threatening toxicity that is caused by uncontrollably increased levels of pro-inflammatory cytokines, e.g., interleukin-6 and interferon.[35] CRS is rated in levels one to four, four being the hardest. It is considered life-threatening at levels three and four.[35] Being a huge concern in cancer immunotherapy, CRS of moderate to high levels is also observed as a result of LNP treatments. Hirsova et al. reported liver inflammation as a result of CRS after the treatment with palmitate and other lipids used as components of LNPs and lipoplexes.[38] Kubota et al. showed that inflammatory cytokine response differs among lipoplexes and LNPs.[39] siRNA-loaded LNPs released lower amounts of tumor necrosis factor $\alpha$ and interleukin-1$\beta$ than lipoplexes. The authors hypothesize that molecular structure has an impact on immune stimulation by NPs and suggest careful optimization of the composition prior to extended studies in vivo.[39]

Complement activation is another pathological process that has been observed for LNP-formulated modified mRNA in rats and monkeys.[40] The authors point on the crucial importance of dose adjustment to make the complement activation mild and reversible. Besides that, coagulation parameters, cell count, and heart tissue might be affected by treatment with LNPs.[40] The use of shielding lipids, such as lipid-anchored polyethylene glycol (PEG) in LNP formulations, has been generally applied to increase systemic circulation time, reduce nonspecific cell interaction and uptake, reduce particle size, and prevent aggregation during storage.[41−43] However, there have been multiple reports that PEG induces production of anti-PEG immunoglobulin M (IgM) and subsequent complement activation, resulting in accelerated clearance.[44,45] It has been reported that PEG shielding may reduce efficacy both in vitro and in vivo, due to steric blocking of the LNP−endosomal membrane interaction, hindering endosomal escape.[42] Strategies to improve efficacy of PEGylated LNP include incorporation of acid- or pH-sensitive-modified PEG to promote the release of PEG from the lipid core, thereby reducing the negative effects of shielding on endosomal release.[43,46]

Multiple works have been dedicated to reducing pro-inflammatory activity of nonvaccine RNA LNPs. Abrams et al. report on successful *Ssb* gene silencing in mouse liver by the siRNA-LNP drug candidate LNP201.[47] LNP201 induced an inflammatory response in mice, via activation of the MAPK kinase pathway. Notably, inflammation was completely inhibited using a glucocorticoid agonist, dexamethasone, without reducing the activity of the siRNA payload. In another work, an increased transfection efficiency and a reduction in cytotoxicity could be obtained when utilizing cholesterol analogs (DC-cholesterol) and helper/fusogenic lipids (DOPE) in LNP-mediated mRNA delivery.[48] Lastly, Asai and Oku[34] point on PEGylation as a steric block to pro-inflammatory interaction of LNP with immune cells. Besides PEG, other ligands, including peptides and antibodies, are suggested to decorate LNPs' surface, to overcome the systemic toxicity.[34]

**Ionizable Cationic Lipids.** The off-target effect and systemic toxicity associated with the use of permanently charged cationic lipids, for RNA delivery in vivo, lead to the development of ionizable lipids with reduced toxicity and immunogenicity. 1,2-Dioleoyl-3-dimethyaminopropane (DODAP) was the first ionizable lipid utilized in a LNP formulation. Using DODAP, up to 70% encapsulation of DNA/RNA has been achieved, in both uni- and multilamellar liposomes.[49] This structure, consisting of two oleyl chains, has served as the foundation for the development of additional ionizable lipids, exemplified by Figure 2. 1,2-Dilinoleyloxy-*N*,*N*-dimethyl-3-aminopropane (DLinDMA), another first generation ionizable lipid, with linoleyl hydrocarbon chains, was reported to be optimal for RNA delivery in hepatocytes, with up to 90% silencing of mRNA in hepatocytes in cynomolgus monkeys.[50] DLinDMA has since demonstrated initial proof of concept in humans[51] and has resulted in the development of second generation ionizable cationic lipids, such as DLin-MC3-DMA. MC3-DMA, one of the lipid components in the Patisiran formulation, has been synthesized containing ester linkages for biodegradability. The biocleavable linker facilitates favorable stability at physiological pH while allowing enzymatic hydrolysis in tissues and intracellular compartments, due to local esterase and/or lipase activity.[52] This promotes improved tolerability and a safety profile, while maintaining high potency in rodents and nonhuman primates (NHP).[52] It should be noted, that the level of gene silencing in NHP was less than the level of gene silencing in mice. This may, in part, be because LNP composition was optimized in mice. Further optimization of the formulation composition would be required to attain optimal efficacy in NHP. These novel amino lipids, however, are the first demonstration of biodegradable lipids with an efficacy comparable to the most


DOI: 10.1021/acs.molpharmaceut.8b01290
*Mol. Pharmaceutics* 2019, 16, 2265−2277

advanced lipids currently available for siRNA delivery, and they show promise for use in future RNAi therapies.

A recent delivery platform combines a lipid component with unlocked nucleic-acid-modified RNA (LUNAR). Similarly to Patisiran, LUNAR achieves biodegradability due to the presence of an ionizable lipid with ester linkage in the lipid backbone.[53,54] The hyperactive factor IX (FIX) mRNA variants used in the LUNAR system were reported to have 8−10 times the therapeutic effect compared to the current recombinant human FIX protein therapy. The authors reason that LUNAR-encapsulated FIX mRNA is preferentially targeted to the liver, translated into protein by hepatocytes, and released into circulation. The term "targeting" should, however, be used with caution, as the liver is a natural site of NP accumulation following intravenous administration.[55] That being said, the liver is a site for many physiological functions and a relevant target for many genetic diseases. So, this phenomenon may be harnessed for hepatic delivery strategies. Additionally, a combined approach using an ionizable lipid-like material (C12-200) formulated with helper lipids for delivery of Cas9 mRNA, and an AAV encoding a sgRNA and repair template, has been utilized for hepatocyte gene editing in vivo.[56] The combined viral and nonviral mediated delivery allowed for short-term expression of Cas9 nuclease, providing on-target gene editing while reducing off-target editing. Another ionizable lipid (8-O14B), with bioreducible properties, was used for the codelivery of supercharged Cre recombinase protein and Cas9:sgRNA both in vitro and in vivo.[57] The bioreducible nature is provided by the inclusion of a disulfide bond in the hydrophobic tail. This undergoes reduction in intracellular compartments due to, for example, the presence of high concentrations of glutathione, ultimately, facilitating endosomal escape of the protein-RNA complex. In human cell culture, the 8-O14B lipid enabled up to 70% Cre- and Cas9:sgRNA-mediated gene recombination and knockout. Under optimized in vitro conditions, the Cre/8-O14B complex was injected into different sites in the brain of mice. Notably, the nanocomplexes delivered to the brain were confined to the injection site. This may indicate potential for use in genome editing in specific neuronal populations.

A novel class of synthetic charge-unbalanced amino-lipids, termed cationic quaternary ammonium sulfonamide amino lipids (CSALs), have recently been explored for siRNA delivery.[58] Through synthesis of multiple lipid analogues with varied linker amine, aliphatic tail side chain, and headgroup amine, a lead CSAL LNP was developed. This CSAL LNP enabled in vivo delivery of an RNA drug candidate to the lungs in normal and tumor-burdened mice.[58] The systematic, modular design implemented here, for the library generation of CSALs, enabled the assessment of structural modifications and the relative contributions to biophysical properties of the LNPs in regard to size, surface charge, and siRNA encapsulation.

Structure and morphology of ionizable cationic lipids are being actively optimized, leading to several successful formulations for both siRNA and mRNA delivery. A phase I clinical trial is currently ongoing for the treatment of advanced solid tumors, whereby siRNA against EphA2 is delivered via an LNP (NCT01591356, Table 2). Another clinical trial involving delivery using an LNP, more specifically, an ASO encapsulated in an LNP (liposomal Grb2), is currently in phase I/II for the treatment of chronic myelogenous leukemia (CML)

**Table 2. Current Clinical Trials Involving NP-Mediated Oligonucleotide Delivery**

| drug name | oligonucleotide | target | disease | delivery vehicle | phase | ClinicalTrials.gov identifier |
|---|---|---|---|---|---|---|
| *STP705* | siRNA | TGF-1$\beta$ and Cox-2 | hypertrophic scarring | peptide (histidine−lysine copolymer) | I/II | NCT02956317 |
| *siG12D-LODER* | siRNA | *KRASG12D* | cancer (pancreatic) | degradable polymeric matrix | II | NCT01676259 |
| *iExosomes*[b] | siRNA | *KRASG12D* mutation | cancer (pancreatic) | extracellular vesicle (exosome) | I | NCT03608631 |
| *NU-0129* | siRNA | *BCL2L12* | cancer (glioblastoma multiforme) | gold NP | I | NCT03020017 |
| *liposomal Grb2* | ASO | Grb2 gene | cancer (CML) | LNP | Ib/IIa | NCT02923986, NCT02781883, NCT01159028 |
| *siRNA-EphA2-DOPC* | siRNA | EphA2 gene | cancer (advanced solid tumors) | LNP | I | NCT01591356 |
| *Lipo-MERIT* | mRNA | tumor-associated antigens | cancer (melanoma) | LNP | I | NCT02410733 |
| *TNBC-MERIT* | mRNA | tumor-associated antigens | cancer (triple negative breast) | LNP | I | NCT02316457 |
| *mRNA-1325* | mRNA | viral antigenic proteins | zika | LNP | I | NCT03014089 |
| *mRNA-2416*[c] | mRNA | OX40L | cancer (advanced/refractory solid tumor malignancies or lymphoma | LNP | I | NCT03323398 |
| *Pbi-shRNA* | shRNA | EWS/FLI1 gene | cancer (Ewing's sarcoma) | LNP | I | NCT02736565 |
| *MTL-CEBPA* | saRNA | CEBPA gene | cancer (liver) | LNP | I | NCT02716012 |
| *SGT-53* | pDNA | p53 gene | cancer (relapsed/refractory solid tumors) | LNP | I/II | NCT02354547, NCT02340156, NCT02340117 |

[a]DOPC, 1,2-dioleoyl-sn-glycero-3-phosphocholine; saRNA, small-activating RNA; shRNA, short hairpin RNA; and pDNA, plasmid DNA. [b]Phase I completed October 29th, 2018. [c]Phase I completed December 31st, 2018.



DOI: 10.1021/acs.molpharmaceut.8b01290
Mol. Pharmaceutics 2019, 16, 2265−2277

(NCT02923986, NCT02781883, and NCT01159028; Table 2).

**LNP Structure−Function Relationship and Screening.** An universal delivery system applicable for the transfection of different classes of nucleic acids, i.e., DNA, siRNA, and mRNA, into different cell lines or primary cells has yet to be achieved. This is, in part, due to the varying nature of the nucleic acid therapeutics. For example, single/double-stranded DNA vs double-stranded RNA, mRNA, and CRISPR-Cas9 sgRNA all have different molecular masses. This means that NP systems are typically adapted to molecular features of the specific nucleic acid.[59] Moreover, the combinatorial chemical space of the LNP realm is immense. The sheer number of different lipids and lipid-like materials that can potentially be utilized for oligonucleotide delivery makes the screening for formulation parameters extremely laborious. Thus, it is difficult to fully explore the chemical space to find the optimal formulation. LNP formulation parameters can be systematically optimized through the one-factor-at-a-time (OFAT) method to generate lipid libraries for functional assessment. For example, to assess the efficiency of delivery in vitro/in vivo in order to reduce the toxicity associated with LNPs.[60] The libraries are rationally designed with varying lipid components and molar composition for the given therapeutic application and oligonucleotide cargo. Such a technique has been applied to optimize the LNP formulation for mRNA delivery in cancer immunotherapy.[61] On the basis of the structure−function knowledge, a general guide for screening of LNPs has been described by Patel et al., who suggested the following screening steps, (1) selection of individual lipid components and preliminary screening of a formulation, (2) studying partitioning behavior and selecting the size of LNP, (3) assessing properties of combined LNPs in vitro, and (4) optimization.[62] Although the initial design is well described, two key steps are missing in the workflow proposed by Patel et al., structural investigations of LNPs and in vivo assays.

Despite attempts to the rational design of LNP structure, LNP-mediated RNA therapies are limited by the poor understanding of how LNP structure and morphology influences biodistribution to off-target organs and delivery efficiency to target cells, in vivo. To improve this, structures of siRNA- and mRNA-loaded LNPs have been studied by dynamic solid-state nuclear magnetic resonance (NMR).[63] The LNPs were composed of the aforementioned ionizable cationic lipid DLin-MC3-DMA, a phospholipid DSPC, cholesterol, and DMPE-PEG2000. Phosphorus and carbon chemical shifts were found to be useful in determining different content and morphology of LNPs. A striking finding was that the structure of LNP was dramatically changed when the RNA payload was applied. Specifically, the loaded LNPs tended to result in layering of DSPC and DMPE-PEG around a rather homogeneous core. RNA cargo was located in the subcore or on the surface of LNP, depending on the composition.[63] This study introduces a new model for LNP structure (homogenous core−shell) and potentially rules out the multilamellar vesicle model, which has previously been used to describe LNPs. This highlights the need for further characterization techniques, such as solid-state NMR, to elucidate a better mechanistic understanding of RNA encapsulation by LNPs, the resulting supramolecular assembly, and the subsequent biological interactions in order to assist the rational design of future LNPs.

PEGylation, as previously mentioned, is a broadly applied modification of LNPs that improves biodistribution and reduces toxicity. Hence, the properties of PEG modification are important factors that need to be taken into consideration when preparing PEGylated LNPs. Wilson et al. used pulsed gradient spin echo (PGSE) NMR to investigate PEG shedding from LNPs ex vivo.[64] In doing this, a combination of DLin-MC3-DMA[63] with DOleylDMA or DSA/DMA-PEG was used. LNPs modified with PEG via shorter lipid anchors showed rapid shedding of PEG in rat serum (half-life time $t_{1/2}$ 0.64 h). Interestingly, extending the lipid chain from C14 to C18 prolonged the $t_{1/2}$ for PEG on the LNP surface up to 4.03 h.[64] This novel NMR method provides a way of studying the dynamics of PEG shedding ex vivo, allowing predictions of particle behavior in vivo. This will facilitate further understanding of the effect of structural variations in PEG-lipids as well as variations to the particle compositions, without the need for animal experiments. Extension of this method into more biologically relevant conditions would be required. It must be noted, that upon intravenous injection of LNPs, it would be expected that PEG shedding is more rapid due to the increased biological milieu.

Predictable in vivo RNA delivery is another highly desired structure−function correlation to be established for LNPs.[65,66] Whitehead et al. studied a large library of 1400 biodegradable lipidoids as potent carriers for siRNA in vivo.[65] Prior to in vivo experiments, an extended in vitro screening of siRNA delivery by LNPs was conducted. The study was carried out in HeLa cells expressing two reporter proteins, firefly and Renilla luciferase. Reduced luciferase activity indicated toxicity associated with the LNP, those of which were not considered for further studies. Of the entire library, 82 LNP formulations were found to be highly toxic, reducing luciferase activity by over 50%. Next, according to an in vitro study, C12 and C13 fatty acids were abundant in the successful LNP population. Moreover, tertiary and secondary amines, alcohols, and branched or linear chains conferred efficacy, while ethers and rings did not, except amine-containing piperazine. The most potent LNPs successfully silenced Factor VII blood clotting factor and CD45 tyrosine phosphatase protein in vivo. These particles contained three or more C13 fatty acids per LNP, and over 50% contained a tertiary amine group in the lipid structure. A second-generation LNP library confirmed these efficacy criteria for siRNA delivery into human hepatocytes and immune cells.[65]

Optimizing LNPs for mRNA delivery has been approached by Areta et al.[66] DLin-MC3-DMA-based LNPs were loaded with human erythropoietin mRNA, leading to NPs of 45 to 135 nm in diameter, corresponding to a DMPE-PEG content from 3 to 0.25 mol %, respectively. Cryo-TEM revealed details on the morphology of the LNPs. As above,[63] adding RNA shaped the LNP structure, leading to less structural variants than in the absence of the payload.[66] Rigid cylinder packing and nonspherical modality have been observed for the mRNA-LNPs in aqueous media. Phospholipid DSPC was located mainly on the surface, as in the previous NMR study.[63] LNP composition has been further optimized with regard to the DLin-cholesterol ratio, to achieve LNPs with a surface area per DSPC molecule of 1.2 $nm^2$. This resulted in maximum protein expression in human adipocytes and hepatocytes in vitro. LNPs with this surface area showed the highest protein production in vitro, especially at an NP size of 100 nm.[66] Regarding the optimal particle size of LNPs for RNA delivery,


DOI: 10.1021/acs.molpharmaceut.8b01290
Mol. Pharmaceutics 2019, 16, 2265−2277

there are contradictory results in the literature. Akinc et al. reported that in vivo efficacy of siRNA-lipidoid formulations increased with decreasing particle size.[67] In contrast, Bao et al. showed that the largest siRNA-LNPs resulted in the highest gene silencing activity in vivo.[68] More recently, Chen et al. identified siRNA-LNPs of 78 nm displaying the highest hepatic gene silencing in vivo.[69] This inconsistency, highlighted by Areta et al.[66] above, demonstrates that particle size alone may not be the only determinant for transfection efficiency. Rather, there is a dependence on particle size and particle surface composition. The latter being particularly prominent in the release of RNA from the endosomal compartment.

The work by Alabi et al.[70] brings in the p$K_a$ as one of key determinants in LNPs fate in vivo. Indeed, only 5−10% RNA payload escape endosomes when special repercussions are not taken.[65,66] Aiding endosomal escape by adjusting the p$K_a$ of a phospholipid formulation is an important screening parameter that was proven to enhance siRNA delivery in vivo and in vitro.[70] Extensive structure−function assessment led to the realization that including ionizable cationic lipids, with an optimal p$K_a$ 6.2−6.4, resulted in long-circulating liposomes, in vitro luciferase silencing in HeLa cells, and in vivo mouse factor VII silencing.[70,71] The ionizable nature of the lipid allows for LNP formation with anionic RNA at low pH, where the lipids possess an overall cationic charge. The overall pKa allows the lipid to remain deprotonated during circulation, reducing nonspecific cell interaction and subsequent early release of RNA cargo. While allowing protonation in the early or late endosome, which is necessary for facilitating membrane fusion and lipid mixing with the anionic lipids in the endosomal membrane.[20]

There are three major aspects that are missing in many early works on LNPs which may have contributed to clinical trial terminations, (1) structure of LNPs, (2) correlation between in vitro and in vivo performance, and (3) delivery to a broad range of cells and tissues outside the liver, rather than focusing on the natural accumulation in hepatocytes. Novel strategies incorporate encoding elements into the LNP design to facilitate the simultaneous assessment of multiple factors in LNP structure and performance. Such an approach, pioneered by Dahlman et al., utilizes DNA oligonucleotide barcodes packaged within the LNPs to measure the biodistribution of distinct LNPs to different cells and tissues.[72,73] Initially, Dahlman et al. chose to systematically vary three factors of one component in the LNP structure and their influence on biodistribution, the PEG tail length, PEG molecular weight (MW), and PEG mol.% in formulation, before proceeding to a larger study comparing the correlation between delivery efficiency in vitro to in vivo.[72,73] The highlight of this study is that LNP delivery in vitro is a poor predictor of delivery in vivo, and as such, the gold standard in vitro screening approach needs to shift to in vivo screening. A further study by Dalhman et al. focused on screening for LNPs with functional mRNA delivery to nonliver tissues.[74] A discrepancy exists between biodistribution of LNPs and functional delivery of mRNA, as 96% of delivered RNA does not escape the endosome.[75,76] This may vary with cell type or disease state. Hence, it becomes difficult to predict functional delivery based on particle biodistribution. Dalhman et al. chose to use a Cre-Lox system in mice, which allowed quantification of functional, cytosolic delivery of mRNA in vivo. Specifically, two LNPs (7C2 and 7C3) were identified out of >250, that efficiently deliver siRNA, sgRNA, and mRNA to endothelial cells.[74] There are still aspects missing from the screening strategies implemented here. For instance, the development and inclusion of high-throughput techniques for characterizing LNPs in terms of zeta-potential, p$K_a$, and lipid bilayer structure. The implementation of further characterization in the screening pipeline would facilitate advances in structure−activity relationships for nonliver tissues. These three studies highlight the necessity for an encoding system in high-throughput LNP assessment to elucidate fundamental understanding of the complex interplay between NP structural properties and delivery in vivo.

Tang et al. proposed a screening of the NP library with regard to interaction with immune cells as an early selection criteria for small molecules, to avoid toxicity in vivo.[77] Using an atherosclerosis model, 17 NP formulations were tested by the factor of inducing cholesterol efflux. Decorating NPs with protein APOA1 remarkably increased cholesterol efflux by the NPs. Besides this, phospholipid and core composition of NPs had an effect on the performance in vivo, with POPC dominant, 30 nm size spherical LNPs being the most effective and least toxic.[77] The authors hypothesize that particles with a small size combined with a long blood half-life promoted retention in atherosclerotic plaque macrophages. The fine-tuning of the LNP components and synthesis procedures improved the therapeutic index of a immunomodulatory molecule by favoring the delivery to aortic macrophages, rather than to splenic macrophages or the liver, which clear NPs from the blood and therefore reduce the bioavailability. This strategy of immunological screening using a combinatorial NP library may allow improvement in the precision of immunotherapies through tissue- and cell-specific delivery and the development of tailored nanotherapies for inflammatory diseases.

**Delivery of LNP.** Following an effective structure optimization, further improvement of the LNP can be achieved via surface decoration with specific ligands. The first generation of LNPs was limited to delivery via passive targeting, often utilizing the enhanced permeability and retention effect (EPR), a phenomenon occurring in solid tumors and infarcted areas associated with sites of inflammation and hypoxia.[78] Doxil, the first FDA-approved liposomal formulation of doxorubicin, incorporated a PEG coating to provide a steric shield for avoiding clearance by the reticuloendothelial system (RES) and allowing greater circulation time following intravenous administration.[79] The EPR effect is now considered the primary mechanism for the passive accumulation of NPs in tumors in vivo.[55] Likewise, the liver also accumulates NPs in a manner similar to the EPR effect. Once retained in the liver, NPs interact with hepatocytes, endothelial cells, B cells, and Kupffer cells. All of which become a major barrier when the objective is delivery to nonliver tissues or cells. A more desirable delivery approach would involve surface modification of the NP to promote delivery in a tissue or cell-specific manner in vivo. Improved delivery of LNPs would minimize nonspecific side effects (both on neighboring cells and systemically) and would reduce the nucleic acid payload.[80,81] Preferential tissue/cell retention may be achieved by conjugating various targeting moieties to the NP surface. Initially, LNPs primarily utilized antibodies as the targeting moiety, due to their high specificity and availability.[82] Since then, various other targeting moieties have been explored, including peptides, proteins, small molecule ligands, aptamers, antigen-binding (Fab) fragments, and single-chain variable


DOI: 10.1021/acs.molpharmaceut.8b01290
Mol. Pharmaceutics 2019, 16, 2265−2277

fragments (scFv).[83] The type of moiety is not the only determinant in targeting functionality, as the size, charge, density, and orientation also contribute to the overall efficacy.

The literature reports a mixture of responses from the use of ligands for LNP modification and their influence on biodistribution or pharmacokinetic profile. Some report no influence; whereas others suggest an improvement.[83] Nonetheless, receptor-mediated endocytosis using targeting ligands is the primary contributor to enhanced therapeutic response, via increasing internalization by target cells.[84,85] A success story in antibody-mediated targeting has been reported in gene silencing, whereby liposomes containing CCR5 siRNA, decorated with lymphocyte function-associated antigen-1 (LFA-1) antibodies, reported delivery to T cells and macrophages and overall protection from HIV infection in mice.[86] However, there are considerations that need to be addressed with the use of LFA-1 antibodies for this approach, as leukocyte adhesion may be blocked and result in the silencing of pro-inflammatory molecules.[87] More recently, Ramshetti et al. reported specific binding, uptake, and silencing of CD45 in murine T lymphocytes following IV injection, using anti-CD4 mAb-targeted LNPs.[88] Even at a low dose, effective T cell silencing was observed in the blood, spleen, bone marrow, and inguinal lymph nodes.

For B cell malignancy, anti-CD38 mAb-modified LNPs achieved specific uptake in human mantle cell lymphoma cells (MCL) in the bone marrow of xenografted mice. In vitro studies demonstrated specific delivery of siRNA against cyclin D1 (siCycD1) to B cells. However, it must be noted, that gene silencing of CycD1 was not successfully demonstrated in a direct manner in vivo. Rather, an overall survival benefit was observed for mice treated with the anti-CD38-LNP-siCycD1.[89] Moreover, LNPs have been functionalized with hyaluronan (HA), a natural ligand for the CD44 receptor. CD44 is overexpressed on the surface of multiple cancer cell types. HA-decorated LNPs delivered siRNA cargo locally to glioblastoma multiforme (GBM) cells in a murine xenograft model, significantly prolonging survival of treated mice.[90] In fact, this was the longest reported survival of mice in this type of GBM model and shows promise for the use of therapeutic siRNAs in localized treatments for GBM.

Returning to the functionality of ligands, their orientation on the LNP is a key factor. This is particularly relevant for monoclonal antibodies (mAb), where the accessibility of the Fab is required for full biofunctionality. It is becoming increasingly evident that conventional covalent immobilization techniques, e.g., using EDC/NHS, are ineffective at directional coupling, due to nonspecific interactions with multiple reactive sites on the protein.[91,92] The lack of directionality in mAb immobilization has been addressed by Jeong et al., whereby orientation-controlled antibody conjugation was achieved using copper-free click chemistry.[93] A modular platform for targeted RNAi therapeutics has recently been developed by Kedmi et al., whereby LNPs are functionalized with targeting antibodies via a recombinant protein, named anchored secondary scFv enabling targeting (ASSET).[94] This platform has since been used for the cell-specific delivery of mRNA to leukocytes in mice, representing a flexible platform that may have great potential in precision medicine.[95]

Nucleic acid aptamers offer several advantages over their antibody counterparts regarding targeting functionality. Aptamers are smaller, lack immunogenicity, have higher stability, and show versatility in chemical production and modification.[96] Upon binding to cell-surface receptors, most aptamers undergo internalization, which makes them ideal targeting moieties for oligonucleotides, i.e., siRNA and miRNA. However, clinical development of therapeutic aptamers is still far behind that of monoclonal antibodies. A recent termination of a phase III clinical trial of an anticoagulant aptamer against factor IXa[97] exemplifies this and indicates that it will still be some time before clinically effective aptamers are developed for use in NP targeting.

Alternate examples of ligands for LNP decoration are GalNAc, which has a high affinity for the asialoglycoprotein receptor on hepatocytes;[98] ApoE lipoprotein, which facilitates receptor-mediated endocytosis into hepatocytes;[98] as well as folate and transferrin for targeting cancer cells.[99,100] Recently, a novel targeted liposomal formulation, utilizing a folate-containing lipoconjugate (FC) and PEG spacer, has been investigated for nucleic acid delivery to folate receptor (FR)-expressing tumor cells.[101] These liposomes were formed under low N/P conditions which favored a reduced cytotoxicity and resulted in enhanced transfection efficiency, both in vitro and in vivo, in comparison to the untargeted formulation. Furthermore, polypeptide pPB-modified stable nucleic acid lipid NPs (pPB-SNALPs) have been reported to selectively deliver siRNA against heat shock protein 47 (Hsp47) to the liver, which has shown efficacy for the targeted therapy of hepatic fibrosis.[102] These modified SNALPs displayed increased uptake by hepatic stellate cells of mice in vitro and in vivo, indicating an effective liver-targeting delivery system. Again, the "liver-targeting" effect observed here is facilitated by the natural hepatic accumulation following intravenous administration. Nevertheless, the current antifibrotic drug treatment is ineffective at liver targeting, so there is promise for the use of modified nucleic acid-LNPs for hepatic fibrosis.

There is currently a bottleneck in the translation of nucleic acid-LNP therapies from clinical trials to products on the market, despite immense effort. Such therapies rely on the establishment of product safety, stability, and performance in vivo that has yet to be achieved. Further assessment is required to characterize and comprehend the particle physicochemical properties, in terms of composition, size, morphology, polydispersity, surface properties, and serum stability, and their biological fate.[103] The cytotoxicity and innate immune activation associated with the use of cationic LNPs has also represented a major barrier in the clinical translation. The utilization of ionizable and PEGylated lipids has to some extent addressed the issues of immunogenicity and mononuclear phagocyte system (MPS) clearance. However, studying the in vivo fate of particles relies on animal models which may not be so feasibly extrapolated to humans.[25] Additionally, production and formulation conditions, as well as storage conditions, are an essential factor in robust and reproducible manufacturing.[25]

**Toward Mass Production of Therapeutic LNP.** When the LNP formulation has been optimized and tested in vitro and in vivo, the next preclinical step requires extended studies. To perform these studies, large amounts of RNA LNP drug candidate are needed. Currently, large-scale synthesis of LNPs is complicated and expensive. Synthesis optimization is therefore a crucial obstacle for RNA LNPs to be overcome in the upcoming years. Having on-hand a high quality, large scale RNA drug, short or long, and LNP formulations is an objective of ongoing work in both academia and industry. Today, up to 10 g of RNA synthesis can be performed.[104] The synthesis applies a solid-phase phosphoramidite chemistry,


DOI: 10.1021/acs.molpharmaceut.8b01290
Mol. Pharmaceutics 2019, 16, 2265−2277

which allows for controlled incorporation of additional modifications, such as LNA, 2′-OMe RNA, 2′-F-RNA, etc. GMP grade RNA LNPs can be further obtained in specialized synthesis units.[105,106] Patisiran, the FDA approved siRNA therapeutic mentioned above, requires systemic administration at a dose of 0.3 mg/kg. Therapeutic mRNA, on the other hand, can be 100 times larger than a single siRNA duplex. mRNA production is currently carried out by a labor- and reagent-demanding cloning-expression approach.[107] Due to complicated, multistep preparation, the price of mRNA drug candidates is high, and the availability of certain modifications is limited. To address this issue, improved synthetic work flows are being explored.[108,109]

Conventional methods of LNP production, e.g., lipid-film hydration and ethanol injection, despite issues in reproducibility and scalability, have, until recently, been the primary technique utilized.[110] These drawbacks stimulated development of improved production strategies, based on the ethanol injection method. T-junction mixing for lipid-based drug delivery was pioneered in 1999 as a technique for production of DNA-lipoplexes, which provided a controlled mixing environment and resulted in reproducible production.[111] Since then, techniques utilizing microfluidic mixing have been used to encapsulate mRNA, siRNA, and pDNA in LNPs. This has revolutionized LNP production for scalability and reproducibility.[112] Microfluidic hydrodynamic focusing (MHF) and staggered herringbone mixing (SHM) represent the forefront in this technology.[113,114] The controlled rapid mixing of two miscible phases, lipids in ethanol and nucleic acids in aqueous buffer, defined by the total flow rate (volume/time) and FRR (ratio of aqueous-to-organic flow rate) allow the resulting particle size and distribution (PDI) to be well-defined.[115] Microfluidic chips may be designed so that the LNP morphology is predetermined and may be tailored to the application. Chips may also be parallelized in SHM to enable up-scaling of LNP production.[41,116]

Fang et al. reported large-scale synthesis of lipid NPs using a multi-inlet vortex reactor (MIVR) (Figure 3).[117] The MIVR device differs from previously reported microfluidic and sonication methods. It consists of either two or four radially symmetric inlets connected to circular reaction chamber. The device mixes an organic phase containing polymers and an aqueous phase, which acts as an antisolvent. Using the MIVR, up to 50 mL of LNP formulation, with a concentration of 2.5 mg/mL, can be produced only in one minute. The authors state that their methodology can be extended to a broad range of loaded LNPs, including RNA LNP, without dramatic reduction in product parameters.[117]

Kim et al. developed an approach for mass production of LNPs with a yield over 3 g per hour.[118] This is approximately 1000 times faster than that of existing microfluidic devices. The principle behind the technique is based on creating symmetric microflow rates by 3D focusing of reagents in selected solvents, which occurs within a simple three-inlet chamber. The particle size can be readily controlled by adjusting the flow rate for the reagents. The reproducibility of the technique is also extraordinary, with a PDI < 0.1 being achieved in over an 100 g production scale.[118]

## CONCLUSION AND FUTURE DIRECTIONS

There is great promise for the future development of LNPs for RNA therapeutics. The development of large-scale, reproducible production of LNPs and their payloads[41,111−116] in clinically relevant quantities could enable a shift of focus in drug development toward RNA therapeutics. Besides offering more material for trials, reducing the cost of RNA LNP drugs would make therapy more accessible to a larger group of patients. The incorporation of target-specific ligands into the LNP formulation, such as monoclonal antibodies or natural ligands, is expected to improve the safety profile of RNA therapeutics by reducing off-target effects and allowing cell-specific interaction, which has promoted the development of effective in vivo administration approaches. However, there is still a need to incorporate aspects of LNP functionalization into the synthesis process to allow reproducible preparation of targeted LNP formulations.

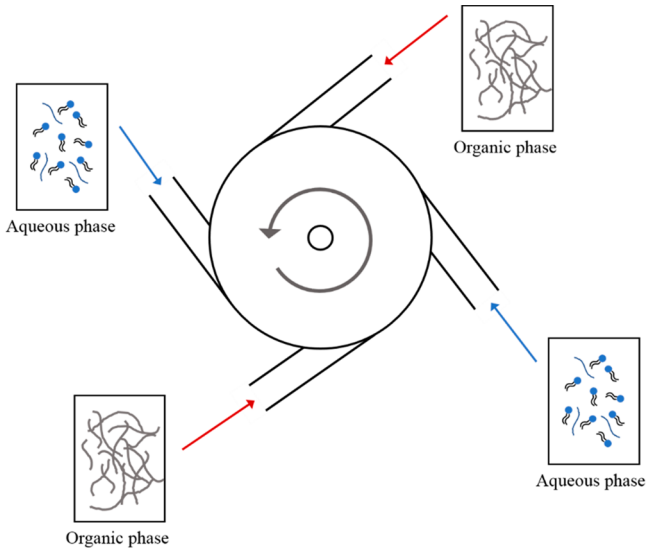


**Figure 3.** Diagrammatic working mechanism of an MIVR device for the synthesis of lipid−polymer hybrid NPs.[117] The organic phase may contain dissolved polymer, and the aqueous phase may contain a lipid/lipid−PEG mixture. The four separate streams are directed into a circular reaction chamber which facilitates the self-assembly of NPs, which are collected from the outlet.

Recent developments in RNA-LNP therapeutics have been translated into several clinical trials, albeit with many challenges. Advances in high-throughput LNP screening and structural characterization approaches have broadened our understanding of the complex macromolecular interactions governing the delivery and efficacy of gene-therapeutics. However, the in vivo fate still needs further clarification for the full therapeutic potential of RNA oligonucleotides to be realized. RNA therapeutics has the potential to expand the range of druggable targets for multiple disease types and synergize with existing therapies to provide novel therapeutic approaches for currently untreatable diseases. In the field of cancer immunotherapy, which is currently dominated by antibodies, small molecules, and engineered T cells, there is still a need for efficacy improvement. CRISPR/Cas is a recently proposed gene editing mechanism that, in order to become an efficacious therapeutic tool, still requires an effective delivery system. Several reports apply LNPs for encapsulating components of the CRISPR/Cas complex, with already positive results achieved in vivo.[56,57,119] Large off target effects and poor cellular uptake of CRISPR/Cas components are crucial issues to be addressed in the future. Personalized cancer vaccines are another emerging direction for RNA lipoplexes and RNA LNPs. Successful trials have been


DOI: 10.1021/acs.molpharmaceut.8b01290
Mol. Pharmaceutics 2019, 16, 2265−2277

performed for several RNA vaccines and have been brought into clinical testing, e.g., Lipo-MERIT and mRNA 2416. Developing more vaccines, both in a therapeutic or prophylactic sense, would be a way to approach cancer in a preventive way, which has not been possible up until now.

## AUTHOR INFORMATION


### Corresponding Authors

*E-mail: kiraas@kemi.dtu.dk.
*E-mail: marita@kemi.dtu.dk.

### ORCID

Kira Astakhova: 0000-0003-4878-0301
Maria Taskova: 0000-0002-9727-2496


### Notes

The authors declare no competing financial interest.

## ACKNOWLEDGMENTS

We acknowledge the Villum Foundation (award 13152), National Institutes of Health USA (NIH 1R01MH113407-01), and ERC-2017-PoC (CodeSphere 767882) for financial support.

## ABBREVIATIONS

ApoE, apolipoprotein E; AS, antisense; ASO, antisense oligonucleotide; ASSET, anchored secondary scFv enabling targeting; Cas9, CRISPR-associated protein 9; CCR5, C−C chemokine receptor type 5; CD, cluster of differentiation; CML, chronic myelogenous leukemia; CRISPR, clustered regularly short palindromic repeats; CRS, cytokine release syndrome; CSAL, cationic quaternary ammonium sulfonamide amino lipids; DLinDMA, 1,2-dilinoleyloxy-*N*,*N*-dimethyl-3-aminopropane; DMD, duchenne muscular dystrophy; DMPE, 1,2-dimyristoyl-sn-glycero-3-phosphoethanolamine; DNA, deoxyribonucleic acid; DODAP, 1,2-dioleoyl-3-dimethylammonium-propane; DOPE, 1,2-dioleoyl-sn-glycero-3-phosphoethanolamine; DOTMA, 1,2-di-*O*-octadecenyl-3-trimethylammonium propane; DSPC, phosphatidylcholine; EDC, 1-ethyl-3-(3-dimethylaminopropyl)carbodiimide; EphA2, ephrin type-A receptor 2; EPR, enhanced permeability and retention effect; Fab, antigen-binding fragment; FR, folate receptor; GalNAc, *N*-acetylgalactosamine; HA, hyaluronan; Hsp47, heat shock protein 47; IgM, immunoglobulin M; LFA-1, lymphocyte function-associated antigen-1; LNP, lipid NP; LUNAR, lipid-enabled and unlocked nucleic-acid-modified RNA; mAb, monoclonal antibody; MAPK, mitogen-activated protein kinase; MCL, mantle cell lymphoma; MHF, microfluidic hydrodynamic focusing; MIVR, multi-inlet vortex reactor; mRNA, messenger RNA; NHS, *N*-hydroxysuccinimide; NHP, nonhuman primates; NMR, nuclear magnetic resonance; NP, nanoparticle; OFAT, one-factor-at-a-time; ON, oligonucleotide; PAM, polyamidoamine dendrimers; PDI, polydispersity index; PEG, polyethylene glycol; PEI, polyethyleneimine; PH1, primary hyperoxaluria 1; PLGA, poly(lactic-co-glycolic) acid; PMO, phosphorodiamidate morpholino oligomer; PRR, pattern-recognition receptors; PS, phosphorothioate; RES, reticuloendothelial system; RIG-I, retinoic acid-inducible gene I; RNA, ribonucleic acid; siCycD1, siRNA against cyclin D1; scFv, single-chain variable fragment; sgRNA, single-guide RNA; SHM, staggered herringbone mixing; siRNA, small interfering RNA; SNALP, stable nucleic acid lipid NPs; SSO, splice switching oligo; T cell, T lymphocyte; TEM, transmission electron microscopy; TLR, toll-like receptor

## REFERENCES


(1) Stein, C. A.; Castanotto, D. FDA-Approved Oligonucleotide Therapies in 2017. *Mol. Ther.* **2017**, *25* (5), 1069−1075.
(2) Martinovich, K. M.; Shaw, N. C.; Kicic, A.; Schultz, A.; Fletcher, S.; Wilton, S. D.; Stick, S. M. The Potential of Antisense Oligonucleotide Therapies for Inherited Childhood Lung Diseases. *Mol. Cell. Pediatr.* **2018**, *5* (1), 3.
(3) Lim, K. R. Q.; Maruyama, R.; Yokota, T. Eteplirsen in the Treatment of Duchenne Muscular Dystrophy. *Drug Des., Dev. Ther.* **2017**, *11*, 533−545.
(4) Khalil, I. A.; Yamada, Y.; Harashima, H. Optimization of siRNA Delivery to Target Sites: Issues and Future Directions. *Expert Opin. Drug Delivery* **2018**, *15* (11), 1053−1065.
(5) Adams, D.; Gonzalez-Duarte, A.; O'Riordan, W. D.; Yang, C.-C.; Ueda, M.; Kristen, A. V.; Tournev, I.; Schmidt, H. H.; Coelho, T.; Berk, J. L.; et al. Patisiran, an RNAi Therapeutic, for Hereditary Transthyretin Amyloidosis. *N. Engl. J. Med.* **2018**, *379* (1), 11−21.
(6) Pastor, F.; Berraondo, P.; Etxeberria, I.; Frederick, J.; Sahin, U.; Gilboa, E.; Melero, I. An Rna Toolbox for Cancer Immunotherapy. *Nat. Rev. Drug Discovery* **2018**, *17* (10), 751−767.
(7) Shen, X.; Corey, D. R. Chemistry, Mechanism and Clinical Status of Antisense Oligonucleotides and Duplex RNAs. *Nucleic Acids Res.* **2018**, *46* (4), 1584−1600.
(8) Palmerston Mendes, L.; Pan, J.; Torchilin, V. Dendrimers as Nanocarriers for Nucleic Acid and Drug Delivery in Cancer Therapy. *Molecules* **2017**, *22* (9), 1401.
(9) Lallana, E.; Rios De La Rosa, J. M.; Tirella, A.; Pelliccia, M.; Gennari, A.; Stratford, I. J.; Puri, S.; Ashford, M.; Tirelli, N. Chitosan/Hyaluronic Acid Nanoparticles: Rational Design Revisited for RNA Delivery. *Mol. Pharmaceutics* **2017**, *14* (7), 2422−2436.
(10) Thomas, T. J.; Tajmir-Riahi, H. A.; Thomas, T. Polyamine-DNA Interactions and Development of Gene Delivery Vehicles. *Amino Acids* **2016**, *48* (10), 2423−2431.
(11) Felgner, P. L.; Gadek, T. R.; Holm, M.; Roman, R.; Chan, H. W.; Wenz, M.; Northrop, J. P.; Ringold, G. M.; Danielsen, M. Lipofection: A Highly Efficient, Lipid-Mediated DNA-Transfection Procedure. *Proc. Natl. Acad. Sci. U. S. A.* **1987**, *84* (21), 7413−7417.
(12) Dwarki, V. J.; Malone, R. W.; Verma, I. M. Cationic Liposome-Mediated RNA Transfection. *Methods Enzymol.* **1993**, *217* (C), 644−654.
(13) Gao, H.; Hui, K. M. Synthesis of a Novel Series of Cationic Lipids That Can Act as Efficient Gene Delivery Vehicles through Systematic Heterocyclic Substitution of Cholesterol Derivatives. *Gene Ther.* **2001**, *8* (11), 855−863.
(14) Zhang, J.; Fan, H.; Levorse, D. A.; Crocker, L. S. Interaction of Cholesterol-Conjugated Ionizable Amino Lipids with Biomembranes: Lipid Polymorphism, Structure-Activity Relationship, and Implications for siRNA Delivery. *Langmuir* **2011**, *27* (15), 9473−9483.
(15) Wasungu, L.; Hoekstra, D. Cationic Lipids, Lipoplexes and Intracellular Delivery of Genes. *J. Controlled Release* **2006**, *116* (2), 255−264.
(16) Floch, V.; Loisel, S.; Guenin, E.; Hervé, A. C.; Clément, J. C.; Yaouanc, J. J.; Des Abbayes, H.; Férec, C. Cation Substitution in Cationic Phosphonolipids: A New Concept To Improve Transfection Activity and Decrease Cellular Toxicity. *J. Med. Chem.* **2000**, *43* (24), 4617−4628.
(17) Farhood, H.; Gao, X.; Son, K.; Lazo, J. S.; Huang, L.; Barsoum, J.; Bottega, R.; Epand, R. M. Cationic Liposomes for Direct Gene Transfer in Therapy of Cancer and Other Diseases. *Ann. N. Y. Acad. Sci.* **1994**, *716*, 23−35.
(18) Hafez, I.; Maurer, N.; Cullis, P. On the Mechanism Whereby Cationic Lipids Promote Intracellular Delivery of Polynucleic Acids. *Gene Ther.* **2001**, *8* (15), 1188−1196.
(19) Felgner, J. H.; Kumar, R.; Sridhar, C. N.; Wheeler, C. J.; Tsai, Y. J.; Border, R.; Ramsey, P.; Martin, M.; Felgner, P. L. Enhanced Gene Delivery and Mechanism Studies with a Novel Series of



DOI: 10.1021/acs.molpharmaceut.8b01290
*Mol. Pharmaceutics* 2019, 16, 2265−2277

Cationic Lipid Formulations. *J. Cell. Biochem. Suppl.* **1994**, *269* (4), 2550.
(20) Kanasty, R.; Dorkin, J. R.; Vegas, A.; Anderson, D. Delivery Materials for siRNA Therapeutics. *Nat. Mater.* **2013**, *12* (11), 967−977.
(21) Jones, C. H.; Chen, C.-K.; Ravikrishnan, A.; Rane, S.; Pfeifer, B. A. Overcoming Nonviral Gene Delivery Barriers: Perspective and Future. *Mol. Pharmaceutics* **2013**, *10* (11), 4082−4098.
(22) Lin, P. J. C.; Tam, Y. Y. C.; Hafez, I.; Sandhu, A.; Chen, S.; Ciufolini, M. A.; Nabi, I. R.; Cullis, P. R. Influence of Cationic Lipid Composition on Uptake and Intracellular Processing of Lipid Nanoparticle Formulations of siRNA. *Nanomedicine* **2013**, *9* (2), 233−246.
(23) Liu, D.; Hu, I.; Qiao, W.; Li, Z.; Zhan, S.; Cheng, L. Synthesis and Characterization of a Series of Carbamate-Linked Cationic Lipids for Gene Delivery. *Lipids* **2005**, *40* (8), 839−848.
(24) Cardarelli, F.; Digiacomo, L.; Marchini, C.; Amici, A.; Salomone, F.; Fiume, G.; Rossetta, A.; Gratton, E.; Pozzi, D.; Caracciolo, G. The Intracellular Trafficking Mechanism of Lipofectamine-Based Transfection Reagents and Its Implication for Gene Delivery. *Sci. Rep.* **2016**, *6* (1), 25879.
(25) Rietwyk, S.; Peer, D. Next-Generation Lipids in RNA Interference Therapeutics. *ACS Nano* **2017**, *11* (8), 7572−7586.
(26) Crucho, C. I. C. Stimuli-Responsive Polymeric Nanoparticles for Nanomedicine. *ChemMedChem* **2015**, *10* (1), 24−38.
(27) Bulbake, U.; Doppalapudi, S.; Kommineni, N.; Khan, W. Liposomal Formulations in Clinical Use: An Updated Review. *Pharmaceutics* **2017**, *9* (2), 12.
(28) Landesman-Milo, D.; Peer, D. Toxicity Profiling of Several Common RNAi-Based Nanomedicines: A Comparative Study. *Drug Delivery Transl. Res.* **2014**, *4* (1), 96−103.
(29) Peer, D. Immunotoxicity Derived from Manipulating Leukocytes with Lipid-Based Nanoparticles. *Adv. Drug Delivery Rev.* **2012**, *64* (15), 1738−1748.
(30) Litzinger, D. C. Limitations of Cationic Liposomes for Antisense Oligonucleotide Delivery in Vivo. *J. Liposome Res.* **1997**, *7* (1), 51−61.
(31) McLean, J. W.; Fox, E. A.; Baluk, P.; Bolton, P. B.; Haskell, A.; Pearlman, R.; Thurston, G.; Umemoto, E. Y.; McDonald, D. M. Organ-Specific Endothelial Cell Uptake of Cationic Liposome-DNA Complexes in Mice. *Am. J. Physiol.* **1997**, *273* (1), 387.
(32) Martin, B.; Sainlos, M.; Aissaoui, A.; Oudrhiri, N.; Hauchecorne, M.; Vigneron, J.; Lehn, J.; Lehn, P. The Design of Cationic Lipids for Gene Delivery. *Curr. Pharm. Des.* **2005**, *11* (3), 375−394.
(33) Filion, M. C.; Phillips, N. C. Toxicity and Immunomodulatory Activity of Liposomal Vectors Formulated with Cationic Lipids toward Immune Effector Cells. *Biochim. Biophys. Acta, Biomembr.* **1997**, *1329* (2), 345−356.
(34) Asai, T.; Oku, N. Systemic Delivery of Small RNA Using Lipid Nanoparticles. *Biol. Pharm. Bull.* **2014**, *37* (2), 201−205.
(35) Lee, D. W.; Gardner, R.; Porter, D. L.; Louis, C. U.; Ahmed, N.; Jensen, M.; Grupp, S. A.; Mackall, C. L. Current concepts in the diagnosis and management of cytokine release syndrome. *Blood* **2014**, *124* (2), 188−196.
(36) Kranz, L. M.; Diken, M.; Haas, H.; Kreiter, S.; Loquai, C.; Reuter, K. C.; Meng, M.; Fritz, D.; Vascotto, F.; Hefesha, H.; et al. Systemic RNA Delivery to Dendritic Cells Exploits Antiviral Defence for Cancer Immunotherapy. *Nature* **2016**, *534* (7607), 396−401.
(37) Verbeke, R.; Lentacker, I.; Wayteck, L.; Breckpot, K.; Van Bockstal, M.; Descamps, B.; Vanhove, C.; De Smedt, S. C.; Dewitte, H. Co-Delivery of Nucleoside-Modified mRNA and TLR Agonists for Cancer Immunotherapy: Restoring the Immunogenicity of Immunosilent mRNA. *J. Controlled Release* **2017**, *266*, 287−300.
(38) Hirsova, P.; Ibrahim, S. H.; Krishnan, A.; Verma, V. K.; Bronk, S. F.; Werneburg, N. W.; Charlton, M. R.; Shah, V. H.; Malhi, H.; Gores, G. J. Lipid-Induced Signaling Causes Release of Inflammatory Extracellular Vesicles From Hepatocytes. *Gastroenterology* **2016**, *150* (4), 956−967.
(39) Kubota, K.; Onishi, K.; Sawaki, K.; Li, T.; Mitsuoka, K.; Sato, T.; Takeoka, S. Effect of the nanoformulation of siRNA-lipid assemblies on their cellular uptake and immune stimulation. *Int. J. Nanomed.* **2017**, *12*, 5121−5133.
(40) Sedic, M.; Senn, J. J.; Lynn, A.; Laska, M.; Smith, M.; Platz, S. J.; Bolen, J.; Hoge, S.; Bulychev, A.; Jacquinet, E.; et al. Safety Evaluation of Lipid Nanoparticle-Formulated Modified mRNA in the Sprague-Dawley Rat and Cynomolgus Monkey. *Vet. Pathol.* **2018**, *55* (2), 341−354.
(41) Belliveau, N. M.; Huft, J.; Lin, P. J.; Chen, S.; Leung, A. K.; Leaver, T. J.; Wild, A. W.; Lee, J. B.; Taylor, R. J.; Tam, Y. K.; et al. Microfluidic Synthesis of Highly Potent Limit-Size Lipid Nanoparticles for in Vivo Delivery of siRNA. *Mol. Ther.–Nucleic Acids* **2012**, *1*, e37.
(42) Clamme, J.-P.; Yu, L.; Liu, Y.; Mahato, R. I.; Liu, J.; Bao, Y.; Ying, W.; Chivukula, P.; Ng, D.; Jin, Y.; et al. Effect of PEGylation on Biodistribution and Gene Silencing of siRNA/Lipid Nanoparticle Complexes. *Pharm. Res.* **2013**, *30* (2), 342−351.
(43) Johnston, B.; Kolli, S.; Thanou, M.; Wong, S.-P.; Miller, A. D.; Harbottle, R. pH-Triggered Nanoparticle Mediated Delivery of siRNA to Liver Cells in Vitro and in Vivo. *Bioconjugate Chem.* **2013**, *24* (3), 314−332.
(44) Tam, Y. Y. C.; Chen, S.; Cullis, P. R. Advances in Lipid Nanoparticles for siRNA Delivery. *Pharmaceutics* **2013**, *5* (3), 498−507.
(45) La-Beck, N. M.; Gabizon, A. A. Nanoparticle Interactions with the Immune System: Clinical Implications for Liposome-Based Cancer Chemotherapy. *Front. Immunol.* **2017**, *8*, 6−11.
(46) Lin, S. Y.; Zhao, W. Y.; Tsai, H. C.; Hsu, W. H.; Lo, C. L.; Hsiue, G. H. Sterically Polymer-Based Liposomal Complexes with Dual-Shell Structure for Enhancing the siRNA Delivery. *Biomacromolecules* **2012**, *13* (3), 664−675.
(47) Abrams, M. T.; Koser, M. L.; Seitzer, J.; Williams, S. C.; Dipietro, M. A.; Wang, W.; Shaw, A. W.; Mao, X.; Jadhav, V.; Davide, J. P.; et al. Evaluation of Efficacy, Biodistribution, and Inflammation for a Potent siRNA Nanoparticle: Effect of Dexamethasone Co-Treatment. *Mol. Ther.* **2010**, *18* (1), 171−180.
(48) Michel, T.; Luft, D.; Abraham, M.-K. K.; Reinhardt, S.; Salinas Medina, M. L.; Kurz, J.; Schaller, M.; Avci-Adali, M.; Schlensak, C.; Peter, K.; et al. Cationic Nanoliposomes Meet mRNA: Efficient Delivery of Modified mRNA Using Hemocompatible and Stable Vectors for Therapeutic Applications. *Mol. Ther.–Nucleic Acids* **2017**, *8*, 459−468.
(49) Semple, S. C.; Klimuk, S. K.; Harasym, T. O.; Dos Santos, N.; Ansell, S. M.; Wong, K. F.; Maurer, N.; Stark, H.; Cullis, P. R.; Hope, M. J.; et al. Efficient Encapsulation of Antisense Oligonucleotides in Lipid Vesicles Using Ionizable Aminolipids: Formation of Novel Small Multilamellar Vesicle Structures. *Biochim. Biophys. Acta, Biomembr.* **2001**, *1510* (1−2), 152−166.
(50) Zimmermann, T. S.; Lee, A. C. H.; Akinc, A.; Bramlage, B.; Bumcrot, D.; Fedoruk, M. N.; Harborth, J.; Heyes, J. A.; Jeffs, L. B.; John, M.; et al. RNAi-Mediated Gene Silencing in Non-Human Primates. *Nature* **2006**, *441* (1), 111−114.
(51) Sah, D. W. Y.; Falzone, R.; Borland, T.; Perez, J.; Adams, D.; Chen, Q.; Hawkins, P. N.; Meyers, R. E.; Butler, J. S.; Munisamy, M.; et al. Safety and Efficacy of RNAi Therapy for Transthyretin Amyloidosis. *N. Engl. J. Med.* **2013**, *369* (9), 819−829.
(52) Maier, M. A.; Jayaraman, M.; Matsuda, S.; Liu, J.; Barros, S.; Querbes, W.; Tam, Y. K.; Ansell, S. M.; Kumar, V.; Qin, J.; et al. Biodegradable Lipids Enabling Rapidly Eliminated Lipid Nanoparticles for Systemic Delivery of RNAi Therapeutics. *Mol. Ther.* **2013**, *21* (8), 1570−1578.
(53) Yanagi, T.; Tachikawa, K.; Wilkie-Grantham, R.; Hishiki, A.; Nagai, K.; Toyonaga, E.; Chivukula, P.; Matsuzawa, S. Lipid Nanoparticle-Mediated siRNA Transfer Against PCTAIRE1/PCTK1/Cdk16 Inhibits In Vivo Cancer Growth. *Mol. Ther.–Nucleic Acids* **2016**, *5* (6), No. e327.
(54) Ramaswamy, S.; Tonnu, N.; Tachikawa, K.; Limphong, P.; Vega, J. B.; Karmali, P. P.; Chivukula, P.; Verma, I. M. Systemic


DOI: 10.1021/acs.molpharmaceut.8b01290
*Mol. Pharmaceutics* 2019, 16, 2265−2277

Delivery of Factor IX Messenger RNA for Protein Replacement Therapy. *Proc. Natl. Acad. Sci. U. S. A.* **2017**, *114* (10), E1941−E1950.
(55) Van Haute, D.; Berlin, J. O. Challenges in Realizing Selectivity for Nanoparticle Biodistribution and Clearance: Lessons from Gold Nanoparticles. *Ther. Delivery* **2017**, *8* (9), 763−774.
(56) Yin, H.; Song, C.-Q. Q.; Dorkin, J. R.; Zhu, L. J.; Li, Y.; Wu, Q.; Park, A.; Yang, J.; Suresh, S.; Bizhanova, A.; et al. Therapeutic Genome Editing by Combined Viral and Non-Viral Delivery of CRISPR System Components in Vivo. *Nat. Biotechnol.* **2016**, *34* (3), 328−333.
(57) Wang, M.; Zuris, J. A.; Meng, F.; Rees, H.; Sun, S.; Deng, P.; Han, Y.; Gao, X.; Pouli, D.; Wu, Q.; et al. Efficient Delivery of Genome-Editing Proteins Using Bioreducible Lipid Nanoparticles. *Proc. Natl. Acad. Sci. U. S. A.* **2016**, *113* (11), 2868−2873.
(58) Miller, J. B.; Kos, P.; Tieu, V.; Zhou, K.; Siegwart, D. J. Development of Cationic Quaternary Ammonium Sulfonamide Amino Lipids for Nucleic Acid Delivery. *ACS Appl. Mater. Interfaces* **2018**, *10* (3), 2302−2311.
(59) Colombani, T.; Peuziat, P.; Dallet, L.; Haudebourg, T.; Mével, M.; Berchel, M.; Lambert, O.; Habrant, D.; Pitard, B. Self-Assembling Complexes between Binary Mixtures of Lipids with Different Linkers and Nucleic Acids Promote Universal mRNA, DNA and siRNA Delivery. *J. Controlled Release* **2017**, *249*, 131−142.
(60) Kauffman, K. J.; Dorkin, J. R.; Yang, J. H.; Heartlein, M. W.; Derosa, F.; Mir, F. F.; Fenton, O. S.; Anderson, D. G. Optimization of Lipid Nanoparticle Formulations for mRNA Delivery in Vivo with Fractional Factorial and Definitive Screening Designs. *Nano Lett.* **2015**, *15* (11), 7300−7306.
(61) Oberli, M. A.; Reichmuth, A. M.; Dorkin, J. R.; Mitchell, M. J.; Fenton, O. S.; Jaklenec, A.; Anderson, D. G.; Langer, R.; Blankschtein, D. Lipid Nanoparticle Assisted mRNA Delivery for Potent Cancer Immunotherapy. *Nano Lett.* **2017**, *17* (3), 1326−1335.
(62) Patel, D.; Kesharwani, R.; Gupta, S. Development & Screening Approach for Lipid Nanoparticle: A Review. *Asian J. Pharm. Res. Dev.* **2015**, *3* (6), 1.
(63) Viger-Gravel, J.; Schantz, A.; Pinon, A. C.; Rossini, A. J.; Schantz, S.; Emsley, L. Structure of Lipid Nanoparticles Containing siRNA or mRNA by Dynamic Nuclear Polarization-Enhanced NMR Spectroscopy. *J. Phys. Chem. B* **2018**, *122* (7), 2073−2081.
(64) Wilson, S. C.; Baryza, J. L.; Reynolds, A. J.; Bowman, K.; Keegan, M. E.; Standley, S. M.; Gardner, N. P.; Parmar, P.; Agir, V. O.; Yadav, S.; et al. Real Time Measurement of PEG Shedding from Lipid Nanoparticles in Serum via NMR Spectroscopy. *Mol. Pharmaceutics* **2015**, *12* (2), 386−392.
(65) Whitehead, K. A.; Dorkin, J. R.; Vegas, A. J.; Chang, P. H.; Veiseh, O.; Matthews, J.; Fenton, O. S.; Zhang, Y.; Olejnik, K. T.; Yesilyurt, V.; et al. Degradable Lipid Nanoparticles with Predictable in Vivo siRNA Delivery Activity. *Nat. Commun.* **2014**, *5*, 1−10.
(66) Yanez Arteta, M.; Kjellman, T.; Bartesaghi, S.; Wallin, S.; Wu, X.; Kvist, A. J.; Dabkowska, A.; Székely, N.; Radulescu, A.; Bergenholtz, J.; et al. Successful Reprogramming of Cellular Protein Production through mRNA Delivered by Functionalized Lipid Nanoparticles. *Proc. Natl. Acad. Sci. U. S. A.* **2018**, *115* (15), E3351−E3360.
(67) Akinc, A.; Goldberg, M.; Qin, J.; Dorkin, J. R.; Gamba-Vitalo, C.; Maier, M.; Jayaprakash, K. N.; Jayaraman, M.; Rajeev, K. G.; Manoharan, M.; et al. Development of Lipidoid-siRNA Formulations for Systemic Delivery to the Liver. *Mol. Ther.* **2009**, *17* (5), 872−879.
(68) Bao, Y.; Jin, Y.; Chivukula, P.; Zhang, J.; Liu, Y.; Liu, J.; Clamme, J.-P.; Mahato, R. I.; Ng, D.; Ying, W.; et al. Effect of PEGylation on Biodistribution and Gene Silencing of siRNA/Lipid Nanoparticle Complexes. *Pharm. Res.* **2013**, *30* (2), 342−351.
(69) Chen, S.; Tam, Y. Y. C.; Lin, P. J. C.; Sung, M. M. H.; Tam, Y. K.; Cullis, P. R. Influence of Particle Size on the in Vivo Potency of Lipid Nanoparticle Formulations of siRNA. *J. Controlled Release* **2016**, *235*, 236−244.
(70) Alabi, C. A.; Love, K. T.; Sahay, G.; Yin, H.; Luly, K. M.; Langer, R.; Anderson, D. G. Multiparametric Approach for the Evaluation of Lipid Nanoparticles for siRNA Delivery. *Proc. Natl. Acad. Sci. U. S. A.* **2013**, *110* (32), 12881−12886.
(71) Jayaraman, M.; Ansell, S. M.; Mui, B. L.; Tam, Y. K.; Chen, J.; Du, X.; Butler, D.; Eltepu, L.; Matsuda, S.; Narayanannair, J. K.; et al. Maximizing the Potency of siRNA Lipid Nanoparticles for Hepatic Gene Silencing in Vivo. *Angew. Chem., Int. Ed.* **2012**, *51* (34), 8529−8533.
(72) Dahlman, J. E.; Kauffman, K. J.; Xing, Y.; Shaw, T. E.; Mir, F. F.; Dlott, C. C.; Langer, R.; Anderson, D. G.; Wang, E. T. Barcoded Nanoparticles for High Throughput in Vivo Discovery of Targeted Therapeutics. *Proc. Natl. Acad. Sci. U. S. A.* **2017**, *114* (8), 2060−2065.
(73) Paunovska, K.; Sago, C. D.; Monaco, C. M.; Hudson, W. H.; Castro, M. G.; Rudoltz, T. G.; Kalathoor, S.; Vanover, D. A.; Santangelo, P. J.; Ahmed, R.; et al. A Direct Comparison of in Vitro and in Vivo Nucleic Acid Delivery Mediated by Hundreds of Nanoparticles Reveals a Weak Correlation. *Nano Lett.* **2018**, *18* (3), 2148−2157.
(74) Sago, C. D.; Lokugamage, M. P.; Paunovska, K.; Vanover, D. A.; Monaco, C. M.; Shah, N. N.; Gamboa Castro, M.; Anderson, S. E.; Rudoltz, T. G.; Lando, G. N.; et al. High-Throughput in Vivo Screen of Functional mRNA Delivery Identifies Nanoparticles for Endothelial Cell Gene Editing. *Proc. Natl. Acad. Sci. U. S. A.* **2018**, *115* (42), E9944−E9952.
(75) Gilleron, J.; Querbes, W.; Zeigerer, A.; Borodovsky, A.; Marsico, G.; Schubert, U.; Manygoats, K.; Seifert, S.; Andree, C.; Stöter, M.; et al. Image-Based Analysis of Lipid Nanoparticle-Mediated siRNA Delivery, Intracellular Trafficking and Endosomal Escape. *Nat. Biotechnol.* **2013**, *31* (7), 638−646.
(76) Trifonova, R.; Charisse, K.; Lieberman, J.; Kirchhausen, T.; Ai, A.; Wittrup, A.; Hamar, P.; Liu, X.; Manoharan, M. Visualizing Lipid-Formulated siRNA Release from Endosomes and Target Gene Knockdown. *Nat. Biotechnol.* **2015**, *33* (8), 870−876.
(77) Tang, J.; Baxter, S.; Menon, A.; Alaarg, A.; Sanchez-Gaytan, B. L.; Fay, F.; Zhao, Y.; Ouimet, M.; Braza, M. S.; Longo, V. A.; et al. Immune Cell Screening of a Nanoparticle Library Improves Atherosclerosis Therapy. *Proc. Natl. Acad. Sci. U. S. A.* **2016**, *113* (44), E6731−E6740.
(78) Bertrand, N.; Wu, J.; Xu, X.; Kamaly, N.; Farokhzad, O. C. Cancer Nanotechnology: The Impact of Passive and Active Targeting in the Era of Modern Cancer Biology. *Adv. Drug Delivery Rev.* **2014**, *66*, 2−25.
(79) Barenholz, Y. Doxil - The First FDA-Approved Nano-Drug: Lessons Learned. *J. Controlled Release* **2012**, *160* (2), 117−134.
(80) Peer, D.; Karp, J. M.; Hong, S.; Farokhzad, O. C.; Margalit, R.; Langer, R. Nanocarriers as an Emerging Platform for Cancer Therapy. *Nat. Nanotechnol.* **2007**, *2* (12), 751−760.
(81) Liu, Y.; Xu, C.-F.; Iqbal, S.; Yang, X.-Z.; Wang, J. Responsive Nanocarriers as an Emerging Platform for Cascaded Delivery of Nucleic Acids to Cancer. *Adv. Drug Delivery Rev.* **2017**, *115*, 98−114.
(82) Allen, T. M. Ligand-Targeted Therapeutics in Anticancer Therapy. *Nat. Rev. Cancer* **2002**, *2* (10), 750−763.
(83) Bartlett, D. W.; Su, H.; Hildebrandt, I. J.; Weber, W. A.; Davis, M. E. Impact of Tumor-Specific Targeting on the Biodistribution and Efficacy of siRNA Nanoparticles Measured by Multimodality in Vivo Imaging. *Proc. Natl. Acad. Sci. U. S. A.* **2007**, *104* (39), 15549−15554.
(84) Bareford, L.; Swaan, P. Endocytic Mechanisms for Targeted Drug Delivery. *Adv. Drug Delivery Rev.* **2007**, *59* (8), 748−758.
(85) Garnacho, C. Intracellular Drug Delivery: Mechanisms for Cell Entry. *Curr. Pharm. Des.* **2016**, *22* (9), 1210−1226.
(86) Kim, S.-S.; Peer, D.; Kumar, P.; Subramanya, S.; Wu, H.; Asthana, D.; Habiro, K.; Yang, Y.-G.; Manjunath, N.; Shimaoka, M.; et al. RNAi-Mediated CCR5 Silencing by LFA-1-Targeted Nanoparticles Prevents HIV Infection in BLT Mice. *Mol. Ther.* **2010**, *18* (2), 370−376.
(87) Lu, C.; Shimaoka, M.; Salas, A.; Springer, T. A. The Binding Sites for Competitive Antagonistic, Allosteric Antagonistic, and Agonistic Antibodies to the I Domain of Integrin LFA-1. *J. Immunol.* **2004**, *173* (6), 3972−3978.


DOI: 10.1021/acs.molpharmaceut.8b01290
*Mol. Pharmaceutics* 2019, 16, 2265−2277

(88) Ramishetti, S.; Kedmi, R.; Goldsmith, M.; Leonard, F.; Sprague, A. G.; Godin, B.; Gozin, M.; Cullis, P. R.; Dykxhoorn, D. M.; Peer, D. Systemic Gene Silencing in Primary T Lymphocytes Using Targeted Lipid Nanoparticles. *ACS Nano* **2015**, *9* (7), 6706−6716.
(89) Weinstein, S.; Toker, I. A.; Emmanuel, R.; Ramishetti, S.; Hazan-Halevy, I.; Rosenblum, D.; Goldsmith, M.; Abraham, A.; Benjamini, O.; Bairey, O.; et al. Harnessing RNAi-Based Nanomedicines for Therapeutic Gene Silencing in B-Cell Malignancies. *Proc. Natl. Acad. Sci. U. S. A.* **2016**, *113* (1), E16−E22.
(90) Cohen, Z. R.; Ramishetti, S.; Peshes-Yaloz, N.; Goldsmith, M.; Wohl, A.; Zibly, Z.; Peer, D. Localized RNAi Therapeutics of Chemoresistant Grade IV Glioma Using Hyaluronan-Grafted Lipid-Based Nanoparticles. *ACS Nano* **2015**, *9* (2), 1581−1591.
(91) Saha, B.; Songe, P.; Evers, T. H.; Prins, M. W. J. The Influence of Covalent Immobilization Conditions on Antibody Accessibility on Nanoparticles. *Analyst* **2017**, *142* (22), 4247−4256.
(92) Malone, M. L.; Cavett, V. J.; Paegel, B. M. Chemoselective Coupling Preserves the Substrate Integrity of Surface-Immobilized Oligonucleotides for Emulsion PCR-Based Gene Library Construction. *ACS Comb. Sci.* **2017**, *19* (1), 9−14.
(93) Jeong, S.; Park, J. Y.; Cha, M. G.; Chang, H.; Kim, Y. il; Kim, H. M.; Jun, B. H.; Lee, D. S.; Lee, Y. S.; Jeong, J. M.; et al. Highly Robust and Optimized Conjugation of Antibodies to Nanoparticles Using Quantitatively Validated Protocols. *Nanoscale* **2017**, *9* (7), 2548−2555.
(94) Kedmi, R.; Veiga, N.; Ramishetti, S.; Goldsmith, M.; Rosenblum, D.; Dammes, N.; Hazan-Halevy, I.; Nahary, L.; Leviatan-Ben-Arye, S.; Harlev, M.; et al. A Modular Platform for Targeted RNAi Therapeutics. *Nat. Nanotechnol.* **2018**, *13* (3), 214−219.
(95) Veiga, N.; Goldsmith, M.; Granot, Y.; Rosenblum, D.; Dammes, N.; Kedmi, R.; Ramishetti, S.; Peer, D. Cell Specific Delivery of Modified mRNA Expressing Therapeutic Proteins to Leukocytes. *Nat. Commun.* **2018**, *9* (1), 9.
(96) Zhou, J.; Rossi, J. Aptamers as Targeted Therapeutics: Current Potential and Challenges. *Nat. Rev. Drug Discovery* **2017**, *16* (3), 181−202.
(97) Verheugt, F. W. A. A. An Anticoagulant Too Good to Be True for Revascularisation. *Lancet* **2016**, *387* (10016), 314−315.
(98) Akinc, A.; Querbes, W.; De, S.; Qin, J.; Frank-Kamenetsky, M.; Jayaprakash, K. N.; Jayaraman, M.; Rajeev, K. G.; Cantley, W. L.; Dorkin, J. R.; et al. Targeted Delivery of RNAi Therapeutics With Endogenous and Exogenous Ligand-Based Mechanisms. *Mol. Ther.* **2010**, *18* (7), 1357.
(99) Yoshizawa, T.; Hattori, Y.; Hakoshima, M.; Koga, K.; Maitani, Y. Folate-Linked Lipid-Based Nanoparticles for Synthetic siRNA Delivery in KB Tumor Xenografts. *Eur. J. Pharm. Biopharm.* **2008**, *70* (3), 718.
(100) Johnsen, K. B.; Burkhart, A.; Melander, F.; Kempen, P. J.; Vejlebo, J. B.; Siupka, P.; Nielsen, M. S.; Andresen, T. L.; Moos, T. Targeting Transferrin Receptors at the Blood-Brain Barrier Improves the Uptake of Immunoliposomes and Subsequent Cargo Transport into the Brain Parenchyma. *Sci. Rep.* **2017**, *7* (1), 10396.
(101) Kabilova, T. O.; Shmendel, E. V.; Gladkikh, D. V.; Chernolovskaya, E. L.; Markov, O. V.; Morozova, N. G.; Maslov, M. A.; Zenkova, M. A. Targeted Delivery of Nucleic Acids into Xenograft Tumors Mediated by Novel Folate-Equipped Liposomes. *Eur. J. Pharm. Biopharm.* **2018**, *123*, 59−70.
(102) Jia, Z.; Gong, Y.; Pi, Y.; Liu, X.; Gao, L.; Kang, L.; Wang, J.; Yang, F.; Tang, J.; Lu, W.; et al. PPB Peptide-Mediated siRNA-Loaded Stable Nucleic Acid Lipid Nanoparticles on Targeting Therapy of Hepatic Fibrosis. *Mol. Pharmaceutics* **2018**, *15* (1), 53−62.
(103) Gindy, M. E.; Leone, A. M.; Cunningham, J. J. Challenges in the Pharmaceutical Development of Lipid-Based Short Interfering Ribonucleic Acid Therapeutics. *Expert Opin. Drug Delivery* **2012**, *9* (2), 171−182.
(104) Integrated DNA Technologies. Large-Scale DNA and RNA Oligonucleotides. https://www.idtdna.com/pages/products/custom-dna-rna/large-scale-synthesis.
(105) City of Hope. GMP Manufacturing. https://www.cityofhope.org/research/shared-resources/gmp-manufacturing.
(106) Study Evaluating Safety and Efficacy of CAR-T Cells Targeting CD123 in Patients With Acute Leukemia. https://clinicaltrials.gov/ct2/show/NCT03672851.
(107) Yu, A. M.; Jian, C.; Yu, A. H.; Tu, M. J. RNA Therapy: Are We Using the Right Molecules? *Pharmacol. Ther.* **2019**, *196*, 91.
(108) Moderna, Inc. https://www.modernatx.com/.
(109) Moderna, Inc. Clinical Trials. https://www.modernatx.com/pipeline/clinical-trials.
(110) Meure, L. A.; Foster, N. R.; Dehghani, F. Conventional and Dense Gas Techniques for the Production of Liposomes: A Review. *AAPS PharmSciTech* **2008**, *9* (3), 798−809.
(111) Hirota, S.; de Ilarduya, C. T.; Barron, L. G.; Szoka, F. C. Simple Mixing Device to Reproducibly Prepare Cationic Lipid-DNA Complexes (Lipoplexes). *BioTechniques* **1999**, *27* (2), 286−290.
(112) Leung, A. K. K. K.; Tam, Y. Y. C.; Chen, S.; Hafez, I. M.; Cullis, P. R. Microfluidic Mixing: A General Method for Encapsulating Macromolecules in Lipid Nanoparticle Systems. *J. Phys. Chem. B* **2015**, *119* (28), 8698−8706.
(113) Jahn, A.; Stavis, S. M.; Hong, J. S.; Vreeland, W. N.; Devoe, D. L.; Gaitan, M. Microfluidic Mixing and the Formation of Nanoscale Lipid Vesicles. *ACS Nano* **2010**, *4* (4), 2077−2087.
(114) Zhigaltsev, I. V.; Belliveau, N.; Hafez, I.; Leung, A. K. K.; Huft, J.; Hansen, C.; Cullis, P. R. Bottom-Up Design and Synthesis of Limit Size Lipid Nanoparticle Systems with Aqueous and Triglyceride Cores Using Millisecond Microfluidic Mixing. *Langmuir* **2012**, *28* (7), 3633−3640.
(115) Evers, M. J. W.; Kulkarni, J. A.; Van der Meel, R.; Cullis, P. R.; Vader, P.; Schiffelers, R. M. State-of-the-Art Design and Rapid-Mixing Production Techniques of Lipid Nanoparticles for Nucleic Acid Delivery. *Small Methods.* **2018**, *2*, 1700375.
(116) Garg, S.; Heuck, G.; Ip, S.; Ramsay, E. Microfluidics: A Transformational Tool for Nanomedicine Development and Production. *J. Drug Target.* **2016**, *24* (9), 821−835.
(117) Fang, R. H.; Chen, K. N. H.; Aryal, S.; Hu, C. M. J.; Zhang, K.; Zhang, L. Large-Scale Synthesis of Lipid-Polymer Hybrid Nanoparticles Using a Multi-Inlet Vortex Reactor. *Langmuir* **2012**, *28* (39), 13824−13829.
(118) Kim, Y.; Lee Chung, B.; Ma, M.; Mulder, W. J. M.; Fayad, Z. A.; Farokhzad, O. C.; Langer, R. Mass Production and Size Control of Lipid-Polymer Hybrid Nanoparticles through Controlled Microvortices. *Nano Lett.* **2012**, *12* (7), 3587−3591.
(119) Finn, J. D.; Smith, A. R.; Patel, M. C.; Shaw, L.; Youniss, M. R.; Van Heteren, J.; Dirstine, T.; Ciullo, C.; Lescarbeau, R.; Seitzer, J.; et al. A Single Administration of CRISPR/Cas9 Lipid Nanoparticles Achieves Robust and Persistent In Vivo Genome Editing. *Cell Rep.* **2018**, *22* (9), 2227.


DOI: 10.1021/acs.molpharmaceut.8b01290
*Mol. Pharmaceutics* 2019, 16, 2265−2277